Study of Fracture Toughness and Notch Toughness under Impact Loading of Electron Beam Melted Ti6Al4V Alloy

Vidit Tambi

A thesis

submitted in partial fulfillment of the

requirements for the degree of

Master of Science

University of Washington

2025

Committee:

Ramulu Mamidala

John Kramlich

Dan Sanders

Program Authorized to offer degree:

Mechanical Engineering

University of Washington

Abstract

Study of Fracture Toughness and Notch Toughness under Impact loading of Electron Beam Melted Ti6Al4V Alloy

Vidit Tambi

Chair of the Supervisory Committee:

Ramulu Mamidala

Department of Mechanical Engineering

This thesis presents a comprehensive investigation into the fracture toughness and the notch toughness behavior of Electron Beam Powder Bed Fused (EB-PBF) Ti-6Al-4V alloy, with particular focus on the effects of build orientation, key mechanical properties and microstructural characteristics. Vertical compact tension specimens as well as Horizontal and vertical Charpy Impact specimens were fabricated using optimized processing parameters. Notch toughness was evaluated using instrumented Charpy impact tests, while fracture toughness was measured using linear-elastic fracture mechanics on fatigue-precracked specimens. The fracture surfaces were examined using profilometry, scanning electron microscopy, microhardness measurements, and microstructural analysis. The findings were correlated with the mechanical properties of similarly fabricated specimens under identical conditions.

Vertical specimens demonstrated superior toughness performance across both test regimes. In fracture toughness testing, Y-Z specimens exhibited the highest toughness (65.81 MPa√m), while

X-Z showed the lowest (63.10 MPa√m). Post-machining generally improved toughness values by mitigating surface defects and enhancing crack resistance. In impact testing, vertical specimens absorbed ~50% more energy than horizontal specimens due to greater ductility, lower microhardness, and crack propagation paths that intersect prior-β grains more frequently. Surface profilometry confirmed ~35% higher shear lip heights, ~50% larger shear areas, and ~15% rougher cracking regions in vertical specimens, indicating increased plastic deformation. The study highlights the critical role of build orientation and post-processing in tailoring the toughness of EB-PBF Ti6Al4V, offering valuable guidance for design and qualification of AM components in structural applications.

TABLE OF CONTENTS

ACKNOWLEDGEMENT

This thesis would not have been possible without the guidance, support, and encouragement of many people. I owe a debt of gratitude to Professor Ramulu Mamidala for his guidance, words of wisdom, and unwavering support during this project. His advice influenced how I conduct research and solve problems, and his exacting standards motivated me to produce my best work. I am also grateful to the University of Washington's (UW) Department of Mechanical Engineering for providing a stimulating learning environment and access to the resources that enabled my research.

I want to express my gratitude to Sayem, Nicole, and Melody, my lab partners, for their kind assistance, enlightening conversations, and good humor throughout the long days of analysis and experimentation. The positive aspects were memorable and the challenging ones were tolerable because of your friendship. My friends deserve just as much gratitude for their unwavering support, punctual check-ins, and maintenance of a healthy balance outside of the lab.

Above all, my mother, father, and sister deserve my sincere appreciation. I was supported at every turn by their unwavering love, support, and incalculable sacrifices. They celebrated each little victory along the road and had faith in me when I doubted myself. Without their assistance, this thesis would not have been feasible.

List of Figures

Figure 12. (a) Isometric view of Charpy impact specimens inside the build chamber, (b) Top view of the specimens showing three different notch orientations, (c) Dimensions of the specimen, (d) Few fabricated specimens

Figure 13. (a) Notch dimensions, (b) Notch orientations with respect to the build plate orientation system

Figure 14. Pictorial representation of Charpy impact testing and tester with a specimen loaded.

Figure 15. (a) Cracking and shearing region of a fracture surface, (b) Surface topography of fracture region, (c) Shear lip height measurement, (d) Shear angle measurement

Figure 16. Calculation of pore area and porosity percentage using ImageJ software (numbers in yellow represent the pores visible by the naked eye)

Figure 17. Impact energy variation with respect to (a) different build orientations, (b) radial distance, (c) along X and Y axis

Figure 18. The surface topography of the fractured EB-PBF Ti6Al4V

Figure 19. Printed notch radius of EB-PBF Ti6Al4V of different build orientations – (a) HS, (b) HT and (c) V

Figure 20. Variation of (a) Average actual Shear area, (b) Average Shear width, (c) Average shear lip height, and (d) MCSL and MCSD lengths with respect to build orientations

Figure 21. The cracking path and prior - β columnar grains within the microstructure of EB-PBF Ti6Al4V (a-d) horizontal- HT specimens, (e-h) vertical specimen. The prior – β grains are highlighted with red dashed line.

Figure 22. SEM images of fractured EB-PBF specimens: (a) Horizontal (HT) – 30x, (b) Horizontal (HT) – 37x, (c) Horizontal (HT) – 60x, (d) Horizontal (HT) – 160x, (e) Vertical (V) – 30x, (f) Vertical (V) – 30x, (g) Vertical (V) – 200x, (h) Vertical (V) – 200x (yellow arrows highlight fracture flutes)

Figure 23. Broad comparison of notch toughness of as built and machined EB-PBF Ti6Al4V with literature [25,32,35,44,52]

Figure 24. Variation of Notch Toughness with respect to (a) Average shear lip height, (b) Average shear width

List of Tables

Chapter 1 Introduction

1.1 Overview and Background Literature

Additive Manufacturing (AM), often referred to as 3D printing, represents a new age of manufacturing, shifting from traditional subtractive manufacturing methods. Instead of removing material from a block or casting into a mold, AM fabricates components layer by layer directly from a digital 3D CAD model [1]. This layer-wise approach enables the production of geometrically complex parts with reduced material waste, shorter lead times, and design flexibility that is difficult or impossible to achieve using conventional manufacturing techniques. Additive Manufacturing process is currently being used in the aerospace, automotive, and biomedical industries, among others, for rapid prototyping as well as production of complex metal parts [2,3].

Over the past two decades, AM has matured from a prototyping tool into a viable production technology for functional end-use parts. Today, it finds applications in a wide array of industries particularly for high-performance applications as AM offers the ability to produce lightweight structures, topology-optimized designs, and functionally graded materials tailored to specific loading conditions [4]. Among the several AM techniques developed, Powder Bed Fusion (PBF) has emerged as one of the most widely adopted methods for metal additive manufacturing. PBF processes build components by selectively melting thin layers of metal powder using a focused energy source—typically a laser or an electron beam. The PBF category includes techniques such as Selective Laser Melting (SLM/ L-PBF) and Electron Beam Melting (EBM/ EB-PBF).

Electron Beam Melting, developed and commercialized primarily by ARCAM AB (now part of GE Additive), uses a high-energy electron beam to melt pre-alloyed metal powders under a high vacuum environment [5]. The vacuum not only protects reactive metals like titanium from oxidation but also promotes defect-free builds and ensures better control over the melt pool

dynamics as there is no interference from gas flow unlike the laser powder bed fusion (L-PBF) [6,7]. EB-PBF typically operates at higher build temperatures (often exceeding 700°C), resulting in reduced residual stresses, in-situ annealing, and a fully dense microstructure with minimal internal defects. Its high build temperature often eliminates the need for extensive support structures. This contrasts with L-PBF, which operates in an inert gas atmosphere (typically argon) and may suffer from higher thermal gradients and stress accumulation during processing. In contrast, LPBF employs a laser to melt fine powders, enabling higher resolution and superior surface finishes (~15 μm Ra), though it typically requires more post-processing and is prone to greater powder degradation.

The EB-PBF process has a smaller build plate and build volume, which limits the part size to be smaller than the L-PBF process. The roughness of EB-PBF parts (~28 μm Ra) is often greater due to larger powder diameter and higher beam size compared to L-PBF process [8]. Machining is recommended for both the processes while additional post processing (i.e., heat treatment) is needed in L-PBF to reduce residual stresses [9]. However, EB-PBF has its own challenges. Issues such as surface roughness, beam deflection due to magnetic fields, limited resolution compared to lasers, and powder recycling constraints require attention. Moreover, the anisotropic nature of layer-wise fabrication introduces variability in mechanical properties depending on the build orientation.

Ti-6Al-4V (Grade 5 titanium) is the most commonly used titanium alloy, comprising approximately 90% of all titanium applications. Ti6Al4V is widely used for stress-critical applications due to its high specific strength, superior fatigue and fracture properties, and biocompatibility. It exhibits a strong balance between tensile strength and ductility due to HCP and BCC crystallographic structure [10]. The alloy contains 6% aluminum (an alpha stabilizer) and

4% vanadium (a beta stabilizer), resulting in a dual-phase alpha-beta microstructure that can be tailored through thermal and mechanical processing. Ti-6Al-4V is particularly well-suited for EB-PBF due to its low thermal conductivity and reactivity with oxygen—conditions that are well-managed in EB-PBF's vacuum environment. EB-PBF-fabricated Ti-6Al-4V parts are known to exhibit a columnar grain structure with a transformed $\alpha + \beta$ lamellar morphology, influenced by the high build temperatures and slow cooling rates. While the resultant mechanical properties are generally comparable to wrought or forged counterparts, the microstructure can vary significantly with build orientation, scan strategy, and local thermal history.

One of the major differences between PBF processes and traditional manufacturing processes (e.g. casting) is the greater number of variabilities and uncertainties involved in PBF processes. Since PBF processes are performed layer-by-layer, the mechanical properties of fabricated metallic parts exhibit anisotropy due to variation in localized microstructure, process induced defects such as porosity and lack of fusion (LOF), and surface roughness. Consequently, the mechanical properties of the EB-PBF Ti6Al4V varies with orientation and build location within the build space [11]. Specifically, the tensile strength and fatigue properties vary by as much as 15% [2,3,12].

Understanding the mechanical behavior of components produced via Electron Beam Melting (EB-PBF) is crucial to ensure their reliability in demanding service environments. While EB-PBF-processed parts often demonstrate near-wrought levels of tensile strength and yield strength, these metrics alone are not sufficient for qualifying materials for critical structural applications. In many engineering scenarios—such as aerospace structures, load-bearing implants, or defense components—parts may be subjected to complex loading, cyclic fatigue, accidental impact, or abrupt crack propagation. Under such conditions, the resistance of a material to crack initiation

and propagation becomes more important than its elastic or plastic behavior. Hence, toughness metrics—such as fracture and notch toughness—are indispensable for structural reliability.

One of the key concerns in EB-PBF-fabricated parts is their anisotropy, resulting from the directional solidification and thermal gradients during the layer-by-layer deposition process. The build orientation (horizontal vs. vertical) significantly affects grain morphology, residual stresses, and defect distribution. For instance, vertically built parts may exhibit columnar grains aligned with the build direction, which can influence crack deflection paths and energy absorption during fracture or impact events. Moreover, although EB-PBF generally produces fully dense parts with minimal porosity, process-induced defects such as lack-of-fusion zones, gas pores, and unmelted powder particles can still occur [13]. These microscopic discontinuities act as stress concentrators and can severely degrade the material's load handling capabilities. Even small surface imperfections or roughness, which are common due to the partially sintered powder cake surrounding EB-PBF parts, may serve as initiation points for cracks under service loading.

Another crucial factor is the microstructure, which evolves due to the high-temperature vacuum environment and slow cooling rates in EB-PBF. Ti-6Al-4V parts fabricated via EB-PBF typically exhibit a coarser, acicular α-phase within prior β-grain boundaries, leading to a basket-weave or Widmanstätten-type structure [14]. While this structure is beneficial for static strength, it may not provide optimal performance under dynamic or fracture-critical scenarios unless carefully controlled.

Beyond static tensile testing, which is standardized and well-documented, relatively fewer studies focus on Fracture toughness and Notch/ Impact toughness of EB-PBF Ti-6Al-4V. These properties provide insights into the material's ability to resist crack propagation (fracture toughness) and to absorb energy during sudden impact loading (notch toughness). This is especially relevant for

applications involving dynamic or off-design loading, such as: turbine blades exposed to high-speed debris impacts, landing gear components experiencing sudden force spikes, orthopedic implants under accidental falls or impact loads and automotive or defense parts subjected to crash or ballistic scenarios. Consequently, a systematic study of these properties—across different build orientations, specimen geometries, and microstructural conditions—is critical for advancing the qualification and certification of EB-PBF Ti-6Al-4V components for real-world applications.

(a) (b) (c)

Figure 1. (a) ARCAM A2X EBM machine with build chamber on the right, (b) Backend control system of the EBM, (c) Close-up view of the heat shield being installed in the build chamber

1.2 Objectives/ Aim

- To fabricate Ti-6Al-4V specimens using the EBM process, maintaining consistent build parameters while varying the geometry and orientation (horizontal vs. vertical) relevant to fracture and impact testing.
- To characterize the microstructure and microhardness of the fabricated specimens in order to correlate material behavior with mechanical performance.
- To perform fracture toughness testing (ASTM E399) on compact tension (CT) specimens to assess the material's resistance to crack growth under mode-I loading.
- To conduct Charpy impact testing (ASTM E23) on notched specimens to evaluate notch sensitivity and energy absorption capability under high-strain-rate loading.
- To analyze the fracture and shear surfaces using optical and scanning electron microscopy (SEM) to understand the dominant failure mechanisms and the influence of build orientation.

Chapter 2 Fracture Toughness

2.1 Introduction

Fracture toughness is a critical material property that quantifies a material's resistance to crack propagation under applied stress. Unlike tensile strength or yield strength, which measure the ability of a material to withstand load without deformation, fracture toughness directly assesses structural reliability in the presence of pre-existing flaws. For metallic components used in aerospace, biomedical, or defense sectors—where catastrophic failure can be life-threatening—fracture toughness plays a vital role in materials selection and part qualification.

In the context of Electron Beam Melting (EBM), fracture performance is influenced not only by intrinsic material behavior but also by process-induced characteristics such as anisotropic grain structure, residual stresses, porosity, and surface roughness. Due to the layer-wise fabrication and high build temperatures inherent to EBM, Ti-6Al-4V components often exhibit a coarse lamellar $\alpha + \beta$ microstructure, with columnar grain growth along the build direction. These microstructural features, coupled with direction-dependent mechanical behavior, result in orientation-sensitive fracture properties, making a detailed understanding of K_{IC} essential. Additionally, surface roughness, a known limitation of EBM, significantly impacts fracture behavior. Rough surfaces can initiate stress concentrations that promote early crack nucleation, reducing fracture resistance.

Another important consideration is the role of post-processing, particularly machining, in modifying the surface state of AM parts. Machining helps eliminate surface irregularities and ensures dimensional accuracy but can also alter the near-surface microstructure through residual stress development, micro hardening, or thermal effects. This chapter investigates this phenomenon by comparing as-built and machined specimens, both fabricated in the vertical orientation, to evaluate how surface condition influences fracture toughness.

Several studies have been conducted on the fracture toughness of the L-PBF and EB-PBF Ti6AL4V. Seifi et. al. studied the effect of test orientation with respect to build and beam raster directions of as-deposited EB-PBF Ti6AL4V and found that the fracture toughness values are comparable to the cast and wrought Ti64 [15]. They also found presence of unmelted powders and isolated porosity in the specimens. Sahu et. al. tested the fracture toughness of heat treated DMLS Ti6AL4V specimens and indicated that the DMLS specimens surpassed heat treated L-PBF Ti6AL4V in terms of the fracture toughness [16]. Mojib et. al. compared the fracture toughness between as built and machined specimens built using EB-PBF in horizontal and vertical orientations. As-built specimens built in vertical orientation had the highest average fracture toughness values while XY specimens had the best performance among the machined ones [12]. They also reported an increase in Fracture toughness values with an increase in built height and decrease in the radial distance.

A comparative study of fracture toughness between the specimens fabricated by EB-PBF Ti6Al4V and Ti6Al4V ELI powder in four different orientations was done by Ninerola et. al. The specimens fabricated by Ti6AL4V ELI powder showed significantly better performance than the ones fabricated by Ti6AL4V powder [17]. They also reported an increase in the Fracture Toughness values and decrease in hardness values as the build height increased. Cain et. al. conducted a study on the fracture toughness of Ti6Al4V alloy produced by SLM process in three different conditions – As-built, stress relieved and heat treated and three different orientations – XZ, ZX and XY [18]. The heat treated ZX specimen had the highest value of fracture toughness followed by XZ and XY ones. It is important to note that the specimens had machined notch. Zhang et. al. studied the effect of post processing on fracture toughness of SLM Ti6L4V. Heat Treated As-built specimens demonstrated significantly higher fracture toughness than wrought or casted specimens but showed

poor ductility [19]. Kumar et. al. performed four types of heat treatment processes – two above β transus temperature and two duplex processes. Results reveal near doubling of fracture toughness after heat treatment accompanied by 20% reduction in Yield strength [20]. The heat-treated specimens showed comparable performance to that of forged and cast & HIPed specimens as martensitic α' decomposes into α/β grains.

99.7% dense SLM TI6Al4V specimens fabricated by Hooreweder et. al. were studied for their fracture toughness behavior [21]. The specimens showed inferior fracture toughness values with respect to the reference material. This was attributed to the unstable and brittle microstructure consisting of a fine martensitic phase with sharp needles. Fracture Toughness of AM repaired Ti6AL4V produced by Direct Energy Deposition was examined by Shreshtha et. al. Machined and heat-treated specimens showed comparable values to the ones fabricated by conventional techniques [22]. Zhang et. al. performed fracture toughness testing on wire + arc additive manufactured Ti6Al4V specimens with machined notch in two orientations and two thicknesses. The thicker specimens had higher values than the thin ones and both of them had slightly higher values than the wrought specimens [23].

Despite the maturity of research around static mechanical properties and microstructure of AM Ti-6Al-4V, fracture toughness remains relatively underexplored. Most studies tend to focus on tensile or fatigue performance, with few offering standardized, quantitative assessments of fracture resistance using methods such as compact tension (C-T) specimens. This study aims to address this gap by exploring the mode – I fracture toughness of pre-cracked EBM Ti-6Al-4V specimens (only in the vertical orientation), with particular attention to the effects of build space parameters, machining, and orientation. A comparative evaluation between as-built and machined specimens is performed to assess how surface condition affects crack propagation resistance. Furthermore,

post-fracture analysis is conducted through detailed fractographic examination involving optical profilometry and shear area measurements, providing a comprehensive understanding of the failure mechanisms and their correlation with microstructure and surface features.

2.2 Materials and Methods

2.2.1 Specimen Fabrication

The Grade 5 Titanium alloy (Ti6Al4V) powder was used to fabricate the Compact tension (CT) specimens for the Fracture Toughness study. The powder was supplied by Advanced Powders & Coatings (Lot: 242-G2029), with a particle size distribution ranging from 45 – 110 μm. Virgin powder (not used in any previous builds) was used and the chemical weight composition of the similar feedstock powder analyzed by our lab members in a previous study is presented in Table 1. Tensile properties of the metal fabricated with this powder by EB-PBF in the same ARCAM A2X machine and using the same build parameters are listed in Table 2. The build was performed on an ARCAM A2X Electron Beam AM system (Mölndal, Sweden) using ARCAM EBM control software version 5.0.64. Layer-wise scan rotation was enabled, and default melting parameters were used as follows: beam current =15 mA, max current = 20 mA, beam scan offset = 25 mA, beam speed = 4530 mm/sec, speed function = 45, and preheat temperature = 650°C.

The specimens were fabricated in a single build to eliminate variability from powder quality. The specimens were virtually modeled in the Materialize Magics Software following the ASTM E399 standard and 5 mm supports were added to the base of the specimens [24]. The dimensions of the specimens are shown in Figure 4. A total of 22 specimens in four vertical orientations: Z-X, Z-Y, X-Z, and Y-Z were printed simultaneously along with other specimens (see Figure 2 and Figure 3). The letter preceding the hyphen represents the direction normal to the crack plane and the letter following the hyphen represents the anticipated direction of crack extension. For Y-Z and X-Z

orientations, the crack plane was parallel to the build layers, while for Z-X and Z-Y orientations, it was transverse. The EBM system generated high-energy electron beam via a tungsten filament electron gun operating at 60 kV power. The electron beams, with a power density of up to 100 kW/cm^2, were focused using electromagnetic lenses, while beam motion was controlled by deflection coils. The beam size was 500 μm, and the theoretical layer thickness was 50 μm. The build was started with 70 kgs of virgin powder.

The build chamber pressure was maintained at 3.5×10^{-4} bar throughout the build to prevent titanium oxidation. The powder bed was preheated and the temperature was maintained to reduce thermal stress due to temperature gradients. During melting, the focused beam fused titanium powder locally at ~1900°C. Upon completion, the chamber temperature was reduced gradually from 650°C to 25°C, starting at 6°C/min and tapering to 0.4°C/min. Support structures were removed after printing. Powder Recovery System (PRS) was used to extract the specimens from the powder cake and the residual powder was recycled, then sieved and mixed with remaining hopper powder for future builds.

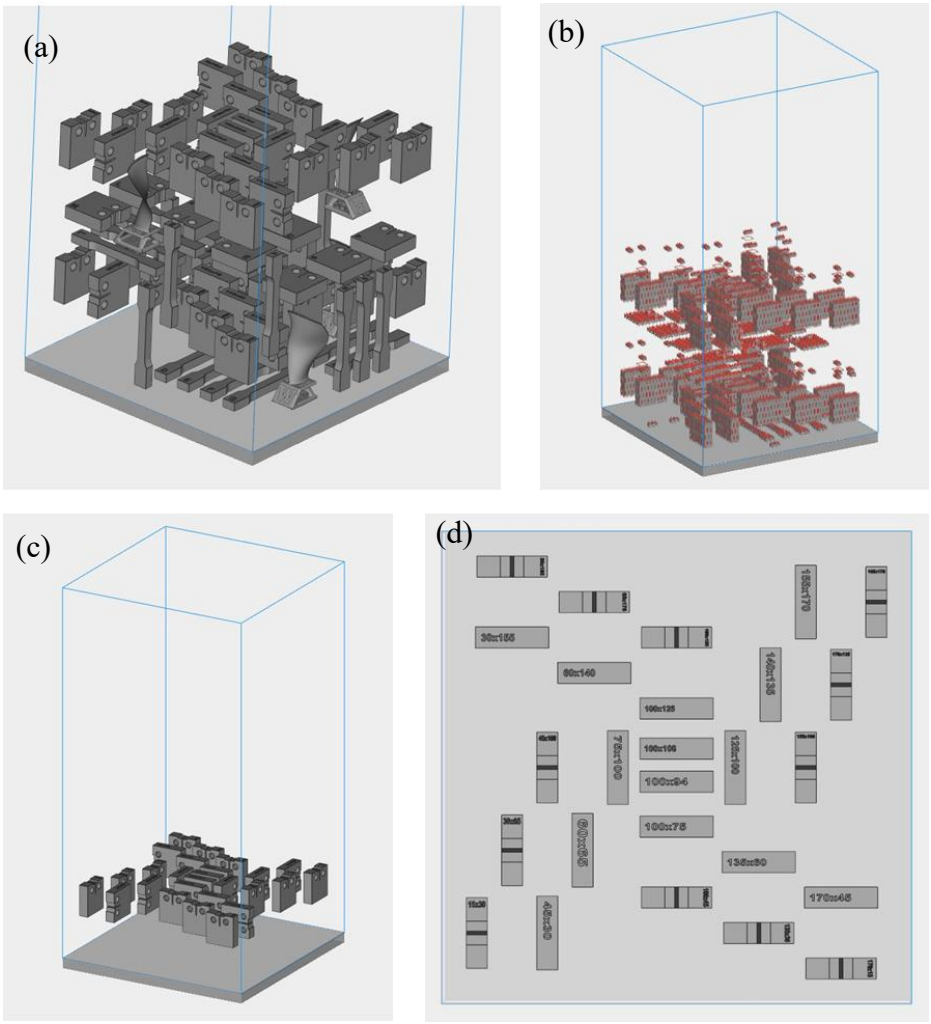

Figure 2. (a) Isometric view of the build chamber & (b) the specimen supports, (c) Isometric view & (d) Top view of the Compact Tension specimens

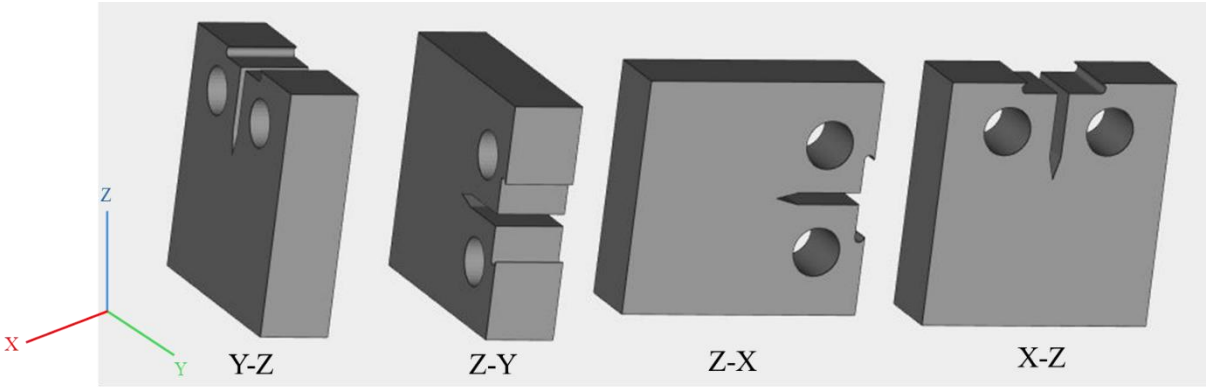

Figure 3. The four different build orientations of the Fracture toughness specimens

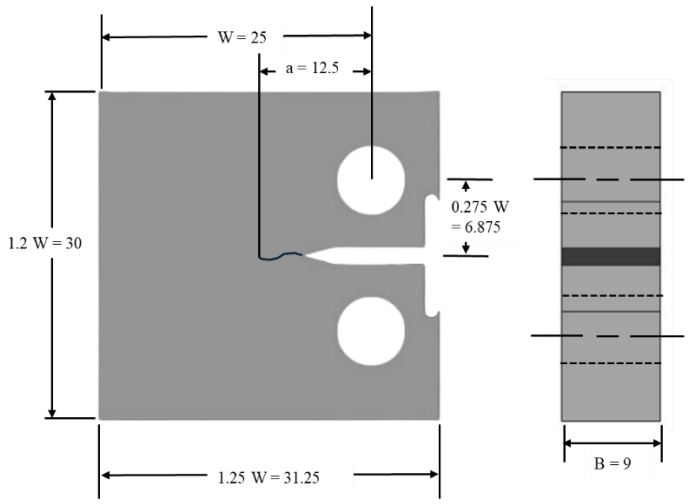

Figure 4. Dimensions of the Fracture toughness C-T specimens

Table 1. Weight percentage composition of virgin Ti6AL4V

Powder condition	Al (wt%)	V (wt%)	O (wt%)	N (wt%)	Fe (wt%)	H (wt%)
Virgin (build 1)	5.41	3.43	0.142	0.024	0.21	0.0014

Table 2. Tensile Properties of EB-PBF virgin Ti6Al4V specimens

Orientation	Elastic modulus (GPa)	Yield Strength (MPa)	Utlimate Tensile Strength (MPa)	% Elongation
Horizontal	92.7 ± 2.5	739 ± 2.7	857 ± 10.4	9.28 ± 1.06
Vertical	98.9 ± 3.2	733 ± 20.7	859 ± 20.5	12.2 ± 0.42

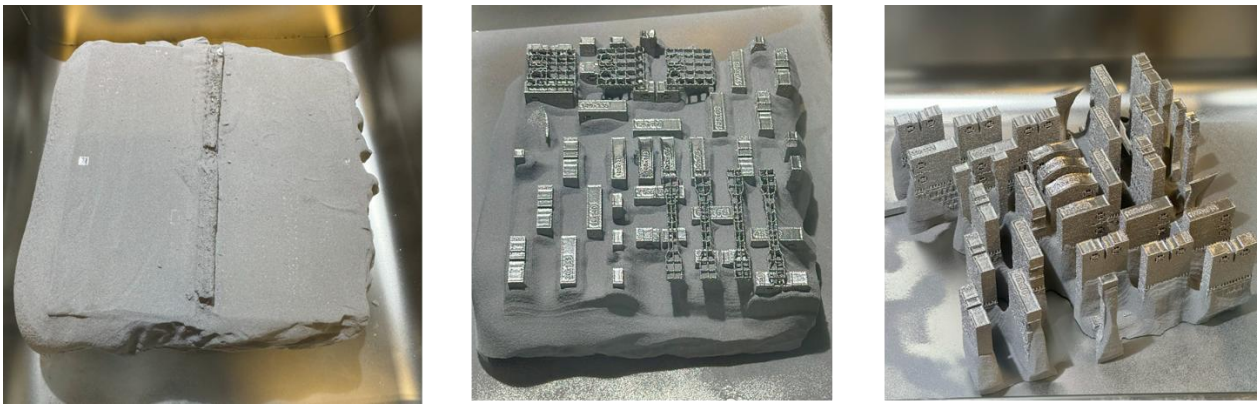

Figure 5. Powder cake extracted from the EBM after completion of the build and at different stages of specimen extraction using Powder Recovery System

2.2.2 Machining

To examine the differences in fracture toughness between as-built and machined specimens, 10 as-built specimens (all four orientations were included) were machined on both the larger surfaces which were perpendicular to the notch plane. Surface machining was performed using a ceramic-coated, 4-flute carbide tool with a 12.7 mm diameter at 500 RPM spindle speed, an 8 mm radial depth of cut, and a 0.8 mm axial depth of cut. The feed rate was set to 76.2 mm/min. After machining, the samples were ready for testing.

2.2.3 Fracture Toughness Testing

Plane-strain fracture toughness testing was performed following ASTM E399 standard using a 20 kN capacity universal testing system (Instron Model 8511, Nordwood, MA) [24]. All tests were conducted at room temperature. The compact tension (CT) specimens had a thickness of 9 mm and a width of 25 mm to minimize plasticity at the crack tip, as illustrated in Figure 4.

A sharp pre-crack was generated from the notch through cyclic loading at 60% of the anticipated plane-strain fracture toughness (KIc), with a frequency of 10 Hz and a stress ratio of 0.1. The fatigue pre-cracking load was calculated using published Ti6Al4V fracture toughness data. A crack length ratio of $0.45 \leq a/W \leq 0.55$ was achieved to ensure linear-elastic material behavior. As the testing adhered to plane-strain conditions, the calculated fracture toughness values were influenced by material thickness and crack size.

The fracture toughness tests were carried out under tension at a constant rate of 0.08–0.15 kN/sec and the crack mouth opening displacement (CMOD) was measured using a displacement gauge under a constant-rate loading. The specimens were subjected to increasing ΔK conditions until total breakage occurred. Following the conclusion of the test, the conditional fracture

toughness KQ is calculated as follows. The force at a 5% secant offset (PQ) is calculated using the initial linear slope of the recorded applied load and CMOD and a sample of load displacement curve is illustrated in Figure 6. The conditional fracture toughness, KQ, was derived from the initial load and CMOD, corresponding to ~2% crack extension. KIc values were reported when they met two validity criterias:

$$Pmax/PQ \leq 1.10 \;\&$$

$$W - a \geq 2.5\,(KQ/\sigma ys)^{2}$$

These criteria confirmed that KQ adhered to plane-strain conditions and could be classified as the material property KIc. Only KIc-compliant results were considered in the study. Equation 2.3 is used to compute the conditional fracture toughness KQ from the value of PQ, where P is the applied load, a is the crack size, W is the frontal width, and f(a/W) is the size correction factor. Equation 2.3 is used to compute the conditional fracture toughness KQ from the value of PQ, where P is the applied load, a is the crack size, W is the width, B is the thickness and f(a/W) is the size correction factor.

$$K = \frac{P * f\left(\frac{a}{W}\right)}{\left(\sqrt{\mathrm{B} * \mathrm{Bn}}\right)\sqrt{\mathrm{W}}}$$

$$f\left(\frac{a}{W}\right) = \frac{\left(2 + \frac{a}{W}\right) * \left(0.886 + 4.64\frac{a}{W} - 13.32\left(\frac{a}{w}\right)^{2} + 14.72\left(\frac{a}{W}\right)^{3} - 5.6\left(\frac{a}{W}\right)^{4}\right)}{\left(1 - \frac{a}{W}\right)^{3/2}}$$

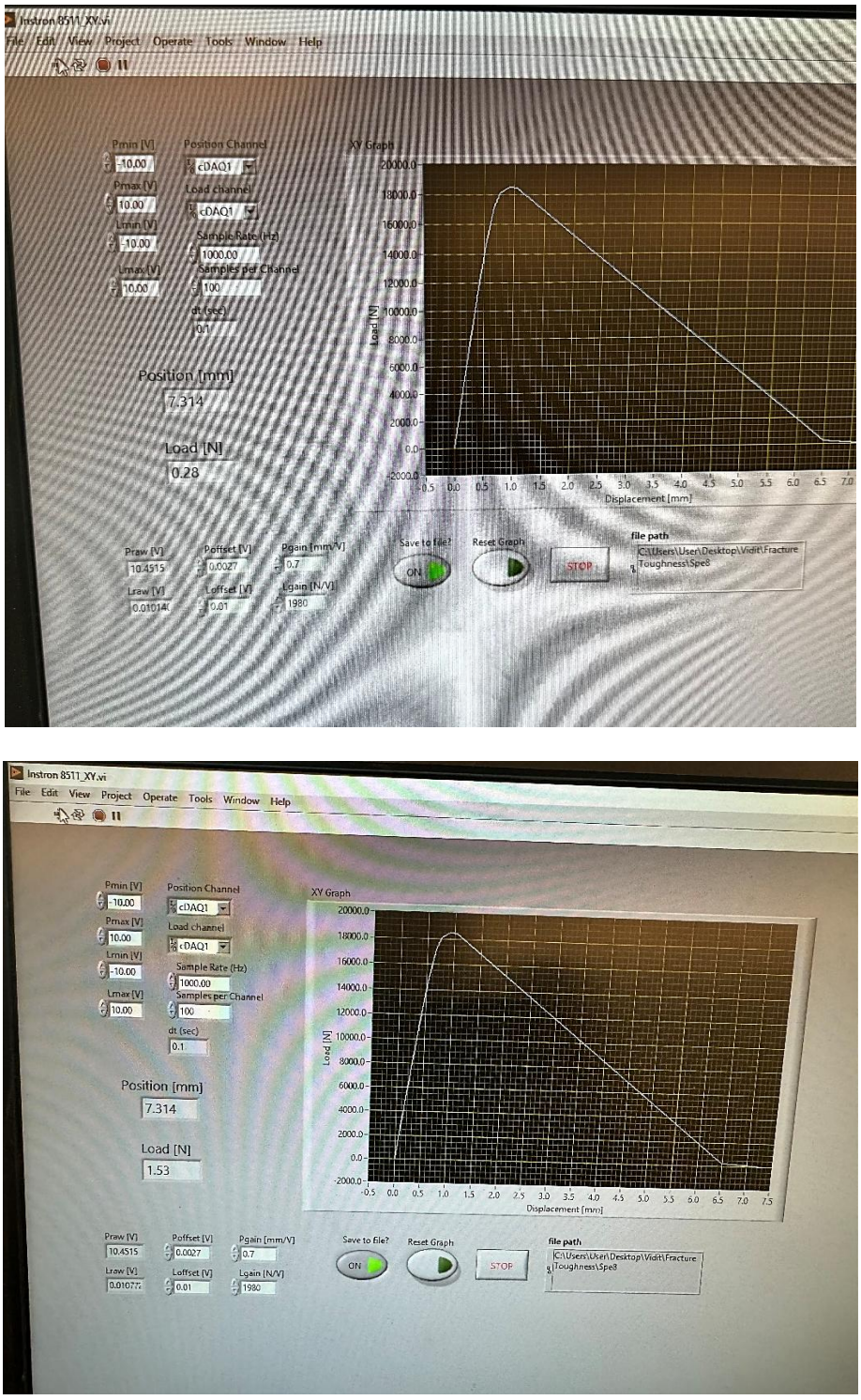

Figure 6. Sample Load vs Displacement graphs captured during Fracture toughness testing

2.2.4 Profilometry

An optical profilometer (Keyence, Model VR – 3100, Osaka, Japan) was used to capture three-dimensional surface topography of the EB-PBF Ti6Al4V specimens after the fracture toughness testing. Optical images and the 3D topography of the relevant surfaces were captured at 12x magnification. The standard surface roughness parameters were calculated for each specimen including Sa (areal roughness height), Sz (10-point height) and Sq (root mean square height). In addition, the Sp (peak height) and Sv (valley depth) parameters were estimated. In the roughness measurement, the entire cracking area was considered as the reference plane in profiling the surface topography. Topography maps of the fractured specimens were created to support identification of the dominant characteristics.

2.2.5 Shear Area analysis

The shear area from the fracture surfaces of 10 representative specimens (all four orientations were included) were measured from the high-resolution color maps using Keyence optical profilometer (Model VR – 3100, Osaka, Japan). The known specimen dimensions were used to calibrate the scale within the software, ensuring precise area measurements. For each fracture surface evaluated, the left-side and right-side shear regions were carefully outlined and the sum of these two areas served as the total shear area. To account for potential variations in measurements and minimize errors, the average shear area was calculated for the two sides of each broken specimen. The shear areas were then averaged across all the specimens of each build orientation to reflect the effects of build orientation on fracture behavior. This approach ensured consistency and minimized errors caused by manual selection or surface irregularities. Using the shear area, the shear widths of the specimens were calculated, which is a more comprehensive reflection of the shear mechanisms. By combining advanced imaging techniques with precise software-based analysis, this study

provides valuable insights into the relationship between fracture toughness, fracture mechanics and build orientation in EB-PBF Ti6Al4V alloys. Jeffs et. al. also used shear lip width to discuss the fracture behavior of EB-PBF Ti6Al4V [25]. In addition, the shear lip height was calculated from the 3D topography (Figure 7). The shear angle of the shear lips was calculated considering the horizontal cracking region as a reference.

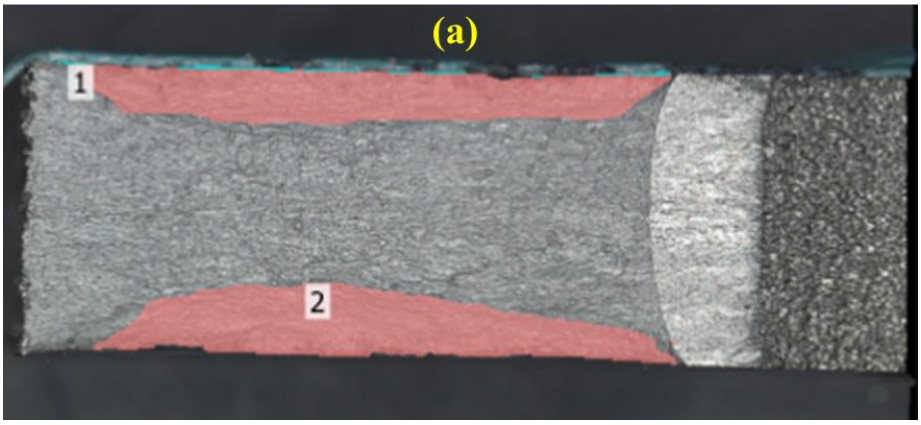

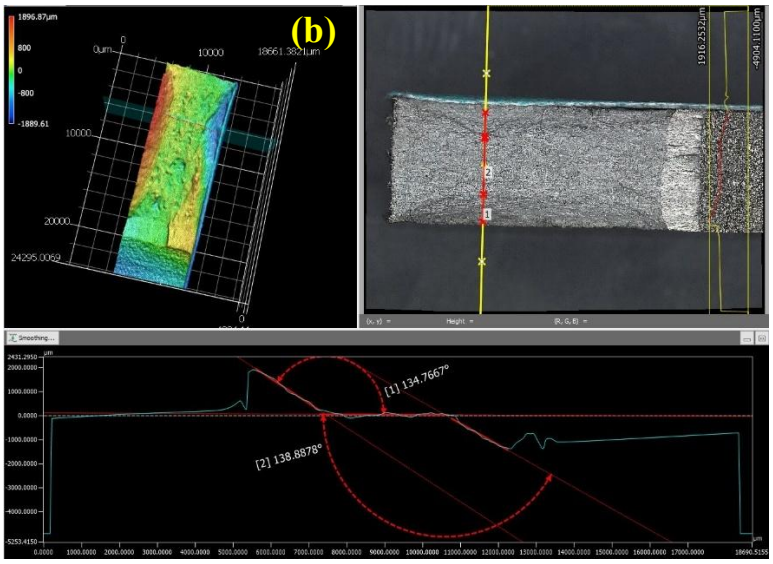

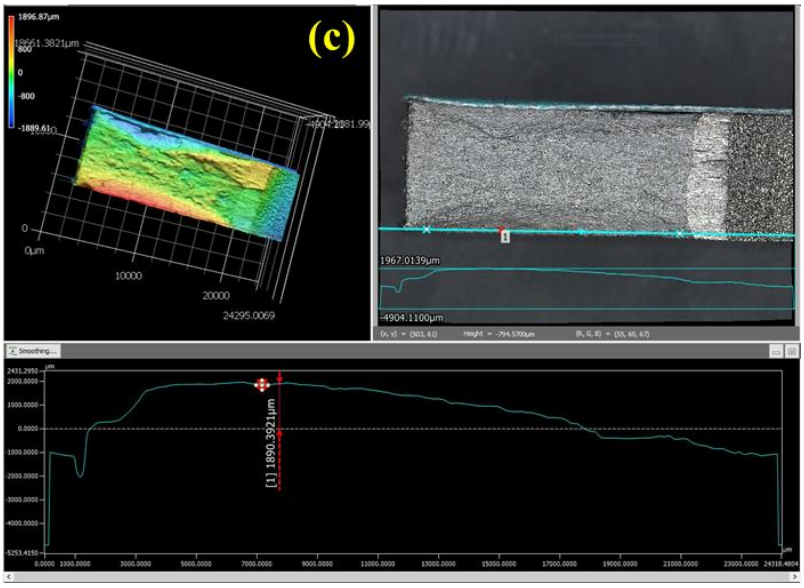

Figure 7. (a) Shear area measurement with carefully outlined shear areas, (b) Shear angle measurement, (c) Shear lip height measurement

2.3 Results

2.3.1 Fracture Toughness

The fracture toughness of the EB-PBF Ti6Al4V specimens for all four build orientations is presented in Figure 8 (a). Among the tested specimens, Y-Z specimens exhibited the highest average fracture toughness value of 65.81 MPa√m ± 0.815, with individual values ranging from 64.6 MPa√m to 66.51 MPa√m. This indicates a relatively narrow distribution and high consistency within this orientation. For the Z-Y specimens, the average fracture toughness was 65.77 MPa√m ± 3.185, although the spread was wider, with values ranging from 61.93 MPa√m to 70.91 MPa√m, suggesting greater variability. Z-X specimens showed a slightly lower average toughness of 64.37 MPa√m ± 1.075, with values between 63.54 MPa√m and 66.49 MPa√m. Finally, the X-Z specimens demonstrated the lowest toughness, with an average of 63.10 MPa√m ± 0.972 and a relatively tight range of 61.92 MPa√m to 64.12 MPa√m.

Figure 8 (b) provides a graphical comparison of the as-built and machined fracture toughness values across all orientations. In general, machining led to an improvement in fracture toughness for most specimens. The Z-X specimens showed an increase from 63.54 MPa√m in the as-built condition to 65.2 MPa√m after machining. A similar trend was observed for the Z-Y specimens, where the toughness improved from 64.48 MPa√m (as-built) to 67.06 MPa√m (machined). X-Z specimens also benefited from machining, with values increasing from 62.08 MPa√m to 64.12 MPa√m. Interestingly, the Y-Z specimens deviated from this trend: the as-built specimens had a slightly higher average fracture toughness (66.06 MPa√m) compared to the machined ones (65.56 MPa√m). Overall, the average fracture toughness across all orientations was found to be 64.76 MPa√m ± 2.444, reflecting the relatively high and consistent toughness of EB-PBF Ti6Al4V material.

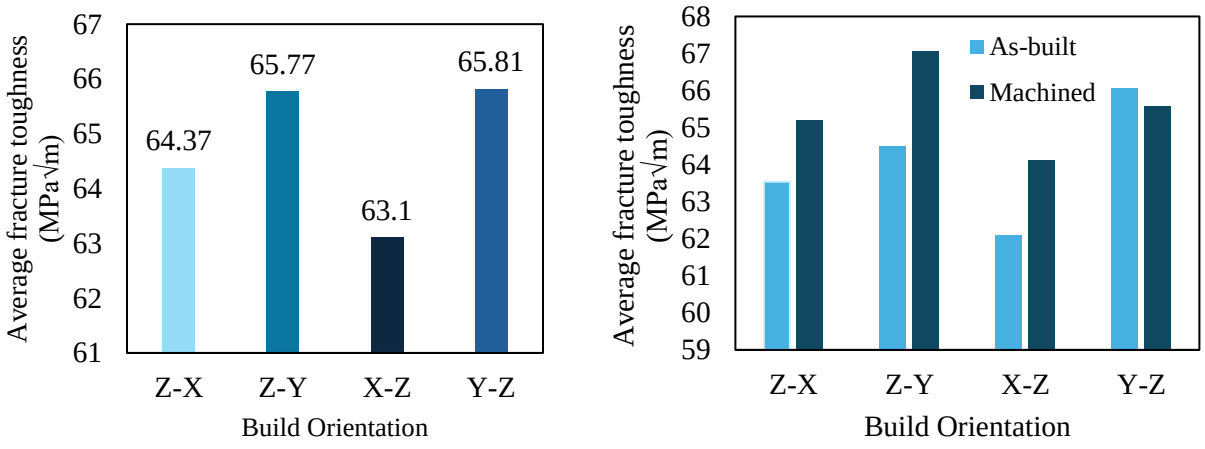

Figure 8. (a) Graph depicting the Fracture Toughness of different build orientations (b) Graphical comparison between the as built and machined Fracture Toughness of different build orientations

2.3.2 Topography and Quantification of Shear Region

Figure 9 shows a two-dimensional optical picture of a fracture specimen. The picture clearly shows the various regions of a fractured surface: Notch region, Pre-cracking region, Shear region and cracking region. The three-dimensional surface profiles of the fractured regions of EB-PBF Ti6Al4V specimens for all four build orientations are shown in Figure 10. The fracture surfaces show distinct shear features near the edges, which are evident as either continuous shear lips or intermittent shear dips across the counter-fracture pieces. The degree of roughness and the morphology of these shear regions visibly vary with build orientation, with some orientations showing a more rugged and dimpled topography compared to others. It is important to note that the shear dips mentioned in this study are the lowered or recessed region on the opposite side of the fracture surface relative to the shear lip.

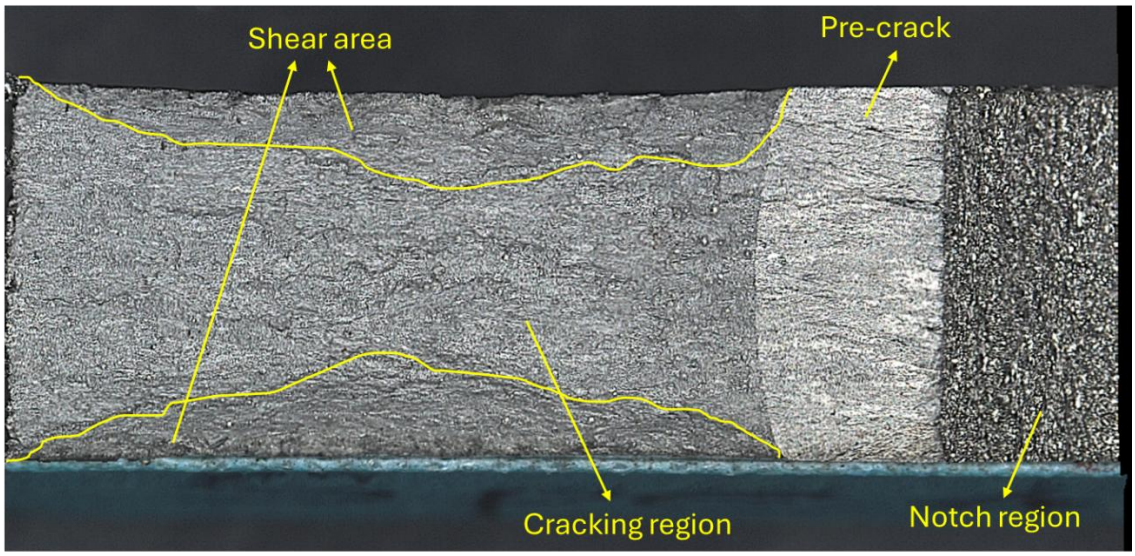

Figure 9. Surface topography of the fractured specimen

The average shear area for each orientation is presented in Figure 11(a). Among the four orientations, Z-X specimens exhibited the highest average shear area of 80.76 mm^2 ± 20.4, with values reaching above 100 mm^2 in some cases. This was followed by Z-Y specimens with an average value of 63.89 mm^2 ± 10.71. The Y-Z and X-Z specimens demonstrated significantly smaller shear areas of 35.35 mm^2 ± 17.47 and 42.52 mm^2 ± 9.71 respectively. These differences in the shear region could suggest variations in plastic energy absorption depending on the build direction. The available fracture area beyond the notch was ~160 mm^2.

The average shear widths for each orientation are summarized in Figure 11(b). Similar to the trend seen in shear areas, Z-X specimens again recorded the widest average shear width of 4.48 mm ± 1.134. This is notably higher than the X-Z and Y-Z specimens, which had the narrowest shear widths averaging about 2.36 mm ± 0.539 and 1.964 mm ± 0.97. Z-Y specimens occupied an intermediate average of 3.549 mm ± 0.595. In general, the Z-oriented specimens (Z-X and Z-Y) appear to undergo greater plastic deformation during fracture, as reflected in both the magnitude of their shear areas and the shear widths.

Figure 11(c) shows the average shear lip and average shear dip angles for different build orientations. Y-Z specimens had the highest average shear lip and shear dip angles of 138.45° ± 4.17 139.42° ± 4.15. They were followed by Z-Y and X-Z which had an average shear lip angles of 136.85° ± 4.4 and 134° ± 4.51 respectively. For shear dip angle, the trend was slightly different. The Y-Z specimens were followed by X-Z and Z-Y specimens, with and average value of 138.55° ± 2.18 and 137.21° ± 4.1 respectively. Z-X specimens had the lowest average shear lip and shear dip angle of 132.55° ± 4.74 and 133.6° ± 2.19 respectively. The fracture surfaces either have shear lips or shear lips as evident in Figure 10 and therefore the shear lip angles and shear dip angles have been presented separately for better interpretation.

Figure 11(d) shows the average shear lip height across different build orientations. Following the trend of shear area and shear width, the Z-X specimens had the highest average shear lip height of 2595.77 mm ± 365.55. Z-Y specimens had the average shear lip height of 2050.49 mm ± 199.35. There was barely any difference between the average shear lip heights of X-Z and Y-Z specimens. The measured values were 1282.88 mm ± 440.6 and 1306.48 mm ± 404.89 respectively.

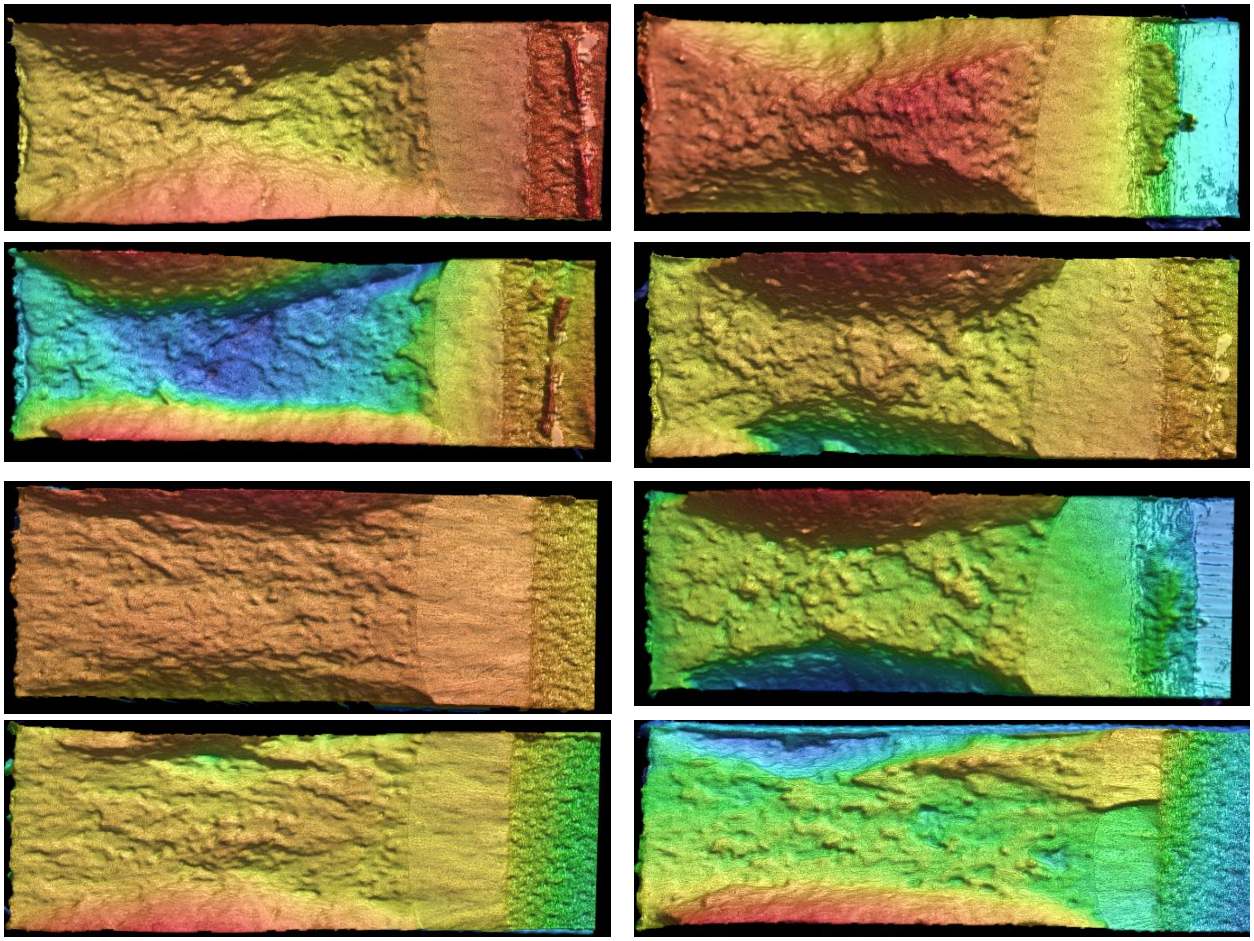

Figure 10. Representative color plots of the fracture surfaces showing fracture topography

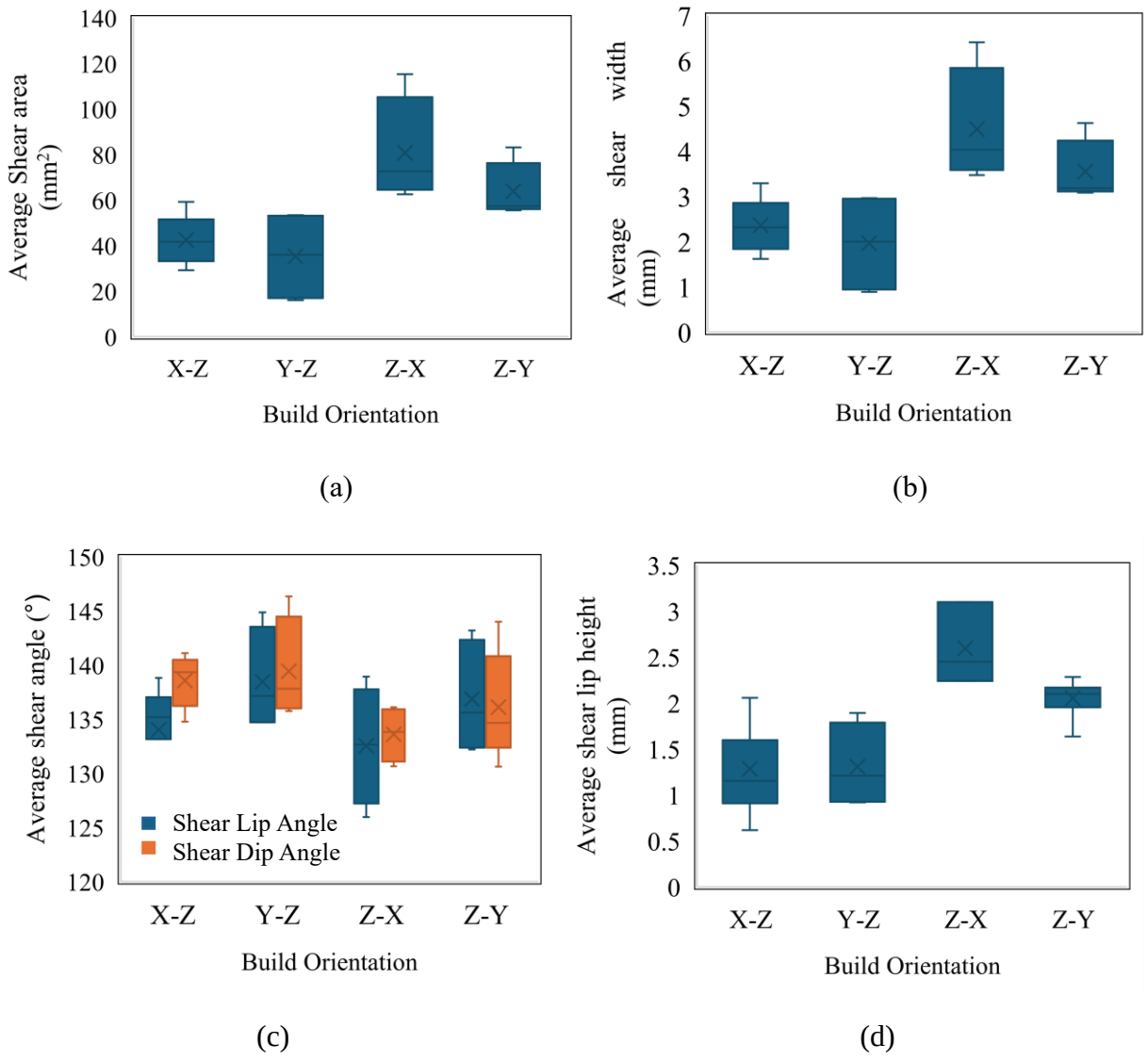

Figure 11. Variation of (a) Average Shear area, (b) Average Shear width, (c) Average shear angle, and (d) Average shear lip height, with respect to build orientations

2.3.3 Surface Roughness

Table 3 presents the surface roughness parameters of the fractured regions for all four orientations. The values characterize the roughness of the surface asperities, excluding the primary shear areas. Among the orientations, the Z-X specimens exhibited the highest average Sa value of 27.32 µm, followed by the Z-Y specimens with 24.54 µm. The X-Z and Y-Z specimens had slightly

lower Sa values of 21.52 μm and 20.92 μm, respectively. A similar trend is observed for the Sq parameter (root mean square roughness height), where Z-Y specimens showed the highest Sq value of 387.14 μm, indicating a rougher surface texture compared to other orientations.

The Sz values (maximum height of the surface) ranged from 28.79 μm for the Y-Z specimens to 35.82 μm for the Z-X specimens. Sp (maximum peak height) was highest for the Z-Y specimens at 236.41 μm, whereas Sv (maximum valley depth) was greatest for the Y-Z specimens at 174.34 μm. Notably, the Z-X and Z-Y specimens demonstrated higher surface roughness values across most parameters compared to the X-Z and Y-Z specimens. As seen in Figure 10, the surface topography of the Z-oriented specimens (Z-X and Z-Y) appears more rugged and uneven, suggesting more energy dissipation during fracture. Conversely, the X-Z and Y-Z specimens exhibit slightly smoother and less rugged surface features, indicative of relatively more brittle fracture behavior.

Table 3. Surface Roughness parameters of different build orientations

Orientation	Sa (μm)	Sq (μm)	Sz (μm)	Sp (μm)	Sv (μm)
X-Z	21.52	345.99	30.14	183.47	162.52
Y-Z	20.92	363.78	28.79	189.44	174.34
Z-X	27.32	362.17	35.82	205.10	157.07
Z-Y	24.54	387.14	33.38	236.41	150.73

2.4 Discussion

The fracture toughness behavior of EB-PBF Ti6Al4V across different build orientations reveals important insights into the anisotropic mechanical behavior induced by the AM process. Among the four orientations examined, the Y-Z specimens demonstrated the highest and most consistent

fracture toughness values suggesting an orientation-sensitive crack propagation mechanism, likely influenced by the layer-wise nature of EB-PBF processing and potential interlayer bonding imperfections. Despite having a slightly lower average fracture toughness than Y-Z, the Z-Y and Z-X specimens exhibited the largest variation in toughness values. This variability may arise from the part's microstructure and the alignment of α-laths and prior β-grains. The EB-PBF specimens exhibit a basketweave α+β microstructure with columnar prior β-grains running parallel to the build direction from bottom to top of the built specimens. For, Z-Y and Z-X specimens, the crack plane is perpendicular to the build direction and also the prior β-grains. This means that the crack travels across the prior β-grains which results in higher energy absorption and greater fracture toughness [26]. Notably, the X-Z specimens consistently recorded the lowest toughness due to the propagation of crack through α+β grains and parallel to prior β-grains. The relatively lesser resistance from the α+β grains makes it easier for the crack to propagate further and therefore results in less absorption of the fracture energy. In all, there was less than ~15% variation in the fracture toughness values of the specimens regardless of the orientation

This data is consistent with the published literature. Mojib et. al. reported the average fracture toughness of 65 MPa√m with Z-X specimens showing better performance than X-Z ones [12]. Dzugan et. al. found the fracture toughness of Z-X specimens to be more than that of X-Z ones, and the measured fracture toughness values were also comparable [27]. Cain et. al. also reported the same trend for their SLM specimens although the overall fracture toughness values were significantly lower which can be attributed to the inherit defects and the residual stresses in the SLM process [18].

The influence of post-processing through machining was generally positive, as evident in Figure 8(b), where most orientations showed an increase in fracture toughness. This enhancement can be attributed to the removal of surface defects, residual stress relaxation, and improved surface integrity [28]. These surface features act as stress concentrators and potential crack initiation sites. By eliminating them, machining reduces the likelihood of premature crack initiation and allows the material's intrinsic fracture resistance to dominate. Additionally, machining can help alleviate residual tensile stresses near the surface that arise from rapid cooling during the layer-by-layer fabrication process. These stresses, if left unaddressed, can contribute to early crack propagation. Improved surface finish and geometric consistency, especially around notched regions, also promote more stable crack growth during fracture toughness testing. The exception was the Y-Z specimens, which exhibited a slight reduction in toughness post-machining. This suggests that machining may sometimes alter local microstructural conditions in ways that do not always benefit material performance but also highlights an interplay of other factors such as mechanical properties and build parameter inhomogeneities in the fracture behavior of the AM specimens.

Fractography analysis further supports these observations. The Z-X and Z-Y specimens displayed larger shear areas, wider shear widths, and higher shear lip heights, indicating greater plastic deformation before fracture. These features are typically associated with ductile fracture behavior, aligning well with their higher surface roughness parameters (Sa, Sq, Sz). The rugged and dimpled fracture surfaces observed for Z-oriented specimens further reinstate the idea of more energy-absorbing fracture paths, potentially due to microstructural orientations that facilitate plasticity.

Conversely, the Y-Z and X-Z specimens, while mechanically strong, showed smaller shear regions and narrower shear widths, reflecting more brittle fracture tendencies. This brittle response is supported by their smoother surface profiles and relatively lower roughness parameters.

The measured shear lip and dip angles provide additional insight into the fracture mechanics. Y-Z specimens exhibited the highest average angles. Relatively higher shear angle in horizontal specimens can be perceived as faster crack propagation as the crack is propagated through/along prior-β grains direction. The possibility of crack propagation along the prior β-grains boundary is much higher in Y-Z and X-Z specimen, thereby possibly making the crack propagation comparatively little easier. Z-X specimens, on the other hand, had the lowest angles. In Z-X specimens, the prior β-grains are split perpendicular their build direction. This leads to a greater resistance from the material against crack propagation, leading to higher energy absorption and smaller shear angles, promoting ductile fracture.

The surface roughness parameters from Table 3 further complement the findings. Higher values of Sa and Sq in Z-oriented specimens correspond to the rugged fracture morphology and are indicative of higher energy absorption. In contrast, smoother surfaces in X-Z and Y-Z specimens correlate with lower plastic deformation and, potentially, increased susceptibility to brittle fracture, despite the latter's high toughness. Specimens with larger and wider shear regions exhibit more rugged, uneven topographies with greater variations in height across the surface, while specimens with lower shear values show comparatively flatter and less contoured surfaces. These observations further support the relationship between build orientation and the fracture behavior of EB-PBF Ti6Al4V, emphasizing the orientation-dependent ductility and crack propagation characteristics of the material.

In summary, the findings highlight that fracture toughness in EB-PBF Ti6Al4V is a function not only of build orientation but also of surface condition and underlying microstructural features. Z-oriented builds tend to favor ductility and energy absorption. These insights are critical for

optimizing the design and post-processing of additively manufactured components for structural applications where fracture resistance is paramount.

2.5 Conclusions

- Y-Z specimens showed the highest average fracture toughness (~65.81 MPa√m), while X-Z specimens had the lowest (~63.10 MPa√m), indicating orientation-dependent mechanical performance.
- Z-X and Z-Y specimens exhibited larger shear areas, wider shear lips, and greater shear lip heights, suggesting higher plastic energy absorption compared to X-Z and Y-Z orientations.
- Z-oriented specimens (Z-X and Z-Y) demonstrated higher surface roughness values (e.g., Sa and Sq), indicative of more rugged fracture topographies and increased ductile behavior.
- Most specimens showed increased toughness after machining due to the removal of surface defects and improved surface integrity. The only exception was Y-Z, which slightly decreased post-machining.
- Greater shear areas and higher shear lip angles were associated with higher fracture toughness, emphasizing the role of plastic deformation in crack resistance.

Chapter 3 Charpy Impact Toughness/ Notch Toughness

3.1 Introduction

While tensile and fracture toughness properties are crucial indicators of a material's mechanical performance, they do not address the material's behavior in sudden impact scenarios, where localized strains and strain rates are extremely high. The notch toughness under impact loading is an important mechanical property, which refers to the amount of energy that a material can absorb before rupture under dynamic loading. Charpy impact testing is most common for metals and provides a convenient manner to explore the dynamic toughness and notch sensitivity [29]. These properties can be sensitive to microstructure and defects, which are concerns in PBF processes in general [30,31].

Several studies have been reported on the notch toughness behavior of L-PBF Ti6Al4V. However, the number of studies reported on EB-PBF of Ti6Al4V is limited. Hrabe et. al. studied the effects of internal porosity and crystallographic texture on the miniaturized Charpy impact test on EB-PBF specimens in the as-built condition and after Hot Isostatic Pressing (HIP) built with horizontal and vertical orientations [32]. Results showed that the HIP treatment reduces internal porosity and increases the α lath thickness, which improved the absorbed energy. Their results emphasized that crystallographic texture and grain morphology influence energy absorption, with crack pathways crossing prior-β grain boundaries contribute to higher energy. Variations in texture across conditions highlighted its critical role in absorbed energy behavior. In another study involving miniaturized Charpy specimens of Ti6Al4V produced by EB-PBF, the metal showed better or equivalent impact toughness after HIPing, and showed no effects due to notch sensitivity/configuration [33]. Bruno et. al. investigated the effect of build orientation (0°, 30°, 60°, 90°) on the microstructure and mechanical performance of Ti-6Al-4V parts fabricated by

ARCAM S12 EB-PBF machine, revealing that horizontal builds exhibit lower ductility and toughness compared to vertical builds in Izod impact testing [34].

Azizideroueiet. al. studied the effects of build orientation (0°, 45°, 90°) and lack of fusion on the Charpy impact energy of EB-PBF Ti-6Al-4V. They reported an increase in the impact energy with an increase in the effective angle between the notch direction and build orientation; LOF facilitated the crack propagation when the notch direction was aligned with the build direction [35]. They also briefly discussed the microstructural influence on the crack paths and reported higher impact energy for vertical specimens. Jeffs et. al. examined the effects of process parameters and build orientation on the notch toughness of EB-PBF Ti-6Al-4V [25]. Their results also show that vertical builds exhibit higher impact energy due to epitaxial grain growth. The beam velocity and normalized energy density influenced microstructure and impact energy relationships, where the influence of beam velocity was more significant.

Grell et. al. studied the effects of oxidation due to powder reuse on the notch toughness of horizontal specimens (XZ - top faced notch; XY- side face notch), and vertical specimens (ZX), and reported a reduction in the toughness which was correlated with lower ductility. The variation in energy absorbed due to build orientation was more dominant in the lower oxidized condition; vertical specimens absorbed a higher amount of energy [36]. Soundarapandiyan reported reduced impact energy with oxidation [37] and increase in the impact toughness of EB-PBF Ti6Al4V with heat treatment [38]. The microstructure of EB-PBF Ti6Al4V, often characterized by α+β phases, porosity, and anisotropic properties due to layer-wise processing, can significantly influence impact toughness.

Most researches on the notch toughness of EB-PBF Ti6Al4V reports the impact energy to failure with very limited mechanical property data and supporting fractographic evaluation. Optical

profilometry is an effective method for analyzing the fracture surface morphology both qualitatively and quantitatively. Hence, in this investigation a detailed evaluation of the fracture surface morphology of EB-PBF Ti6Al4V specimens after Charpy impact testing was conducted and the key surface features were identified. The effects of build orientation were evaluated in relation to surface topography, material properties such as hardness, microstructure, and other mechanical properties, including the predominate process induced defects. Recognizing that the notch toughness is a function of ductility and that the interrelationship is often reflected through characteristic features of the fracture surfaces [39]. The notch toughness and surface topography were discussed considering other mechanical properties i.e., tensile properties, hardness, fracture toughness of EB-PBF Ti6Al4V fabricated in the same system with optimized parameters.

3.2 Materials and Methods

3.2.1 Specimen Fabrication

Charpy impact specimens were built for this investigation by Aditya Koneru (previous lab member) with Ti6AL4V powder that had been used in 20 previous builds. Charpy impact specimens are cuboids with square cross-sections and a notch which lies parallel to the cross-section in the center of one of the rectangular faces. Details regarding the total number of hours accrued in the build chamber or replenishment practiced in these builds were not available. The average powder diameter was about 50 microns with the majority of the powder (> 90% particles) in the range of 45-120 microns. The weight percentage composition of this feedstock is presented in Table 4 [40].

The Charpy impact specimens were built in accordance with ASTM E23 with three different orientations, including Horizontal Side (HS), Horizontal Top (HT) and Vertical (V) as shown in Figure 12 [41]. Horizontal side means the notch is on the side face of the specimen whereas

Horizontal top means the notch is on the top face of the specimen. Ten specimens were built with each orientation in a single build, all with standard geometry (10x10x55mm) with notch depth of 2 mm, angle of 45 degrees, and a notch-tip curvature of 0.25mm (Figure 13). The position and orientation of the specimens inside the chamber were virtually modeled with 6 mm support structures in Materialize Magics software. The build was completed on an ARCAM EBM A2X machine (version 5.0.64), using the default parameters for Ti6Al4V. The default build parameters include beam current =15 mA, max current = 20 mA, beam scan offset = 25 mA, beam speed = 4530 mm/sec, speed function = 45, and preheat temperature = 650°C [42,43]. The successful print with the powder cake was extracted from the build chamber. The specimens were extracted from the powder cake using the powder recovery system (PRS) and were ready for Charpy impact testing. Tensile properties of the metal fabricated with this powder by EB-PBF in the same ARCAM A2X machine and using the same build parameters are listed in Table 5 [39].

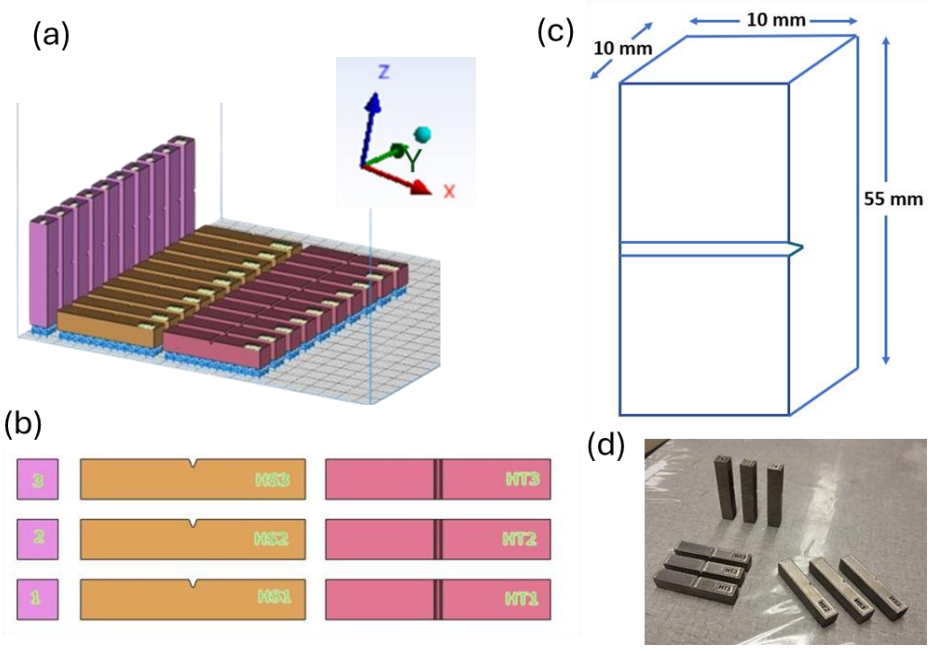

Figure 12. (a) Isometric view of Charpy impact specimens inside the build chamber, (b) Top view of the specimens showing three different notch orientations, (c) Dimensions of the specimen, (d) Few fabricated specimens

Table 4. Weight percentage composition of 20th build cycle Ti6AL4V

Build	Al (wt%)	V (wt%)	O (wt%)	N (wt%)	Fe (wt%)	H (wt%)
20	5.54	3.40	0.269	0.027	0.26	0.0012

Table 5. Tensile Properties of EB-PBF Ti6Al4V specimens at 20 cycles [7]

Orientation	Elastic modulus (GPa)	Yield Strength (MPa)	Utlimate Tensile Strength (MPa)	% Elongation
Horizontal	102 ± 0.8	927 ± 18.9	1010 ± 21.8	4.3 ± 0.25
Vertical	113 ± 5.9	939 ± 7.5	1070 ± 11.3	9.18 ± 0.99

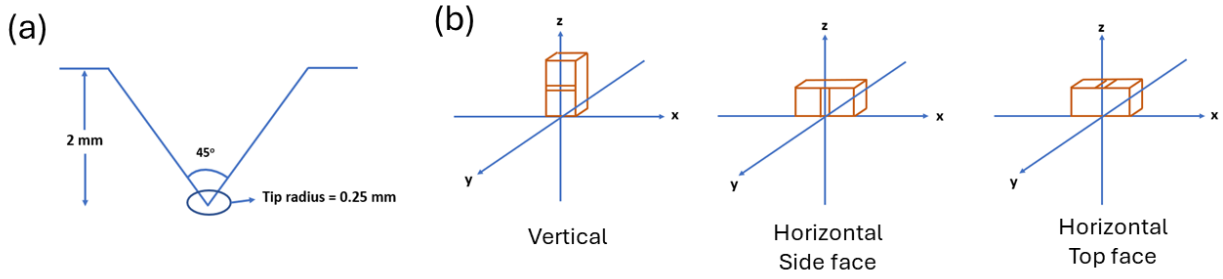

Figure 13. (a) Notch dimensions, (b) Notch orientations with respect to the build plate orientation system

3.2.2 Charpy Impact Testing

The Charpy impact test provides a measure of resistance to fracture under impact loading [29]. The experiments in this investigation were performed using a Satec SI-1K3 (FOB Warren, MI) adhering to the ASTM E23 standard [41]. The absorbed energy is measured as the reduction in the pendulum's potential energy between its first and second maxima during the swing. The impact test set up is shown in Figure 14. The instrument was calibrated prior to each experiment as required for accurate measurements. The Charpy pendulum was raised to the ready position and the tested specimen was placed in the designated slot, supported at both ends on the side opposite the notch. The pendulum, equipped with a one-dimensional striking region, was released to strike the face opposite to the notch, fracturing the specimen. The impact testing method resembles a three point bend test in a beam. The largest force was delivered at the notch, where stress

concentration was highest, and the absorbed energy was determined by the pendulum's reduction in potential energy. The notch sensitivity of the specimens was assumed to remain constant since all specimens had similar geometry. The Charpy impact test evaluates the energy absorbed during fracture, which is calculated as: $E\ (J)\ =\ E_i\ -\ E_f$, where,

$$E_i\ =\ mgR\ (1 - cos\ \beta) \text{ and } E_f\ =\ mgR\ (1 - cos\ \alpha)$$

In the above equations, m is the hammer mass, g is gravitational acceleration and R is the pendulum radius [44].

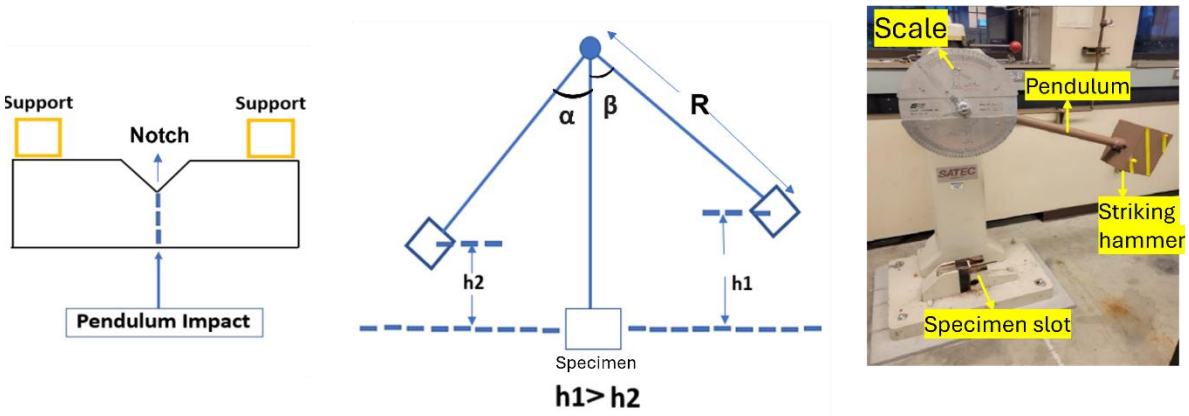

Figure 14. Pictorial representation of Charpy impact testing and tester with a specimen loaded.

3.2.3 Profilometry

An optical profilometer (Keyence, Model VR – 3100, Osaka, Japan) was used to capture three-dimensional surface topography of the EB-PBF Ti6Al4V specimens after the impact testing. Optical images and the 3D topography of the relevant surfaces were captured at magnifications between 12x and 180x. The standard surface roughness parameters were calculated for each specimen including Sa (areal roughness height), Sz (10-point height) and Sq (root mean square height). In addition, the Sp (peak height) and Sv (valley depth) parameters were estimated, as well

as the Ssk (skewness) and Sku (kurtosis). In the roughness measurement, the entire cracking area was considered as the reference plane in profiling the surface topography. Topography maps of the fractured specimens were created to support identification of the dominant characteristics.

3.2.4 Shear area analysis

The shear area for each fracture surface was measured from the high-resolution color maps using Keyence optical profilometer (Model VR – 3100, Osaka, Japan) and ImageJ software (version 1.46r). The known specimen dimensions were used to calibrate the scale within the software, ensuring precise area measurements. For each fracture surface evaluated, the left-side and right-side shear regions were carefully outlined and the sum of these two areas served as the total shear area. To account for potential variations in measurements and minimize errors, the average shear area was calculated for the two sides of each broken specimen. The shear areas were then averaged across the 10 specimens of each build orientation to reflect the effects of build orientation on fracture behavior. This approach ensured consistency and minimized errors caused by manual selection or surface irregularities. The measured shear area is the projected area as seen from the top view of the fractured surface rather than the actual 3-D shear area. Using the projected shear area, the shear angle and the trigonometric principals, the actual shear areas and consequently the shear widths of the specimens were calculated, which is a more comprehensive reflection of the shear mechanisms. By combining advanced imaging techniques with precise software-based analysis, this study provides valuable insights into the relationship between Charpy impact toughness, fracture mechanics and build orientation in EB-PBF Ti6Al4V alloys. In addition, the shear lip dimensions (length and height) were calculated from the 3D topography (Figure 15). Jeffs et. al. also used shear lip width to discuss the fracture behavior of EB-PBF Ti6Al4V [25]. Two more indices have been introduced and measured in this study - Maximum Continuous Shear Lip

Length (MCSL) and Maximum Continuous Shear Dip Length (MCSD). MCSL and MCSD are defined as the maximum length of the continuous shear lip and shear dip in a fractured specimen. The roughness of the fractured areas (cracking area) has also been measured excluding the shear lip and shear dip areas. It is important to note that the shear dips mentioned in this study are the lowered or recessed region on the opposite side of the fracture surface relative to the shear lip. The shear angle of the shear lips was calculated considering the vertical cracking region as a reference.

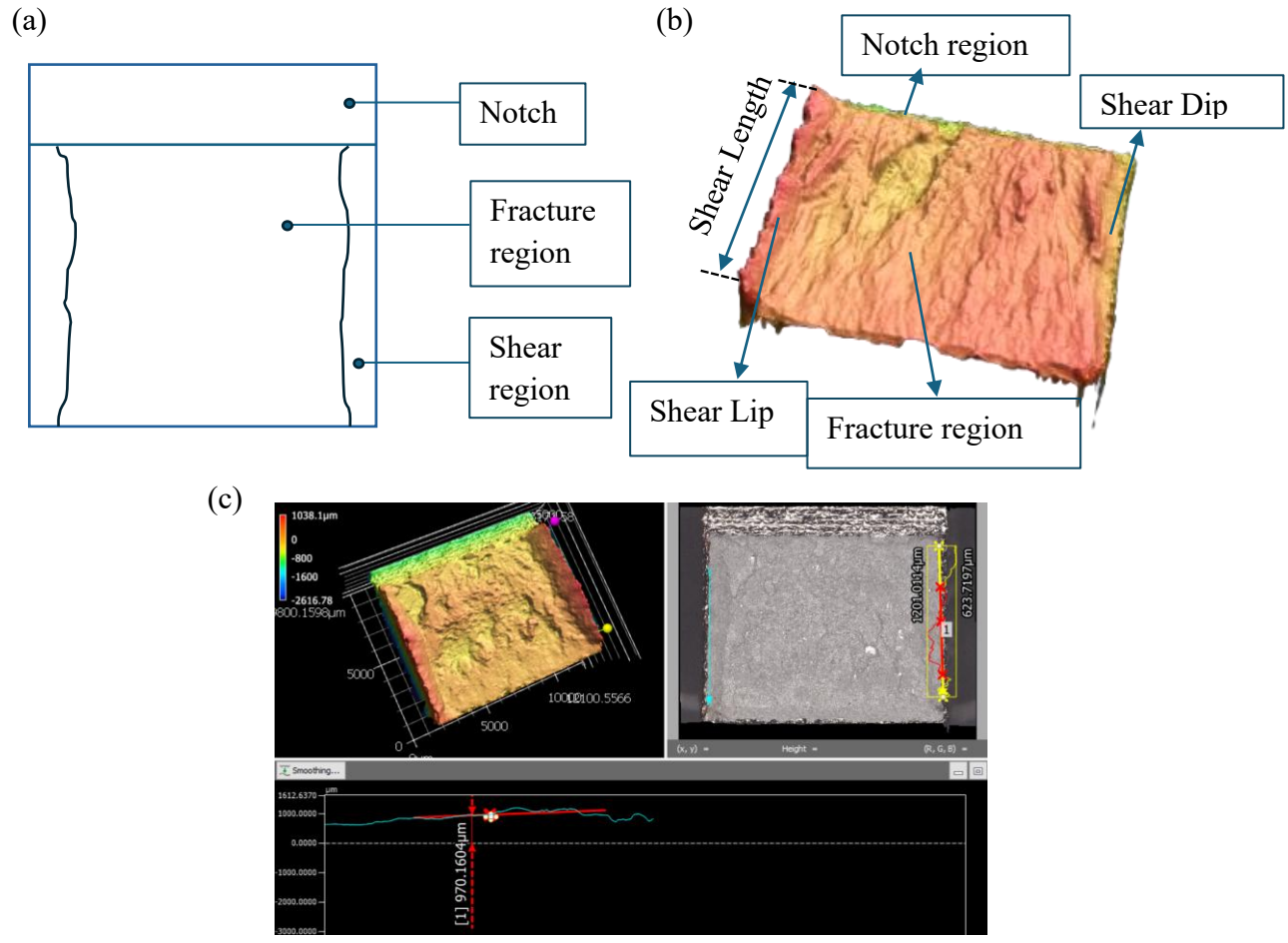

(d)

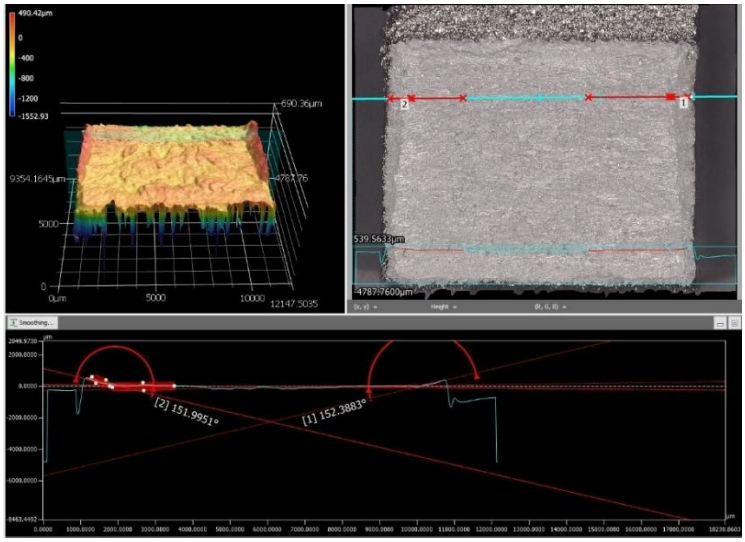

Figure 15. (a) Cracking and shearing region of a fracture surface, (b) Surface topography of fracture region, (c) Shear lip height measurement, (d) Shear angle measurement

3.2.5 Microstructure and microhardness

Selected specimens underwent sectioning, mounting, and polishing to evaluate the microstructure and measure the microhardness. Out of 30 specimens, 11 representative specimens were evaluated. One half of each specimen was mounted in a graphite-based mounting medium using a conventional mount press. Polishing was performed using an EcoMet 30 semi-automatic polisher (Buehler, IL). The process began with sequential grinding using silicon carbide (SiC) papers of 240, 400, 600, 800, and 1200 grit. Each grit was applied for 3 minutes at 300 RPM under a polishing load of 20 N per mount, with continuous water coolant. Fine polishing was peformed using a 1 mL DiaLube diamond suspension (~3 μm particle size) for 5–6 minutes without additional water. To achieve a mirror-like surface, a final chemical attack polishing step was performed using a mixture of 0.5 mL NH4OH and 2 drops of H2O2 in 10 mL colloidal silica (~0.05 μm silica particle size) for 5 minutes. At each stage, the polished surface was assessed through visual inspection and optical microscopy. The microstructure was revealed by etching the final polished specimens with Kroll's reagent (2% HF, 6% HNO3, and 92% H2O) for 8 seconds.

Optical images were then captured using an optical microscope (Nikon BXZ5150, Japan) at magnifications of 50x, 100x, 200x, 500x, and 1000x. For microhardness measurements, a micro-indenter (LM247AT, LECO Corp., MI) equipped with AMH43 software (LECO Corp., MI) was used, following ASTM E92 standards. Each specimen underwent at least 15 indentations, with an applied force of 100 g for 13 seconds per indentation. To comply with ASTM E92 guidelines, the indentation sites were examined before and after testing, ensuring a minimum spacing of 2.5 times the indentation diagonal (2.5d) between adjacent impressions to prevent interference.

3.2.6 Scanning Electron Microscopy

The detailed features on the fractured surfaces were captured with scanning electron microscopy (SEM, JEOL JSM 6010PLUS/LA). Prior to the SEM, the specimens were cleared of any debris with a nitrogen gas gun. Images were obtained for magnifications between 30x-400x. Two images of each of the three build orientations were analyzed using the ImageJ software (Figure 16) to estimate the percentage area of porosity with respect to the total area of the fractured surface.

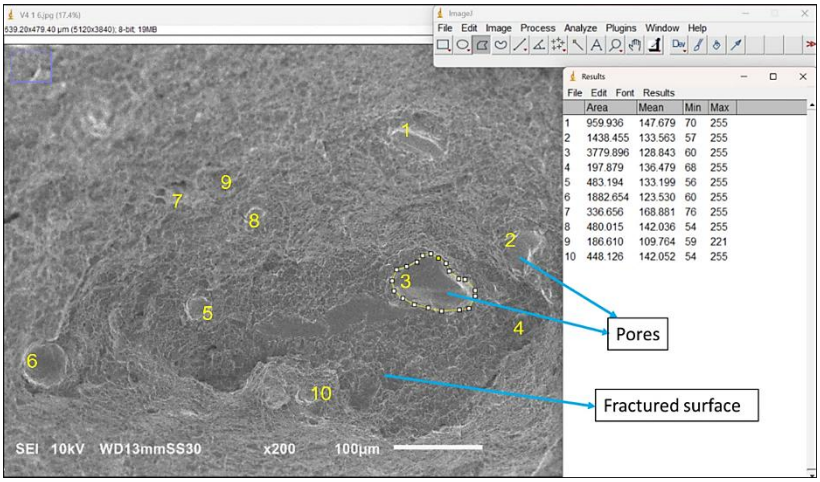

Figure 16. Calculation of pore area and porosity percentage using ImageJ software (numbers in yellow represent the pores visible by the naked eye)

3.3 Results

3.3.1 Impact Energy

The energy to fracture of the EB-PBF specimens is presented in Figure 17(a) for all three orientations. The horizontal specimens with top-faced notch (HT) exhibited an average impact energy of 15.48 J ± 0.58, while the individual values ranged between 14 J and 17 J. The horizontal specimens with side-faced notch (HS) had an average impact energy of 15.94 J ± 0.75, where the energy absorption varied from 15 J to 17.75 J. Overall, the horizontal specimens regardless of notch orientation showed impact energy of 15.71 J ± 0.93. The vertical specimens (V) exhibited an average impact energy of 22.86 J, where the energy absorption ranged from 9.75 J to 54.5 J. As evident, the vertical orientation exhibited higher absorbed energy than both the horizontal orientations. Between the HS and HT groups, the HS specimens exhibited slightly higher (~2.97%) average impact energy, which highlights that there was negligible difference in the notch toughness of the metal with horizontal orientation regardless of notch face. The variation in impact energy variation of the horizontal specimens with respect to location in the build chamber are presented in Figure 17(b) and Figure 17(c). Overall, the horizontal HT specimens show a slight increase in energy to fracture with radial distance; no trend is observed in the HS specimens. There is no apparent variation in energy to facture along the X and Y axes. When comparing the impact toughness (notch toughness), the V specimens showed higher average impact toughness of 0.285 J/mm^2 ± 0.188 followed by the HS and HT top specimens which had average impact toughness of 0.199 J/mm^2 ± 0.009 and 0.193 J/mm^2 ± 0.013, respectively.

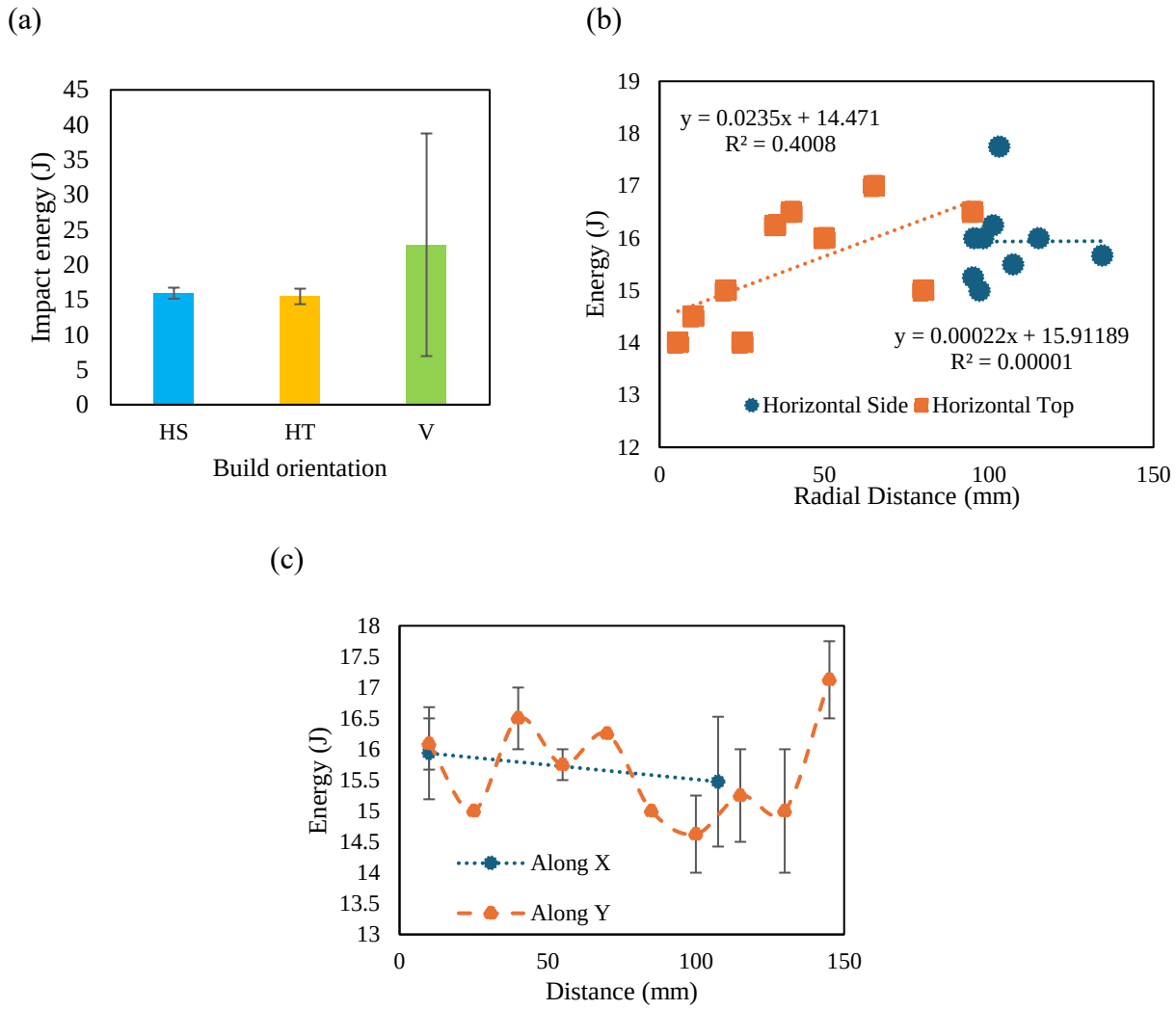

Figure 17. Impact energy variation with respect to (a) different build orientations, (b) radial distance, (c) along X and Y axis

3.3.2 Topography and Quantification of Shear Region

Figure 18 shows the three-dimensional topography of six representative fractured EB- specimens from each build orientation. Shear lips and shear dips can be seen on the edges of the specimens. The measured shear lip area, shear lip height, and impact energy absorbed are provided in the legend below each specimen. The shear areas were mostly found on the edges of both the pieces, either in the form of shear lips or shear dips. The shear lips were found to be either continuous or discontinuous. In the location where the shear lips are discontinuous (shear dips), shear lips are

found on the counter pieces. Results for the fracture surface shear parameters are presented in Figure 20. Overall, the shear area was most predominant for the vertical specimens as evident in the average actual shear areas in Figure 20(a). The designed cross-sectional area available to fracture beyond the notch was ~80 mm^2. Thus, ~13.67%, ~17.68% and ~24.11% of the total fractured area respectively HS, HT and vertical specimens belong to the shear region

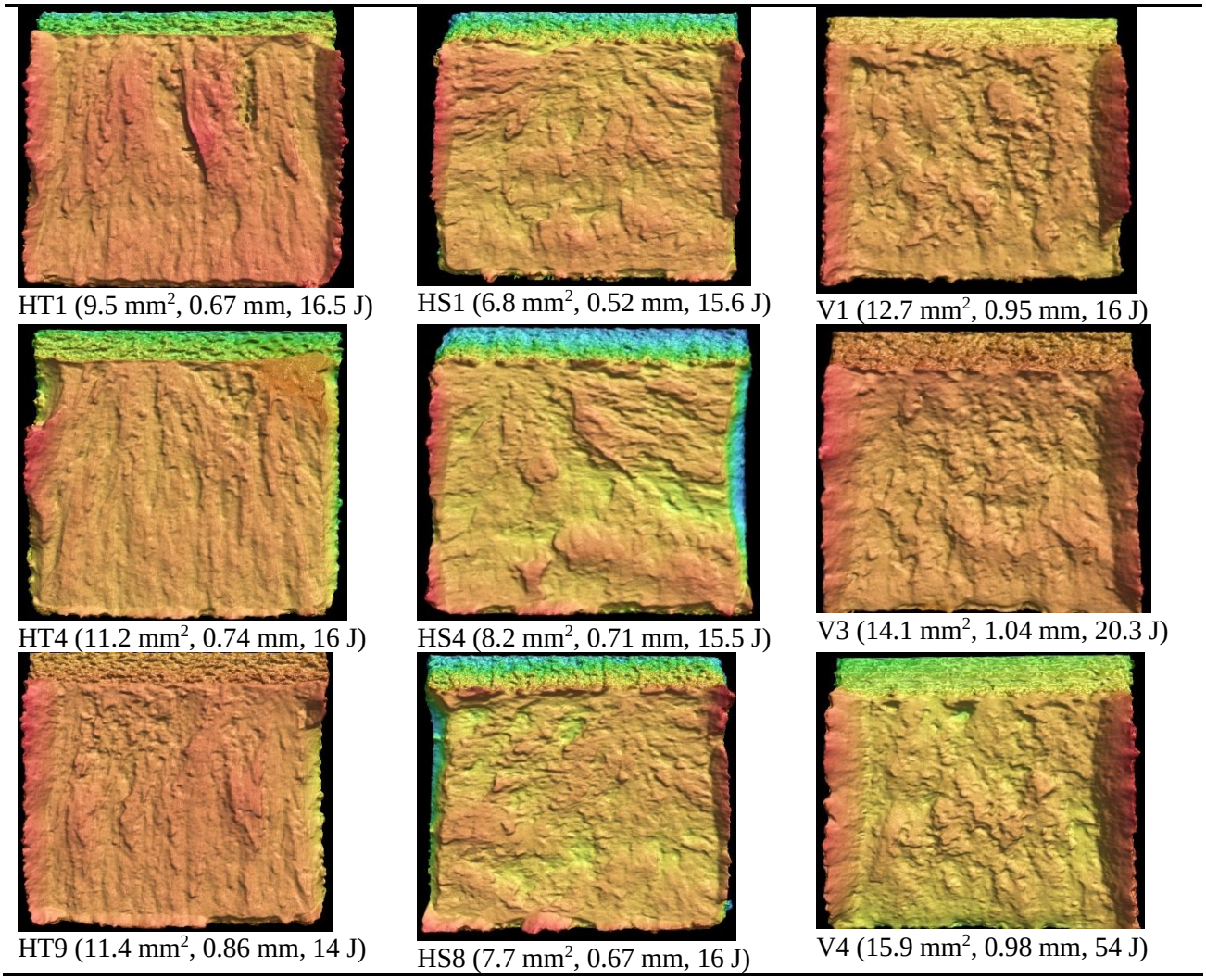

Figure 18. The surface topography of the fractured EB-PBF Ti6Al4V

Figure 20(c) presents average the shear lip height variation with respect to build orientation. The areas affected by the dominant shear regions at the edges and the notch were excluded. The average shear lips heights for HS, HT and V specimens are 671 μm, 758 μm and 960 μm; the maximum values being 982 μm, 1036 μm and 1276 μm, respectively. The average shear lip height for horizontal specimens is 714 μm. The shear lip heights for vertical specimens are consistently higher than the horizontal specimens. Overall, the average shear lip height in vertical specimens is ~34.78% higher than horizontal specimens.

The shear lip widths of the vertical specimens are also higher than horizontal specimens. As per the calculations, the average shear widths are 0.76 mm ± 0.082, 1.02 mm ± 0.131 and 1.34 mm ± 0.125 for HS, HT and V specimens respectively (see Figure 20b)). The higher the shear area and the shear lips height, the higher is the energy absorption, which is discussed in detail in the discussion section. The shear angles were also calculated and reported to be respectively 43.52°, 42.02°, and 44.63° for HS, HT and Vertical specimens with an average of 43.39°± 1.39° regardless of orientation. The average printed notch radius of HS, HT and vertical specimens are respectively 0.58 mm, 0.47 mm, 0.46 mm, and the average printed notch radius is 0.5 ± 0.06 mm for all specimens regardless of the orientation (see Figure 19). The average Maximum Continuous Shear Lip Lengths (MCSL) for HS, HT and V specimens are 5.412 mm, 6.322 mm and 7.067 mm respectively. This shows that the shear lip lengths account for approximately 54% (HS), 63% (HT) and 70% (V) of the specimen width in the specimens. Similarly, the average Maximum Continuous Shear Dip Length (MCSD) for HS, HT and V specimens are 5.519 mm, 6.506 mm and 6.983 mm respectively (see Figure 20(d)).

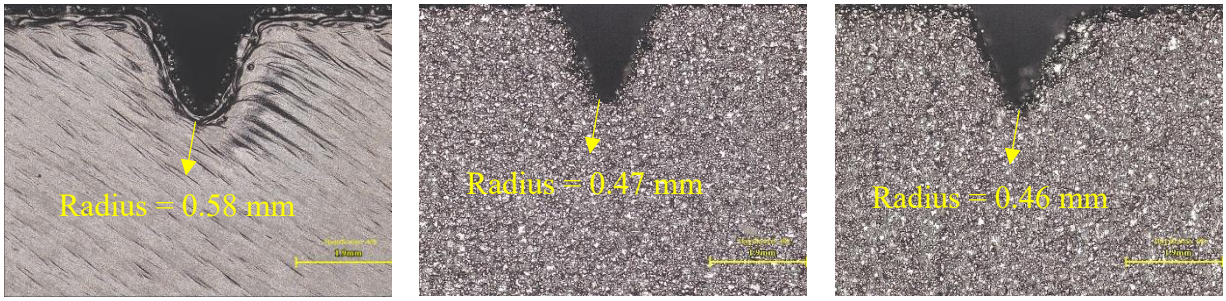

Figure 19. Printed notch radius of EB-PBF Ti6Al4V of different build orientations – (a) HS, (b) HT and (c) V

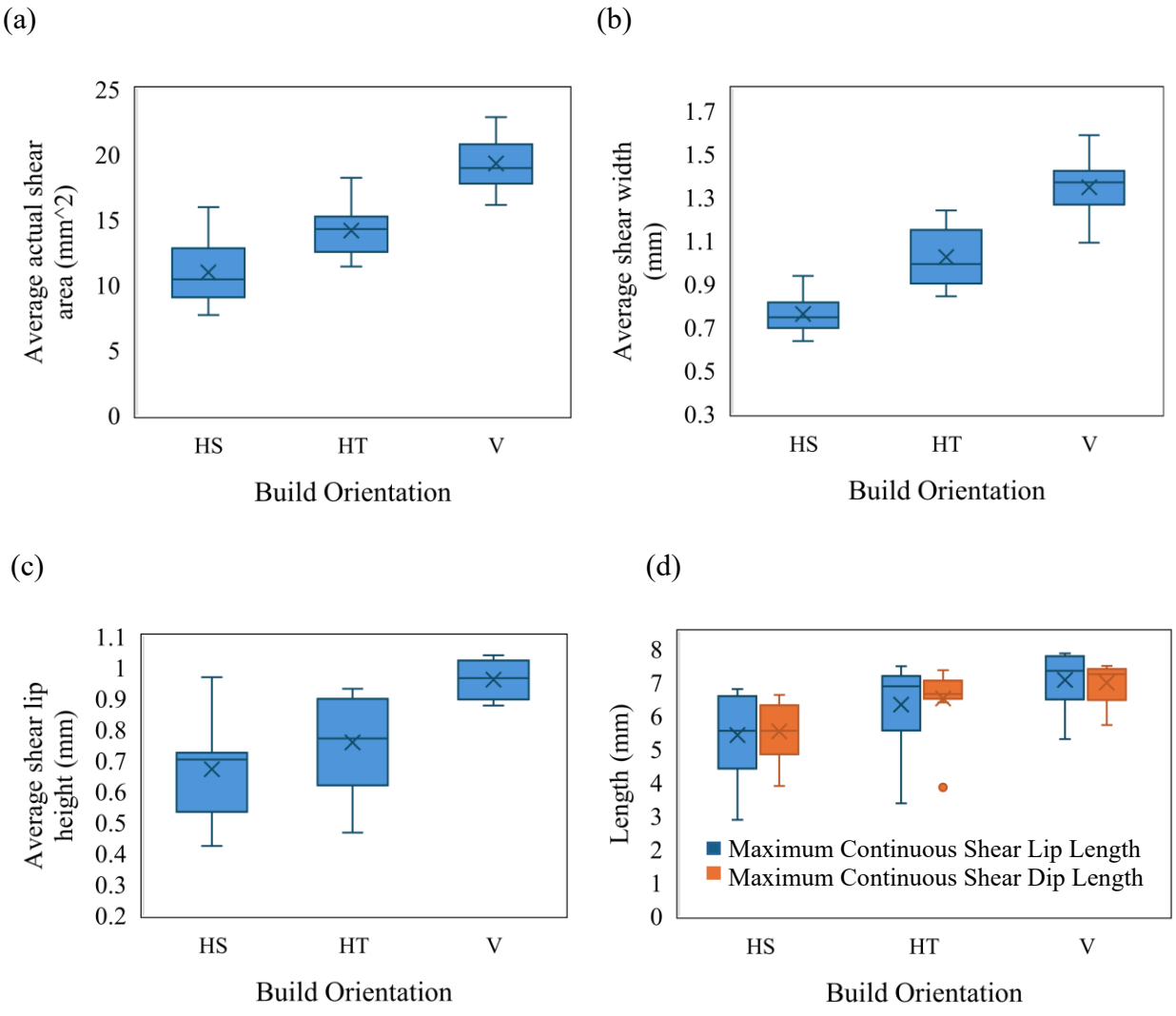

Figure 20. Variation of (a) Average actual Shear area, (b) Average Shear width, (c) Average shear lip height, and (d) MCSL and MCSD lengths with respect to build orientations

3.3.3 Surface Roughness

Table 6 represents the surface roughness parameters of the fractured region. The values represent the roughness of the surface asperities excluding the shear area. The mean Sa values are 18.65 μm and 21.41 μm, respectively for the H and V specimens. The mean Sv values are 170.01 μm and 164.21 μm, respectively for the H and V specimens. Sv shows the largest difference followed by Sa and Sq (root mean roughness height). The surface roughness of the cracking regions in the vertical specimens is higher than the horizontal specimens. As seen in Figure 18, the surface topography of the vertical EB-PBF Ti6Al4V visually appears more rugged than horizontal specimens, a sign of more ductility. On the other hand, the cracking region surfaces of the horizontal specimens appear slightly less rugged and comparatively flatter than vertical specimens.

Table 6. The surface roughness parameters of the fractured (cracking) area

Orientation	Sa (μm)	Sq (μm)	Sz (μm)	Sp (μm)	Sv (μm)
Horizontal	18.65	25.18	319.83	149.83	170.01
Vertical	21.41	28.80	346.77	182.56	164.21

3.3.4 Microhardness and Microstructure

Microhardness is a subsurface property which represents resistance against deformation and is often proportional to the Ultimate tensile strength in metals [45]. The average microhardness of HS and HT specimens are respectively 355.5 ± 2.9, and 362.3 ± 8.3, where $H_{HS} < H_{HT}$. Overall, the average microhardness of horizontal specimens is 358.9 ± 7.1. Vertical specimens showed the lowest average microhardness of 351.3 ± 3.8. This microhardness trend is consistent with published literature. Although we have not measured α-lath thickness in this experiment, visually, vertical specimens appear to have coarser α-lath thickness. Thus, the hardness of the vertical

specimens is lower than horizontal specimens. Published studies including Jeffs et. al. reported finer α-lath thickness in horizontal specimens compared to vertical specimens [25]. In our previous study on EB-PBF Ti6Al4V [46], α-lath thickness showed a disproportionate relationship with microhardness, which is consistent with Tan et. al. [47] and Sharma et. al. [48]. **Error! Reference source not found.** shows the microstructural pictures of both the horizontal and vertical specimens depicting the crack paths and the columnar β grains. It can be clearly seen that for vertical specimens, the crack propagates through α plus β colonies, crossing prior β grains in the process, indicating trans granular propagation, hence higher impact values. But in the case of horizontal specimens, the crack predominantly travels along the prior β boundaries, leading to reduction in the energy absorption. These findings align with previous research on Ti6Al4V fracture behavior [35].

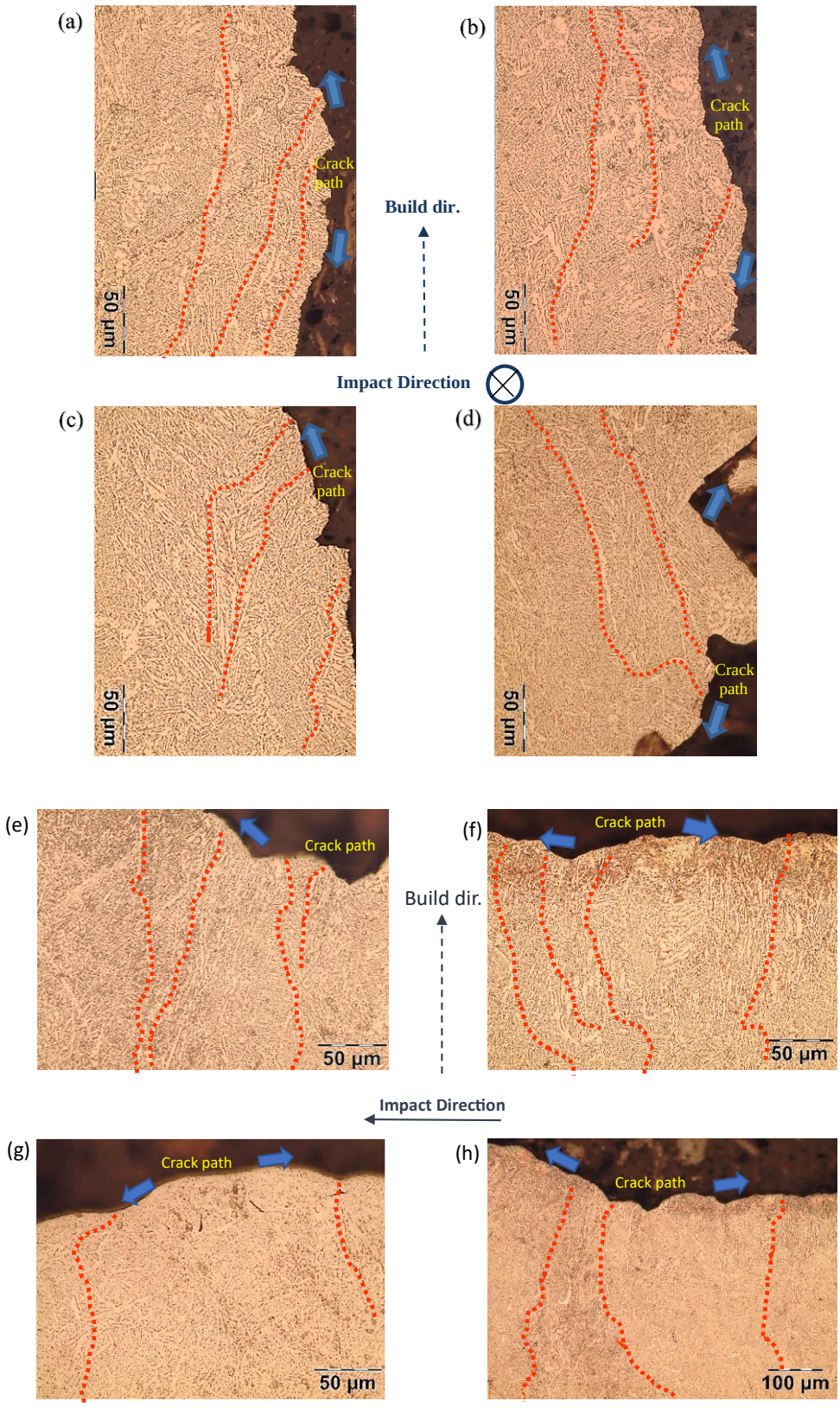

Figure 21. The cracking path and prior - β columnar grains within the microstructure of EB-PBF Ti6Al4V (a-d) horizontal- HT specimens, (e-h) vertical specimen. The prior – β grains are highlighted with red dashed line.

3.3.5 Scanning Electron Microscopy

Figure 22 represents the SEM images of the fractured EB-PBF Ti6Al4V specimens of horizontal (HT) and vertical specimens at multiple magnifications. The fractured micrographs show the presence of process induced defects, i.e., porosity, lack of fusion, and fractured features such as fracture flutes [39]. The porosity can be seen as circular voids, both in horizontal and vertical specimens. These micro-void coalescence as well as fracture flutes can be observed across all specimens. They start to appear more frequently as the powder is reused more and more and since the powder in this study was being used for the 20^{th} time, a lot of porosity defects as well as fracture flutes can be seen in the SEM images. The average percentage of porosity for the fractured surface area for horizontal and vertical orientation is 4.53%, and 1.8% respectively. This clearly shows that the percentage porosity in vertical specimens was about 150% higher than the horizontal ones on their fractured surface. However, this does not represent the actual porosity within the entire horizontal or vertical specimens, which would have been better analyzed using μ-CT analysis. However, the critical defect size increases with power reuse in EB-PBF Ti6Al4V [49]. The fracture flutes, marked by yellow arrows, are also seen in both orientations in Figure 22(d) and Figure 22(h). Flutes are elongated dimples in the geometry and are common to HCP structures. The fracture flutes are signs of ductile fracture and develop from a reduction in slip in the HCP-α phase due to increasing oxygen content in the material [39]. Usually, these flutes tend to form on $\{10\underline{1}0\} < 11\underline{2}0 >$ along α–α and α–β grain boundaries and are also often formed in Widmanstatten microstructures due to the close packing of the α- and β-plates [50].

Horizontal (HT) **Vertical (V)**

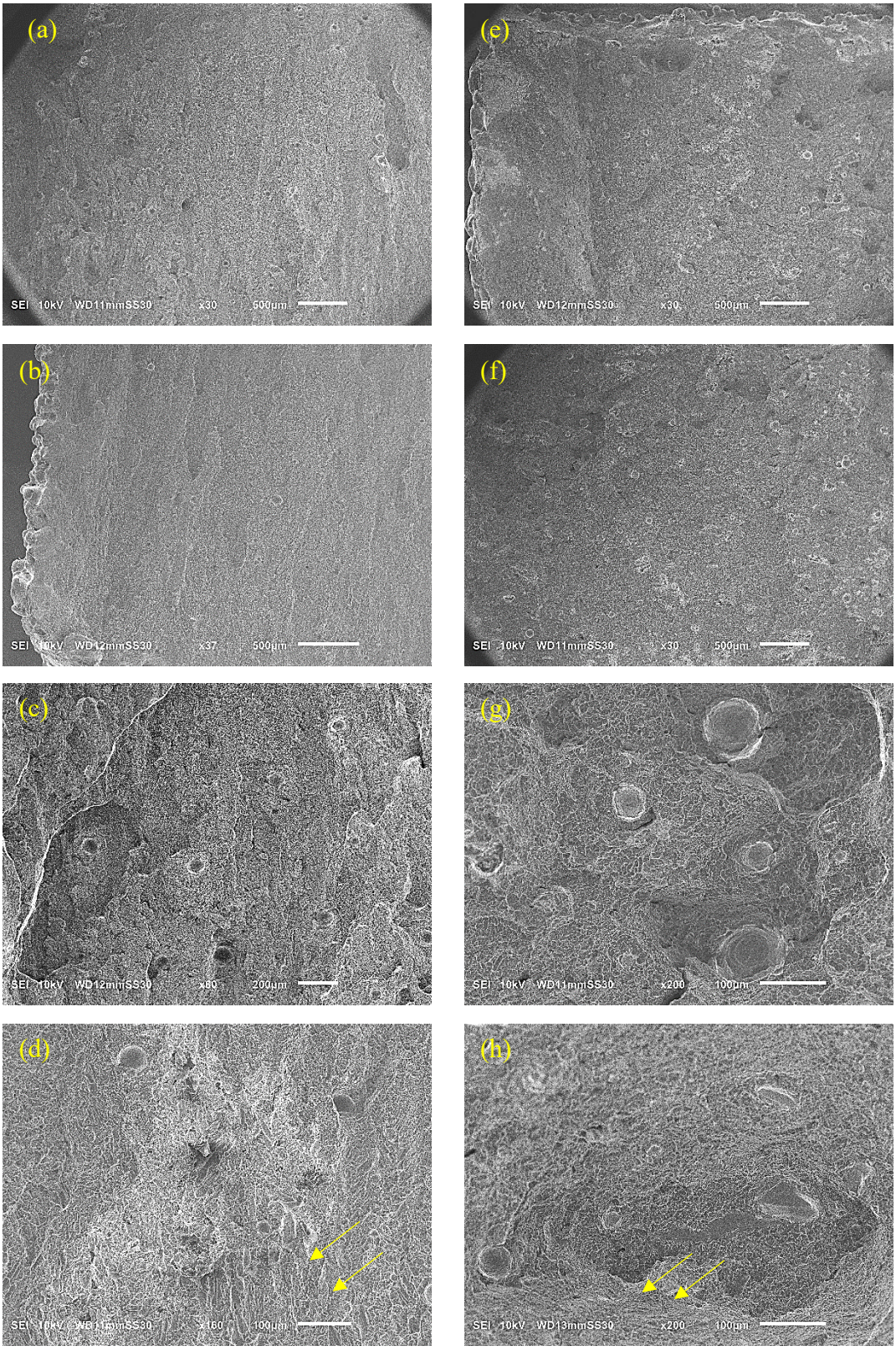

Figure 22. SEM images of fractured EB-PBF specimens: (a) Horizontal (HT) – 30x, (b) Horizontal (HT) – 37x, (c) Horizontal (HT) – 60x, (d) Horizontal (HT) – 160x, (e) Vertical (V) – 30x, (f) Vertical (V) – 30x, (g) Vertical (V) – 200x, (h) Vertical (V) – 200x (yellow arrows highlight fracture flutes)

3.4 Discussion

The EB-PBF Ti6Al4V specimens in as-built conditions show anisotropy in their impact resistance or impact toughness with respect to the build orientation. As mentioned in Section 3.1, the vertical specimens had ~50% higher average impact energy and impact toughness than the horizontal specimens. This suggests enhanced energy absorption due to the crack propagation path. The impact toughness in this study is comparable to the as-built specimens as reported in other studies but lower than machined and HIPed EB-PBF Ti6Al4 [25,34,36]. The as-built specimens had more surface asperities, and more sites of stress concentrations, thus making it less capable of energy absorption as compared to machined specimens. In horizontal specimens, the notch direction showed minimal energy variation. These results confirm that the build orientation is the most influential to the average impact energy absorption. The average value of impact energy for AM specimens is 19.2 J which is comparable to the reported impact energy data (19.33 J) for wrought alloy with α/β annealing [51]. Figure 23 shows the impact toughness of the as – built and machined EB-PBF specimens; as-built and machined LB-PBF specimens and casted Ti6AlV in relation to different build orientation angles. As observed, the impact toughness of EB-PBF Ti6Al4V is comparable to those of LB-PBF and casted alloys [44,52,53]. However, EB-PBF specimens in this study show lower impact toughness than other published data since we examined the as-built surfaces only and no post processing was done. Also, reused powder may lead to lower energy absorption. The as-built surface variation leads to higher local stress concentration which can result in lower energy absorption. In a previous study from our research group [54], U-notch, with its larger root radius, typically exhibits lower stress concentration and higher impact energy

absorption than a sharper V-notch due to reduced crack initiation sensitivity and a larger cross-sectional area subjected to distortion. Although designed as V-notch, the specimens show U-notch curvature at their roots (see Figure 19) resulting from final solidification. In addition to as-built surface effects, this deviation to U-like-notch may lower the impact energy as well.

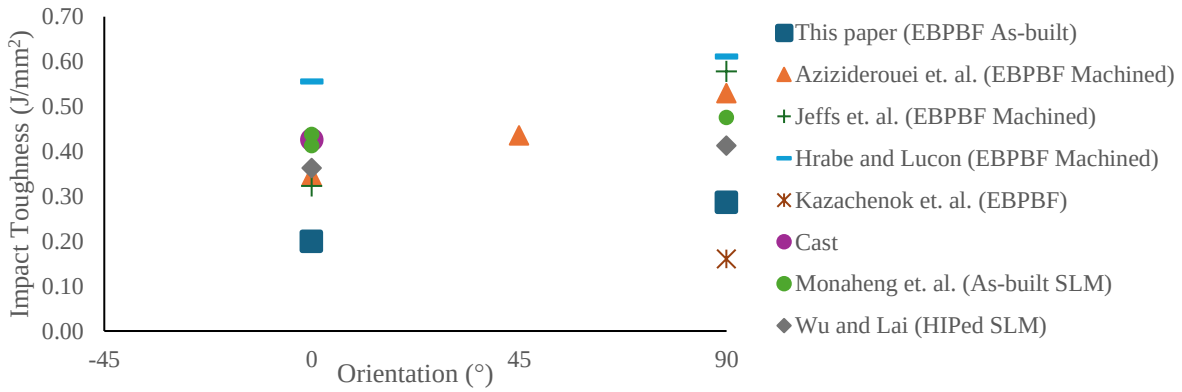

Figure 23. Broad comparison of notch toughness of as built and machined EB-PBF Ti6Al4V with literature [25,32,35,44,52]

Vertical specimens showed greater signs of ductility on the fractured specimens compared to the horizontal specimens. The ruptured surface of the vertical specimens showed ~35% greater shear lips height, and ~51% actual shear area (~40% greater shear lip width and longer continuous shear lips); while the cracking region showed ~15% higher roughness and more rugged topography. Vertical specimens exhibited higher shear angles (44.63°) than horizontal specimens (42.52°). In horizontal specimens, the prior β-grains are split along their build direction. Relatively lower shear angle in horizontal specimens can be perceived as faster crack propagation as the crack is propagated through/along prior-β grains direction. The possibility of crack propagation along the prior β-grains boundary is much higher in horizontal specimen, thereby possibly making the crack propagation comparatively little easier. During the impact loading, the prior β-grains are bent and fractured transversely in vertical specimens (see Figure 21). In the vertical specimens, crack is propagated perpendicular to the columnar grains, where the crack deflection occurs by columnar

β-grains, and goes through more α-β grain boundaries. Thus, impact toughness is enhanced in vertical specimens. The crack deflection enhances energy dissipation by increasing the fracture surface area. Vertical specimens probably allow improved slip transmission between α+β colonies, improving ductility and energy absorption, whereas horizontal specimens exhibit less plasticity because of limited slip across prior β-grain boundaries [39]. Regarding hardness, the average hardness of vertical specimens is 2.12% lower than horizontal specimens due to alteration of prior β grains' direction with respect to loading direction. According to a previous research from our research group [39], the percentage of elongation of vertical and horizontal EB-PBF Ti6Al4V specimens of similar powder cycle are respectively 9.18% and 4.30% (see Table 5), which is also consistent with other literature [34]. Thus, both the tensile properties and hardness may play a synergic role in determining the failure mode and surface characteristics under impact loading.

In a fracture toughness study of EB-PBF Ti6Al4V from our research group, Mojib et. al. reported higher shear area for vertical specimens than horizontal specimens, when the build is attached to the base plate; a similar build condition as in this experiment [12]. Overall, the energy absorption in impact is dissipated as plastic energy through ductile shear and plastic deformation of sheared region; and rest as the surface energy of brittle cracking of fractured region to create new surfaces [55]. The greatest energy absorption occurs in the form of plastic energy in metals.

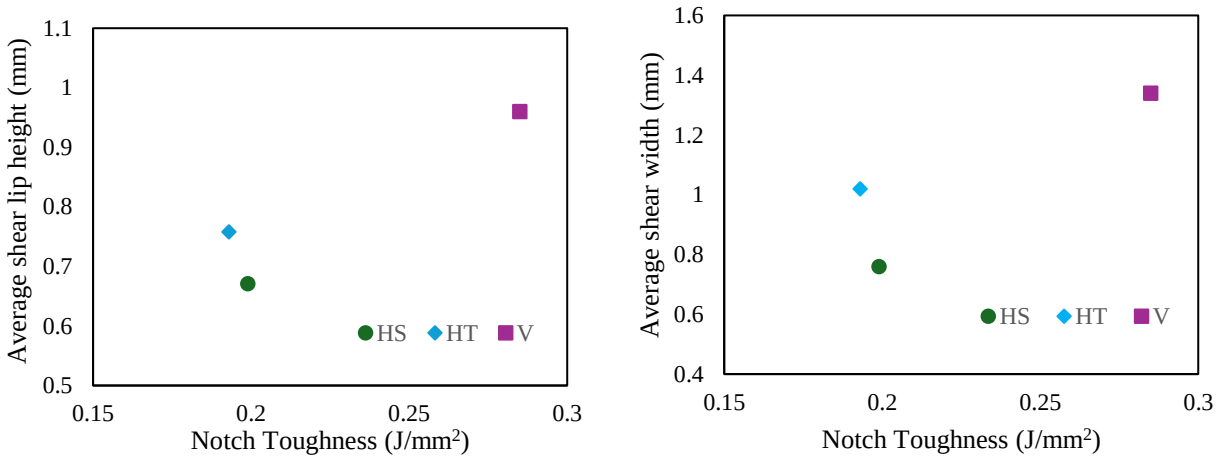

Figure 24. Variation of Notch Toughness with respect to (a) Average shear lip height, (b) Average shear width

Quasi-static plane strain fracture toughness (K_{IC}), and dynamic Charpy impact energy (C_{VN}) are correlated as $\alpha = \left(\frac{K_{IC}}{\sigma_{ys}}\right)^2 \left(\frac{\sigma_{ys}}{C_{VN}}\right)^{\frac{1}{3}}$ when normalized to material's yield strength (σ_{ys}) [38]. In presence of crack, $\frac{K_{IC}}{\sigma_{ys}}$ and $\frac{C_{VN}}{\sigma_{ys}}$ respectively represents the relative significance of crack propagation to plastic deformation in quasi-static loading, and energy absorption to plastic deformation in dynamic fracture. Physically, α is a non-dimensional parameter that compares quasi-static fracture toughness and impact energy absorption. The numeric value of K_{Ic} and C_{VN} are much less than σ_{ys} in Ti-6Al-4V ($\frac{K_{IC}}{\sigma_{ys}} < 1 \; and \; \frac{C_{VN}}{\sigma_{ys}} < 1$) . Therefore, lower value of $\left(\frac{K_{IC}}{\sigma_{ys}}\right)^2$ and higher value of $\left(\frac{C_{VN}}{\sigma_{ys}}\right)^{\frac{1}{3}}$ respectively mean a material's higher possibility to sustain crack-like defects in quasi-static loading, and dynamic loading at high strain rate. Figure 14 (a) represents the plot of $\left(\frac{K_{IC}}{\sigma_{ys}}\right)^2$ and $\left(\frac{C_{VN}}{\sigma_{ys}}\right)^{\frac{1}{3}}$ for EB-PBF as-built specimens for HS, HT, and V orientation according to similar the crack directions of fracture toughness specimens in Vidit [39] and Mojib et al. [9]. EB-PBF specimens are close to wrought and electron beam welded Ti-6Al-4V from Rao

and Acharya's studies [40,41]. In as-built EB-PBF Ti6Al4V specimens, mean α = 1.79, with per-orientation values are 1.99, 1.79 and 1.60 respectively for HT, HS and V specimens; which are close to 1.18 for wrought Ti-6Al-4V reported by Rao and Acharya [40,41]. It is important to note that Rao and Acharya reported the value as 11.85 due to their calculation error in unit conversion. However, the values of α differs from wrought Ti-6Al-4V (1.18) due to difference in fracture toughness and geometry [40,41]. According to Figure 14, $\left(\frac{K_{IC}}{\sigma_{ys}}\right)^2$ values of horizontal and vertical specimens are similar with 3.15% variation, while $\left(\frac{\sigma_{ys}}{C_{VN}}\right)^{\frac{1}{3}}$ shows little wider variation of 4.18%. Another non-dimensional equation comparing quasi-static fracture toughness and notch toughness (K_{NT}) can be expressed as $\beta = \left(\frac{K_{IC}}{\sigma_{ys}}\right)^2 \left(\frac{\sigma_{ys}}{K_{NT}}\right)$ where K_{IC} is in MPa-m$^{0.5}$, K_{NT} is in MPa-m (J/mm^2), and σ_{ys} is in MPa. Figure 14 (b) presents the plot of $\left(\frac{K_{IC}}{\sigma_{ys}}\right)^2$ vs $\left(\frac{K_{\mathrm{NT}}}{\sigma_{ys}}\right)$. $\left(\frac{K_{IC}}{\sigma_{ys}}\right)^2$ shows less variation than $\left(\frac{K_{\mathrm{NT}}}{\sigma_{ys}}\right)$ within horizontal and vertical EB-PBF Ti-6Al-4V. Thus, vertical orientation shows greater resistance to fracture in impact loading than quasi-static loading, which is most probably due to crack arrest by columnar grains discussed earlier. The values of β for HS. HT and V are respectively 24.30, 21.41, and 15.31, which can be utilized to calculate the fracture toughness if the Charpy impact energy absorption is known, a comparatively faster experimental method than fracture toughness test.

The variation of as-built surface roughness is believed to be negligible as the impact is applied against the notch, the crack propagation started from the notch [33]. The minimal and slight variation of energy absorbed in horizontal top face and horizontal side faced specimens could probably be attributed to variation in stress concentration due to microscopic notch radius variation

because of change in solidification behavior with respect to orientation. Overall, the microstructure and the process induced defects, such as porosity affect the energy absorption and fracture propagation [32]. Schur et. al. reported the higher presence of porosity and lack of fusion in vertical specimens compared to horizontal specimens consistently in 30 build cycles [56]. The distribution of the effective pore diameter of EB-PBF Ti6Al4V at similar build cycle is much tighter than virgin power and ranges between 0.05 mm to 0.12 mm [56].

While both microstructure and porosity can influence the energy absorption [57], the microstructure (grain orientation) plays a more dominant role than porosity in this experiment. 80% of the vertical specimens showed higher impact energy absorption (notch toughness) and greater ductility than the horizontal ones, which is probably due to crack deflection in crack propagation perpendicular to the columnar prior-β grains. The remaining 20% vertical specimens showed lower energy absorption, where the interplay of porosity and grain orientation might be responsible, however, would require further research. According to Figure 22, the frequency of pores is higher in vertical specimens than horizontal specimens. Despite the limited porosity approximation based on SEM images, the porosity trend between vertical and horizonal fractured surfaces is consistent with our previous study [12].

3.5 Conclusion

This study evaluated the notch toughness of Electron Beam Powder Bed Fused (EB-PBF) Ti-6Al-4V with respect to build orientation and mechanical properties. According to the findings, the following conclusions are drawn:

- The EB-PBF Ti6Al4V vertical specimens absorbed ~50% higher average impact energy than horizontal specimens, which was attributed to the synergic effects of greater ductility, grain boundary contributions to the crack propagation resistance and lower microhardness.
- The fractured topography of EB-PBF Ti6Al4V can be categorized into shear region and cracking region. The shear region was characterized by shear area, shear lips (height, width, and angle), and shear dips. The surface roughness of the cracking region can be used a metric to quantify and compare the fractured topography. The vertical EB-PBF Ti6Al4V specimens showed ~15% greater roughness than horizontal specimens.
- The fractured surface topography reflects the greater ductility of vertical specimens, i.e., ~35% greater shear lips height, ~51% shear area, ~ 8% greater shear angle in cracking region. The vertical specimens exhibited trans granular fracture, crossing prior β grain boundaries, leading to higher energy absorption, whereas horizontal specimens showed intergranular fracture along prior β boundaries, making them more brittle.
- Process induces defects, i.e., porosity may influence the impact energy absorption as a representative vertical specimen showed greater porosity. Fracture flutes were observed on the ruptured surface.
- Because of their wider shear regions and enhanced crack deflection, vertical specimens have higher ductility and energy absorption, as confirmed by a correlation between shear lip dimensions, and impact energy. The shear lip width and continuous shear length can be used as metrics of greater ductility influencing the impact toughness of PBF Ti-6Al-4V. The impact fracture characteristics correlated well with tensile properties and hardness, where vertical specimens had lower microhardness and higher percentage of elongation, reinforcing the influence of anisotropy on mechanical performance in EB-PBF Ti6Al4V.

References

[1] Kolamroudi, M., Asmael, M., IIkan, M., and Kordani, S., 2021, “Developments on Electron Beam Melting (EBM) of Ti–6Al–4V: A Review,” Trans. Indian Inst. Met., **74**, pp. 783–790.

[2] Chern, A. H., Nandwana, P., Yuan, T., Kirka, M. M., Dehoff, R. R., Liaw, P. K., and Duty, C. E., 2019, “A Review on the Fatigue Behavior of Ti-6Al-4V Fabricated by Electron Beam Melting Additive Manufacturing,” Int. J. Fatigue, **119**, pp. 173–184.

[3] Lewandowski, J. J., and Seifi, M., 2016, “Metal Additive Manufacturing: A Review of Mechanical Properties,” Annu. Rev. Mater. Res., **46**, pp. 151–186.

[4] Tshephe, T., Akinwamide, S., olevsky, E., and Olubambi, P., 2022, “Additive Manufacturing of Titanium-Based Alloys- A Review of Methods, Properties, Challenges, and Prospects,” Heliyon, **8**(3). [Online]. Available: https://doi.org/10.1016/j.heliyon.2022.e09041.

[5] Khanjar, A., and Jasim, N., 2024, “A Brief Review of Electron Beam Melting (EBM) Manufacturing of Ti-6Al-4V Alloy for Biomedical Applications,” J. Manuf. Innov., **1**(1), pp. 83–102.

[6] Schleusener, R., Montelione, A., Cunningham, C., Schur, R., Ramulu, M., and Arola, D., 2025, “On the Contribution of Planned and Unplanned Build Interrupts to the Fatigue Properties of Ti6Al4V from Laser Powder Bed Fusion,” J. Mater. Res. Technol., **35**, pp. 4368–4377.

[7] Abeyta, A., Nouwens, C., Jones, A. M., Haworth, T. A., Montelione, A., Ramulu, M., and Arola, D., 2025, “Characterizing Gas Flow in the Build Chamber of Laser Powder Bed Fusion Systems Utilizing Particle Image Velocimetry: A Path to Improvements.” [Online]. Available: https://doi.org/10.2139/ssrn.5125860.

[8] Soltani-Tehrani, A., Salman Yasin, M., Shao, S., Haghshenas, M., and Shamsaei, N., 2022, “Effects of Powder Particle Size on Fatigue Performance of Laser Powder-Bed Fused Ti-6Al-4V,” Procedia Struct. Integr., **38**, pp. 84–93.

[9] Abdullah, M. B., Mojib, M., Atmadja, N., and Ramulu, M., 2025, “Machinability of Electron Beam Powder Bed Fused Ti-6Al-4V in Face Milling with Coated Carbide End Mill,” J. Mater. Eng. Perform. [Online]. Available: https://doi.org/10.1007/s11665-025-10901-7.

[10] Safdar, A., Wei, L. Y., Snis, A., and Lai, Z., 2012, “Evaluation of Microstructural Development in Electron Beam Melted Ti-6Al-4V,” Mater. Charact., **65**, pp. 8–15.

[11] Ghods, S., Schur, R., Schleusener, R., Montelione, A., Pahuja, R., Wisdom, C., Arola, D., and Ramulu, M., 2022, “Contributions of Intra-Build Design Parameters to Mechanical Properties in Electron Beam Additive Manufacturing of Ti6Al4V,” Mater. Today Commun., **30**. [Online]. Available: https://doi.org/10.1016/j.mtcomm.2022.103190.

[12] Mojib, M. M., Fero, K., Atmadja, N., Arola, D., Chen, X., and Ramulu, M., 2024, “Effect of Intra-Build Design Parameters on the Fracture Toughness Properties of Electron Beam Melted Ti6Al4V,” Fatigue Fract. Eng. Mater. Struct., **47**(10), pp. 3894–3909.

[13] Gong, H., Nadimpalli, V., Rafi, K., Starr, T., and Stucker, B., 2019, “Micro-CT Evaluation of Defects in Ti-6Al-4V Parts Fabricated by Metal Additive Manufacturing,” Technologies, **7**(2), p. 44.

[14] Ran, J., Jiang, F., Sun, X., Chen, Z., Tian, C., and Zhao, H., 2020, “Microstructure and Mechanical Properties of Ti-6Al-4V Fabricated by Electron Beam Melting,” Crystals, **10**(11), p. 972.

[15] Seifi, M., Dahar, M., Aman R, Harrysson, O., Beuth, J., and Lewandowski, J., 2015, “Evaluation of Orientation Dependence of Fracture Toughness and Fatigue Crack Propagation Behavior of As-Deposited ARCAM EBM Ti-6Al-4V,” J. Miner. Met. Mater. Soc., **67**, pp. 597–607.

[16] Sahu, V., Chandrakar, S., Jha, S., and Gurao, N., 2025, “Elucidating the Fracture Toughness of Additively Manufactured and Thermo-Mechanically Treated Ti6Al4V,” Mater. Trans., **65**(5), pp. 532–541.

[17] Ninerola, R., and Giner, E., 2025, “Fracture Toughness of Ti-6Al-4V and Ti-6Al-4V ELI Alloys Fabricated by Electron Beam Melting With Different Orientation and Positions,” Fatigue Fract. Eng. Mater. Struct., **48**(5). [Online]. Available: http://dx.doi.org/10.1111/ffe.14607.

[18] Cain, V., Thijs, L., Humbeeck, J., Hooreweder, B., and Knutsen, R., 2015, “Crack Propagation and Fracture Toughness of Ti6Al4V Alloy Produced by Selective Laser Melting,” Addit. Manuf., **5**, pp. 68–76.

[19] Zhang, H., Dong, D., Su, S., and Chen, A., 2019, “Experimental Study of Effect of Post Processing on Fracture Toughness and Fatigue Crack Growth Performance of Selective Laser Melting Ti-6Al-4V,” Chin. J. Aeronaut., **32**(10), pp. 2382–2393.

[20] Kumar, P., and Ramamurty, U., 2019, “Microstructural Optimization through Heat Treatment for Enhancing the Fracture Toughness and Fatigue Crack Growth Resistance of Selective Laser Melted Ti6Al4V Alloy,” Acta Mater., **169**, pp. 45–59.

[21] Hooreweder, B., Moens, D., Boonen, R., Kruth, J., and Sas, P., 2012, “Analysis of Fracture Toughness and Crack Propagation of Ti6Al4V Produced by Selective Laser Melting,” Adv. Eng. Mater., **14**(1–2), pp. 92–97.

[22] Shrestha, S., Rassi, J., Kannan, M., Morscher, G., Gyekenyesi, A., and Scott-Emuakpor, O., 2021, “Fracture Toughness and Fatigue Crack Growth Rate Properties of AM Repaired Ti–6Al–4V by Direct Energy Deposition,” Mater. Sci. Eng. A, **823**. [Online]. Available: https://doi.org/10.1016/j.msea.2021.141701.

[23] Zhang, X., Martina, F., Ding, J., Wang, X., and Williams, S., 2016, “Fracture Toughness and Fatigue Crack Growth Rate Properties in Wire + Arc Additive Manufactured Ti-6Al-4V,” Fatigue Fract. Eng. Mater. Struct., **40**(5), pp. 790–803.

[24] 2018, “Standard Test Method for Linear-Elastic Plane-Strain Fracture Toughness of Metallic Materials.” [Online]. Available: 10.1520/E0399-22.

[25] Jeffs, S., Lancaster, R., Davies, G., Hole, W., Roberts, B., Stapleton, D., Thomas, M., Todd, I., and Baxter Gavin, 2021, “Effect of Process Parameters and Build Orientation on Microstructure and Impact Energy of Electron Beam Powder Bed Fused Ti-6Al-4V,” Materials, **14**, p. 5376.

[26] Edwards, P., and Ramulu, M, 2015, “Effect of Build Direction on the Fracture Toughness and Fatigue Crack Growth in Selective Laser Melted Ti-6Al-4V,” Fatigue Fract. Eng. Mater. Struct., **38**(10), pp. 1228–1236.

[27] Dzugan, J., Seifi, M., Rzepa, S., Rund, M., Koukolikova, M., Viehrig, H. W., Liu, Z. H., and Lewandowski, J., 2022, “The Effects of Post-Processing on the Local Fracture Toughness Properties of Electron Beam Powder Bed Fusion Ti-6Al-4V Alloy,” Eng. Fract. Mech., **273**. [Online]. Available: https://doi.org/10.1016/j.engfracmech.2022.108697.

[28] Willaims, S., Zhang, H., Leonard, F., Derguti, F., Todd, I., and Prangnell, P., 2015, “XCT Analysis of the Influence of Melt Strategies on Defect Population in Ti–6Al–4V Components Manufactured by Selective Electron Beam Melting,” Mater. Charact., **102**, pp. 47–61.

[29] Jawaid, M., Sultan, M. T. H., and Saba, N., 2018, *Mechanical and Physical Testing of Biocomposites, Fibre-Reinforced Composites and Hybrid Composites*, Woodhead Publishing. [Online]. Available: https://doi.org/10.1016/C2016-0-04437-6.

[30] Solberg, K., and Berto, F., 2019, “Notch-Defect Interaction in Additively Manufactured Inconel 718,” Int. J. Fatigue, **122**, pp. 35–45.

[31] Eylon, D., and Pierce C. M., 1976, “Effect of Microstructure on Notch Fatigue Properties of Ti-6Al-4V,” Metall. Trans. A, **7**, pp. 111–121.

[32] Hrabe, N., White, R., and Lucon, E., 2019, “Effects of Internal Porosity and Crystallographic Texture on Charpy Absorbed Energy of Electron Beam Melting Titanium Alloy (Ti-6Al-4V),” Mater. Sci. Eng., **742**, pp. 269–277.

[33] Lucon, E., and Hrabe, Nikolas, 2018, “Instrumented Impact Testing of Miniaturized Charpy Specimens of AM Ti-6Al-4V,” Mater. Perform. Charact., **7**, pp. 126–138.

[34] Bruno, J., Rochman, A., and Cassar, G., 2017, “Effect of Build Orientation of Electron Beam Melting on Microstructure and Mechanical Properties of Ti-6Al-4V,” J. Mater. Eng. Perform., **26**, pp. 692–703.

[35] Aziziderouei, M., Chen, Z., Pasang, T., Newby, M., and Tao, Y., 2020, “Effect of Lack of Fusion Formed during Electron Beam Powder Bed Fusion of Ti-6Al-4V Alloy on Impact Toughness,” J. Mater. Eng. Perform., **29**, pp. 4978–4990.

[36] Grell, W. A., Solis-Ramos, E., Clark, E., Lucon, E., Garboczi, E. J., Predecki, P. K., Loftus, Z., and Kumosa, M., 2017, “Effect of Powder Oxidation on the Impact Toughness of Electron Beam Melting Ti-6Al-4V,” Addit. Manuf., **17**, pp. 123–134.

[37] Soundarapandiyan, G., Johnston, C., Khan, R. H. U., Leung, C. L. A., Lee, P. D., Hernandez-Nava, E., Chen, B., and Fitzpatrick, M. E., 2021, “The Effects of Powder Reuse on the Mechanical Response of Electron Beam Additively Manufactured Ti6Al4V Parts,” Addit. Manuf., **46**. [Online]. Available: https://doi.org/10.1016/j.addma.2021.102101.

[38] Soundarapandiyan, G., Johnston, C., Chen, B., and Fitzpatrick, M. E., 2021, “Effect of Postprocessing Thermal Treatments on Electron-Beam Powder Bed–Fused Ti6Al4V,” Mater. Des. Process. Commun., **3**(3). [Online]. Available: https://doi.org/10.1002/mdp2.168.

[39] Schur, R., Ghods, S., Schultz, E., Wisdom, C., Pahuja, R., Montelione, A., Arola, D., and Ramulu, M., 2020, “A Fractographic Analysis of Additively Manufactured Ti6Al4V by Electron Beam Melting: Effects of Powder Reuse,” J. Fail. Anal. Prev., **20**, pp. 794–803.

[40] Ghods, S., Schultz, E., Wisdom, C., Schur, R., Pahuja, R., Montelione, A., Arola, D., and Ramulu, M., 2020, “Electron Beam Additive Manufacturing of Ti6Al4V: Evolution of Powder Morphology and Part Microstructure with Powder Reuse,” Materialia, **9**. [Online]. Available: https://doi.org/10.1016/j.mtla.2020.100631.

[41] “Standard Test Methods for Notched Bar Impact Testing of Metallic Materials.” https://doi.org/10.1520/E0023-24.

[42] Abdullah, M. B., and Ramulu, M, 2023, “Sliding Wear Behavior of Electron Beam Melted (EBM) Ti6Al4V,” *ASME 2022 International Mechanical Engineering Congress and Exposition*, Ohio, USA. [Online]. Available: https://doi.org/10.1115/IMECE2022-94735.

[43] Abdullah, M. B., Alajmi, A. F., and Ramulu, M., 2022, “Solid Particle Erosion Behavior of Electron Beam Melted (EBM) Ti6Al4V at Different Built Orientation,” *ASME 2022 International Mechanical Engineering Congress and Exposition*. [Online]. Available: https://doi.org/10.1115/IMECE2021-71776.

[44] Monaheng, L. F., Preez, W. B., and Polese, C., 2021, “Towards Qualification in the Aviation Industry: Impact Toughness of Ti6Al4V(ELI) Specimens Produced through Laser Powder Bed Fusion Followed by Two-Stage Heat Treatment,” Metals, **11**(11), p. 1736.

[45] Hickey, C. F. J., 1961, *Tensile Strength - Hardness Correlation for Titanium Alloys*, WAL TR 405.22/1, WATERTOWN ARSENAL LABS, MA. [Online]. Available: https://apps.dtic.mil/sti/citations/ADA952706.

[46] Abdullah, M. B., Bol, E., Kelley, G., Doyle, C., Schleusener, R., Mojib, M., Chen, X., Arola, D., and Ramulu, M., 2023, “Microstructure and Microhardness of Electron Beam Melted

Ti–6Al–4V Components with Differential Thickness in Initial Deposition Layers," J. Mater. Res. Technol., **26**, pp. 6493–6507.

[47] Tan, X., Kok, Y., Tan, Y. J., Descoins, M., Mangelinck, D., Tor, S. B., Leong, K. F., and Chua, C. kai, 2015, "Graded Microstructure and Mechanical Properties of Additive Manufactured Ti–6Al–4V via Electron Beam Melting," Acta Mater., **97**, pp. 1–16.

[48] Sharma, H., Parfitt, D., Syed, A. K., Wimpenny, D., Baxter, G., and Chen, B., 2019, "A Critical Evaluation of the Microstructural Gradient along the Build Direction in Electron Beam Melted Ti-6Al-4V Alloy," Mater. Sci. Eng., **744**, pp. 182–194.

[49] Borrelli, R., Bellini, C., Berto, F., Cocco, V. D., Foti, P., Lacoviello, F., Mocanu, L. P., Pirozzi, C., Razavi, N., and Franchitti, S., 2024, "The Impact of Ti6Al4V Powder Reuse on the Quality of Electron Beam Powder Bed Fusion Parts," Prog. Addit. Manuf., **9**, pp. 1475–1490.

[50] Meyn, D., and Brooks, E., 1981, "Microstructural Origin of Flutes and Their Use in Distinguishing Striationless Fatigue Cleavage from Stress-Corrosion Cracking in Titanium Alloys," ASTM International, pp. 5–31. https://doi.org/10.1520/STP33421S.

[51] Singh, A. P., Yang, F., Torrens, R., and Gabbitas, B., 2019, "Heat Treatment, Impact Properties, and Fracture Behaviour of Ti-6Al-4V Alloy Produced by Powder Compact Extrusion," Materials, **12**(23), p. 3824.

[52] Wu, M.-W., Lai, P.-H., and Chen, J.-K., 2016, "Anisotropy in the Impact Toughness of Selective Laser Melted Ti–6Al–4V Alloy," Mater. Sci. Eng., **650**, pp. 295–299.

[53] Wu, M.-W., and Lai, P.-H., 2016, "The Positive Effect of Hot Isostatic Pressing on Improving the Anisotropies of Bending and Impact Properties in Selective Laser Melted Ti-6Al-4V Alloy," Mater. Sci. Eng., **658**, pp. 429–438.

[54] Sanders, D. G., Edwards, P., Cantrell, A. M., Gangwar, K., and Ramulu, M., 2015, "Friction Stir-Welded Titanium Alloy Ti-6Al-4V: Microstructure, Mechanical and Fracture Properties," J. Miner. Met. Mater. Soc., **67**, pp. 1054–1063.

[55] Anderson, T. L., 2017, *Elastic–Plastic Fracture Mechanics*.

[56] Schur, R., Ghods, S., Wisdom, C., Pahuja, R., Montelione, A., Arola, D., and Ramulu, M., 2021, "Mechanical Anisotropy and Its Evolution with Powder Reuse in Electron Beam Melting AM of Ti6Al4V," Mater. Des., **200**. [Online]. Available: https://doi.org/10.1016/j.matdes.2021.109450.

[57] Maurya, A., Dabas, A., and Narasimhulu, A., 2019, "A Review on the Effect of Powder Oxidation, Internal Porosity and Crystallographic Texture on the Charpy Impact Energy of Ti-6Al-4V Specimen Fabricated Using Electron Beam Melting and Hot-Isostatic Pressing Post Processing," Int. J. Eng. Res. Technol., **8**(8). https://doi.org/10.17577/IJERTV8IS080024.

Appendix A

A-1 Fracture Toughness failed build pictures

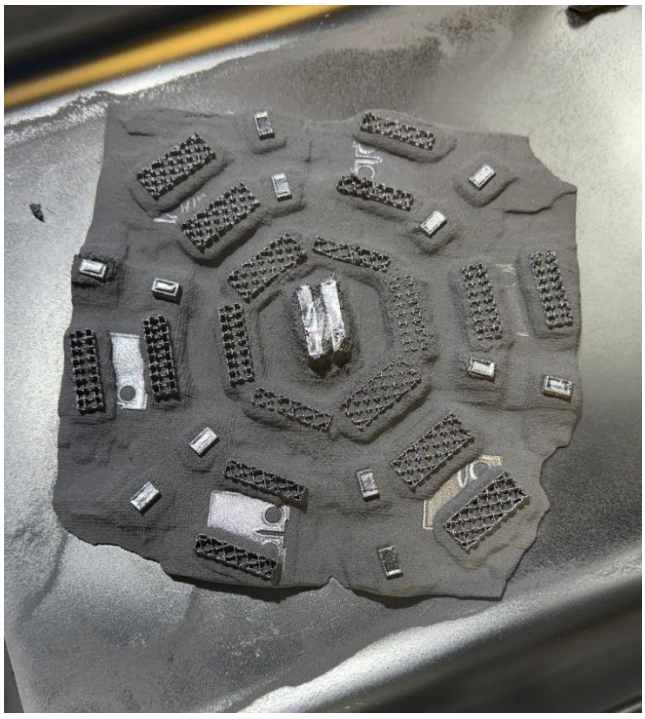

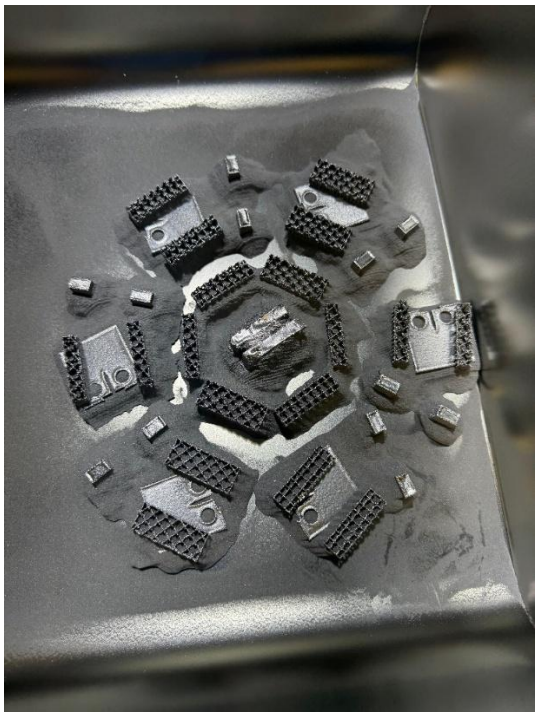

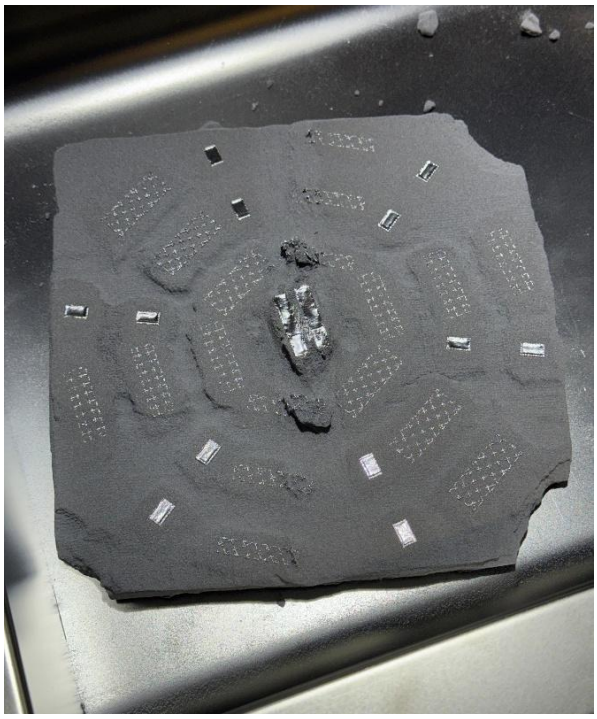

A-2 Fracture Toughness data

Z-X (As built)	a (m)	W (m)	a/w	F(a/W)	Pq (N)	B (m)	Kq (Pa sqrt(m))	Kic (MPa sqrt(m))	Average	Z-X average	Overall average
135*60	0.0125	0.0244	0.512	10.036	8900	0.009	63538107	63.54	**63.54**		
Z-X (Machined)	a	W	a/w	F(a/W)	P	B	K	Kic	Average	**64.785**	
60*140	0.0122	0.0248	0.492	9.424	7950	0.00735	64728666	64.73			
30*155	0.011	0.0247	0.445	8.231	8850	0.0072	64378024	64.38	**65.2**		
100*75	0.0108	0.02458	0.439	8.096	9400	0.0073	66494554	66.49			
Z-Y (As built)	a	W	a/w	F(a/W)	P	B	K	Kic	Average	Z-Y average	
125*100	0.0098	0.0246	0.398	7.248	12700	0.00898	65350597	65.35	**64.48**		
155*170	0.0104	0.02511	0.414	7.559	12000	0.009	63601455	63.6			
Z-Y (machined)	a	W	a/w	F(a/W)	P	B	K	Kic	Average	**66.19**	
75*100	0.0118	0.02452	0.481	9.127	8500	0.008	61928009	61.93			
140*135	0.0089	0.02453	0.363	6.606	11750	0.00755	65644722	65.64	**67.06**		
155*170	0.0094	0.02511	0.374	6.806	12100	0.00745	69761163	69.76			
60*65	0.0082	0.02448	0.335	6.15	13800	0.00765	70907367	70.91			**64.86125**
X-Z (as built)	a	W	a/w	F(a/W)	P	B	K	Kic	Average	X-Z average	
65*155	0.0124	0.025	0.496	9.541	9250	0.00897	62228555	62.23	**62.08**		
135*30	0.0102	0.0247	0.413	7.534	11600	0.00898	61924408	61.92			
										62.75	
X-Z (machined)	a	W	a/w	F(a/W)	P	B	K	Kic	Average		
65*170	0.009	0.025	0.36	6.558	11950	0.00773	64123659	64.12	**64.12**		
Y-Z (as built)	a	W	a/w	F(a/W)	P	B	K	Kic	Average	Y-Z average	
100*155	0.0106	0.02482	0.427	7.827	12100	0.0091	66059486	66.06	**66.06**		
Y-Z (machined)	a	W	a/w	F(a/W)	P	B	K	Kic	Average	**65.72**	
30*65	0.012	0.0249	0.482	9.145	8550	0.00745	66514397	66.51	**65.56**		
15*30	0.0114	0.0245	0.465	8.711	9100	0.00784	64598122	64.6			

A - 3 Fracture Toughness – Surface Roughness data

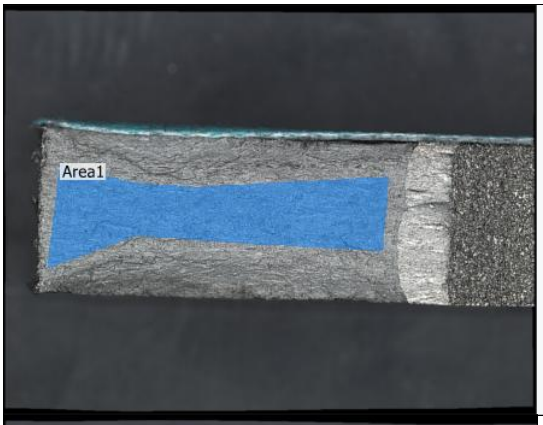

	Sa	Sz	Str	Spc	Sdr	Sq	Ssk
	µm	µm		1/mm		µm	
Max.	25.6804	344.1316		6.1318	0.0808531	34.0917	0.1681
Min.	25.6804	344.1316		6.1318	0.0808531	34.0917	0.1681
Ave.	25.6804	344.1316		6.1318	0.0808531	34.0917	0.1681
Std. DV	0.0000	0.0000		0.0000	0.0000000	0.0000	0.0000
Area1	25.6804	344.1316		6.1318	0.0808531	34.0917	0.1681

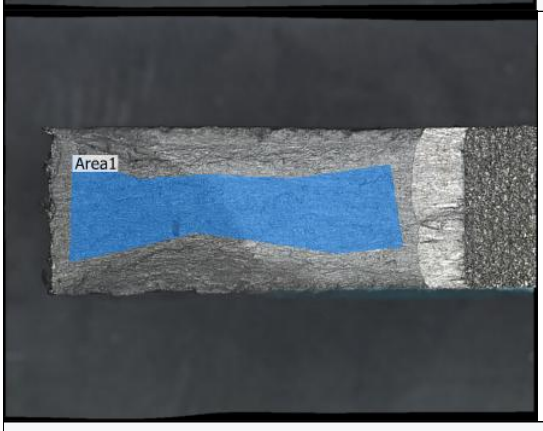

	Sa	Sz	Str	Spc	Sdr	Sq	Ssk
	µm	µm		1/mm		µm	
Max.	25.8533	347.1074		5.9819	0.0785001	33.9603	0.0098
Min.	25.8533	347.1074		5.9819	0.0785001	33.9603	0.0098
Ave.	25.8533	347.1074		5.9819	0.0785001	33.9603	0.0098
Std. DV	0.0000	0.0000		0.0000	0.0000000	0.0000	0.0000
Area1	25.8533	347.1074		5.9819	0.0785001	33.9603	0.0098

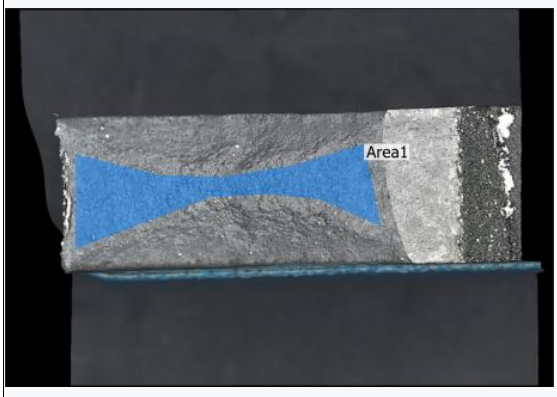

	Sa	Sz	Str	Spc	Sdr	Sq	Ssk
	µm	µm		1/mm		µm	
Max.	29.3767	373.6471		6.7854	0.1011273	38.3909	0.1849
Min.	29.3767	373.6471		6.7854	0.1011273	38.3909	0.1849
Ave.	29.3767	373.6471		6.7854	0.1011273	38.3909	0.1849
Std. DV	0.0000	0.0000		0.0000	0.0000000	0.0000	0.0000
Area1	29.3767	373.6471		6.7854	0.1011273	38.3909	0.1849

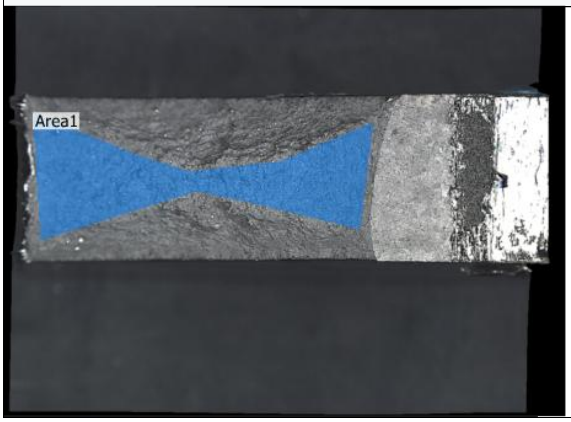

	Sa	Sz	Str	Spc	Sdr	Sq	Ssk
	µm	µm		1/mm		µm	
Max.	29.1351	424.0820		7.0360	0.1009128	38.1929	0.2050
Min.	29.1351	424.0820		7.0360	0.1009128	38.1929	0.2050
Ave.	29.1351	424.0820		7.0360	0.1009128	38.1929	0.2050
Std. DV	0.0000	0.0000		0.0000	0.0000000	0.0000	0.0000
Area1	29.1351	424.0820		7.0360	0.1009128	38.1929	0.2050

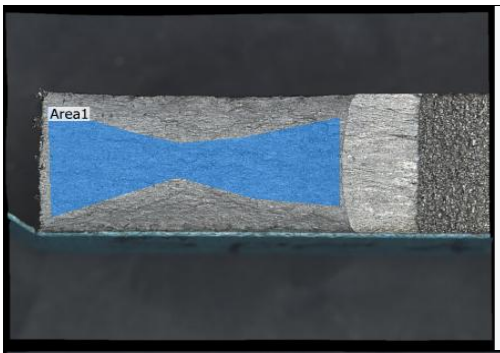

	Sa	Sz	Str	Spc	Sdr	Sq	Ssk
	µm	µm		1/mm		µm	
Max.	24.3210	346.0319		6.0101	0.0732973	32.2579	0.0657
Min.	24.3210	346.0319		6.0101	0.0732973	32.2579	0.0657
Ave.	24.3210	346.0319		6.0101	0.0732973	32.2579	0.0657
Std. DV	0.0000	0.0000		0.0000	0.0000000	0.0000	0.0000
Area1	24.3210	346.0319		6.0101	0.0732973	32.2579	0.0657

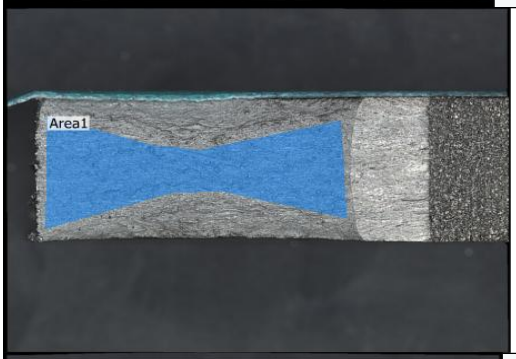

	Sa	Sz	Str	Spc	Sdr	Sq	Ssk
	µm	µm		1/mm		µm	
Max.	24.4026	370.3322		6.1757	0.0743418	32.5095	-0.0245
Min.	24.4026	370.3322		6.1757	0.0743418	32.5095	-0.0245
Ave.	24.4026	370.3322		6.1757	0.0743418	32.5095	-0.0245
Std. DV	0.0000	0.0000		0.0000	0.0000000	0.0000	0.0000
Area1	24.4026	370.3322		6.1757	0.0743418	32.5095	-0.0245

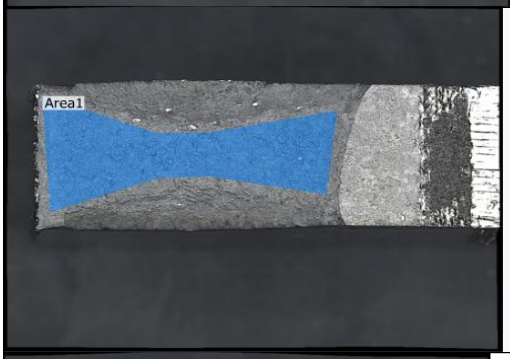

	Sa	Sz	Str	Spc	Sdr	Sq	Ssk
	µm	µm		1/mm		µm	
Max.	25.7423	334.6915		5.7804	0.0774837	34.9146	0.0750
Min.	25.7423	334.6915		5.7804	0.0774837	34.9146	0.0750
Ave.	25.7423	334.6915		5.7804	0.0774837	34.9146	0.0750
Std. DV	0.0000	0.0000		0.0000	0.0000000	0.0000	0.0000
Area1	25.7423	334.6915		5.7804	0.0774837	34.9146	0.0750

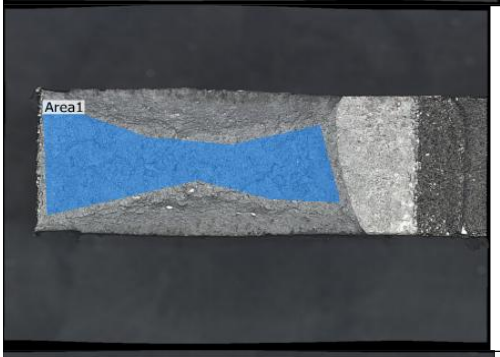

	Sa	Sz	Str	Spc	Sdr	Sq	Ssk
	µm	µm		1/mm		µm	
Max.	26.2797	650.2378		5.4944	0.0784544	37.5032	1.3256
Min.	26.2797	650.2378		5.4944	0.0784544	37.5032	1.3256
Ave.	26.2797	650.2378		5.4944	0.0784544	37.5032	1.3256
Std. DV	0.0000	0.0000		0.0000	0.0000000	0.0000	0.0000
Area1	26.2797	650.2378		5.4944	0.0784544	37.5032	1.3256

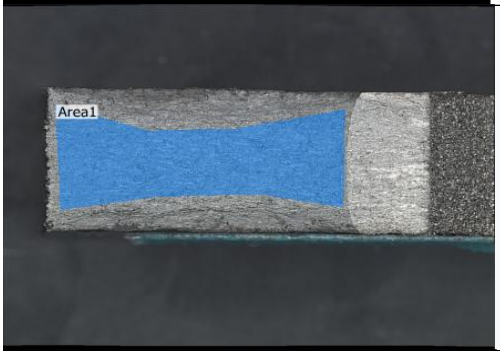

	Sa	Sz	Str	Spc	Sdr	Sq	Ssk
	µm	µm		1/mm		µm	
Max.	22.4684	276.3609		6.3058	0.0680952	29.2728	0.1920
Min.	22.4684	276.3609		6.3058	0.0680952	29.2728	0.1920
Ave.	22.4684	276.3609		6.3058	0.0680952	29.2728	0.1920
Std. DV	0.0000	0.0000		0.0000	0.0000000	0.0000	0.0000
Area1	22.4684	276.3609		6.3058	0.0680952	29.2728	0.1920

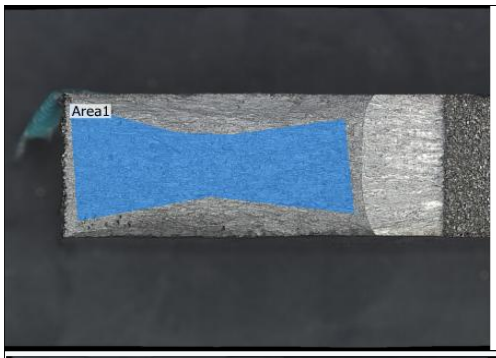

	Sa	Sz	Str	Spc	Sdr	Sq	Ssk
	μm	μm		1/mm		μm	
Max.	22.6093	303.7004		6.0630	0.0676207	29.5817	0.0042
Min.	22.6093	303.7004		6.0630	0.0676207	29.5817	0.0042
Ave.	22.6093	303.7004		6.0630	0.0676207	29.5817	0.0042
Std. DV	0.0000	0.0000		0.0000	0.0000000	0.0000	0.0000
Area1	22.6093	303.7004		6.0630	0.0676207	29.5817	0.0042

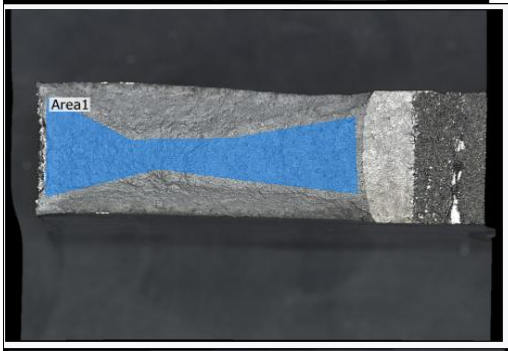

	Sa	Sz	Str	Spc	Sdr	Sq	Ssk
	μm	μm		1/mm		μm	
Max.	25.9847	314.8243		6.1732	0.0787817	33.8897	0.2588
Min.	25.9847	314.8243		6.1732	0.0787817	33.8897	0.2588
Ave.	25.9847	314.8243		6.1732	0.0787817	33.8897	0.2588
Std. DV	0.0000	0.0000		0.0000	0.0000000	0.0000	0.0000
Area1	25.9847	314.8243		6.1732	0.0787817	33.8897	0.2588

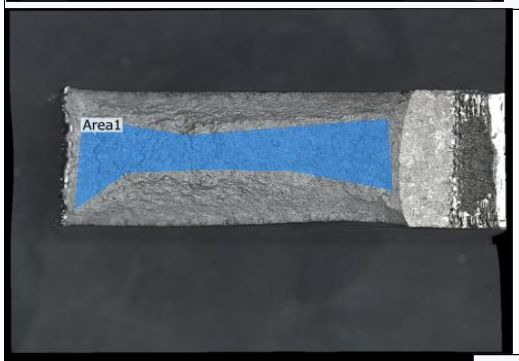

	Sa	Sz	Str	Spc	Sdr	Sq	Ssk
	μm	μm		1/mm		μm	
Max.	24.7946	336.1190		5.8922	0.0744909	32.8014	0.0734
Min.	24.7946	336.1190		5.8922	0.0744909	32.8014	0.0734
Ave.	24.7946	336.1190		5.8922	0.0744909	32.8014	0.0734
Std. DV	0.0000	0.0000		0.0000	0.0000000	0.0000	0.0000
Area1	24.7946	336.1190		5.8922	0.0744909	32.8014	0.0734

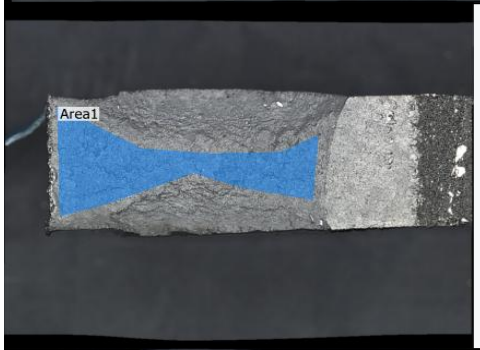

	Sa	Sz	Str	Spc	Sdr	Sq	Ssk
	μm	μm		1/mm		μm	
Max.	26.1370	332.7018		5.9704	0.0788004	34.5908	0.0884
Min.	26.1370	332.7018		5.9704	0.0788004	34.5908	0.0884
Ave.	26.1370	332.7018		5.9704	0.0788004	34.5908	0.0884
Std. DV	0.0000	0.0000		0.0000	0.0000000	0.0000	0.0000
Area1	26.1370	332.7018		5.9704	0.0788004	34.5908	0.0884

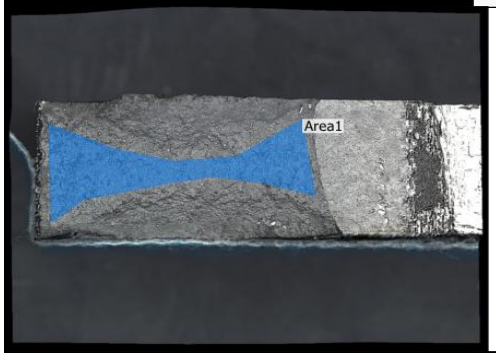

	Sa	Sz	Str	Spc	Sdr	Sq	Ssk
	μm	μm		1/mm		μm	
Max.	27.5885	349.9202		6.6043	0.0875598	36.9330	0.3929
Min.	27.5885	349.9202		6.6043	0.0875598	36.9330	0.3929
Ave.	27.5885	349.9202		6.6043	0.0875598	36.9330	0.3929
Std. DV	0.0000	0.0000		0.0000	0.0000000	0.0000	0.0000
Area1	27.5885	349.9202		6.6043	0.0875598	36.9330	0.3929

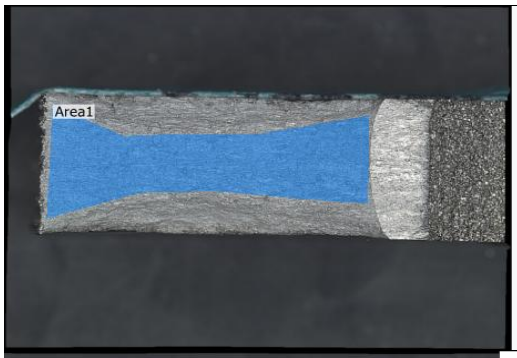

	Sa	Sz	Str	Spc	Sdr	Sq	Ssk
	μm	μm		1/mm		μm	
Max.	20.8820	362.8033		5.3393	0.0614348	28.3584	0.0124
Min.	20.8820	362.8033		5.3393	0.0614348	28.3584	0.0124
Ave.	20.8820	362.8033		5.3393	0.0614348	28.3584	0.0124
Std. DV	0.0000	0.0000		0.0000	0.0000000	0.0000	0.0000
Area1	20.8820	362.8033		5.3393	0.0614348	28.3584	0.0124

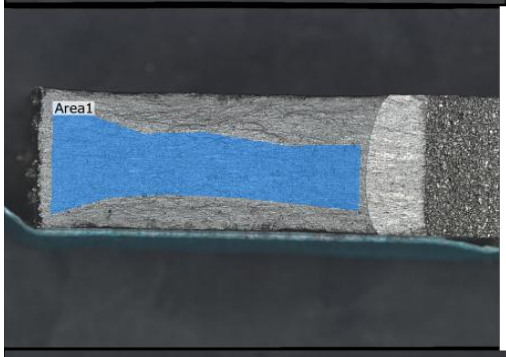

	Sa	Sz	Str	Spc	Sdr	Sq	Ssk
	μm	μm		1/mm		μm	
Max.	20.6290	292.4801		5.9188	0.0601856	27.9995	0.1258
Min.	20.6290	292.4801		5.9188	0.0601856	27.9995	0.1258
Ave.	20.6290	292.4801		5.9188	0.0601856	27.9995	0.1258
Std. DV	0.0000	0.0000		0.0000	0.0000000	0.0000	0.0000
Area1	20.6290	292.4801		5.9188	0.0601856	27.9995	0.1258

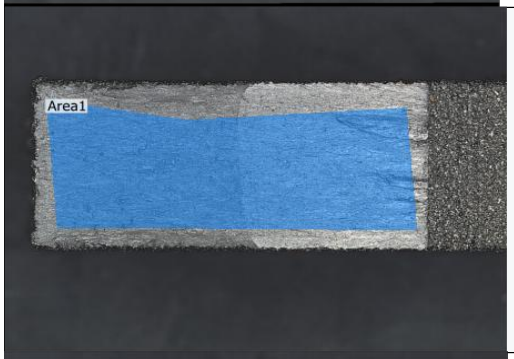

	Sa	Sz	Str	Spc	Sdr	Sq	Ssk
	μm	μm		1/mm		μm	
Max.	16.7323	454.7613		4.6742	0.0455516	25.4461	0.0853
Min.	16.7323	454.7613		4.6742	0.0455516	25.4461	0.0853
Ave.	16.7323	454.7613		4.6742	0.0455516	25.4461	0.0853
Std. DV	0.0000	0.0000		0.0000	0.0000000	0.0000	0.0000
Area1	16.7323	454.7613		4.6742	0.0455516	25.4461	0.0853

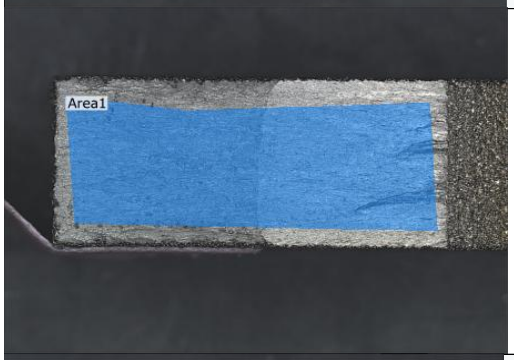

	Sa	Sz	Str	Spc	Sdr	Sq	Ssk
	μm	μm		1/mm		μm	
Max.	15.4210	309.1186		4.1608	0.0335487	21.6785	0.2847
Min.	15.4210	309.1186		4.1608	0.0335487	21.6785	0.2847
Ave.	15.4210	309.1186		4.1608	0.0335487	21.6785	0.2847
Std. DV	0.0000	0.0000		0.0000	0.0000000	0.0000	0.0000
Area1	15.4210	309.1186		4.1608	0.0335487	21.6785	0.2847

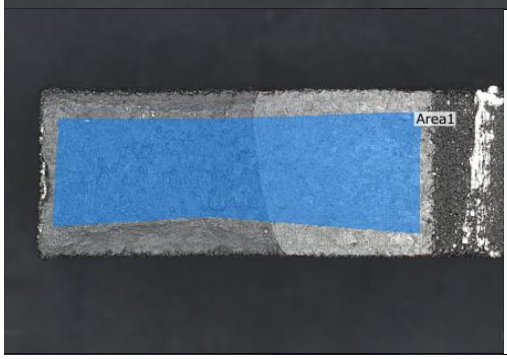

	Sa	Sz	Str	Spc	Sdr	Sq	Ssk
	μm	μm		1/mm		μm	
Max.	17.5836	400.2425		3.5726	0.0511432	28.5169	0.4417
Min.	17.5836	400.2425		3.5726	0.0511432	28.5169	0.4417
Ave.	17.5836	400.2425		3.5726	0.0511432	28.5169	0.4417
Std. DV	0.0000	0.0000		0.0000	0.0000000	0.0000	0.0000
Area1	17.5836	400.2425		3.5726	0.0511432	28.5169	0.4417

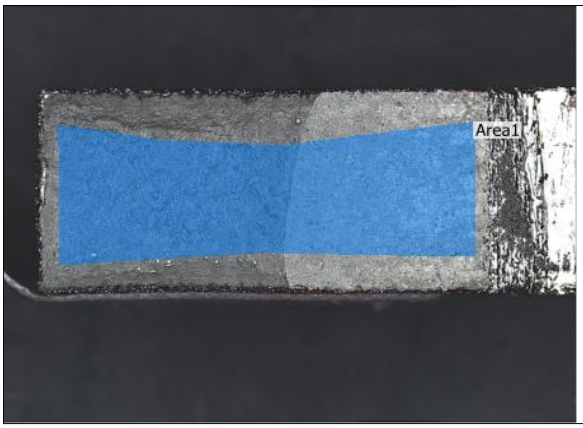

	Sa	Sz	Str	Spc	Sdr	Sq	Ssk
	µm	µm		1/mm		µm	
Max.	17.7337	379.2913		4.0088	0.0531802	28.6740	-0.143
Min.	17.7337	379.2913		4.0088	0.0531802	28.6740	-0.143
Ave.	17.7337	379.2913		4.0088	0.0531802	28.6740	-0.143
Std. DV	0.0000	0.0000		0.0000	0.0000000	0.0000	0.000
Area1	17.7337	379.2913		4.0088	0.0531802	28.6740	-0.143

A - 4 Fracture Toughness – Shear lip height

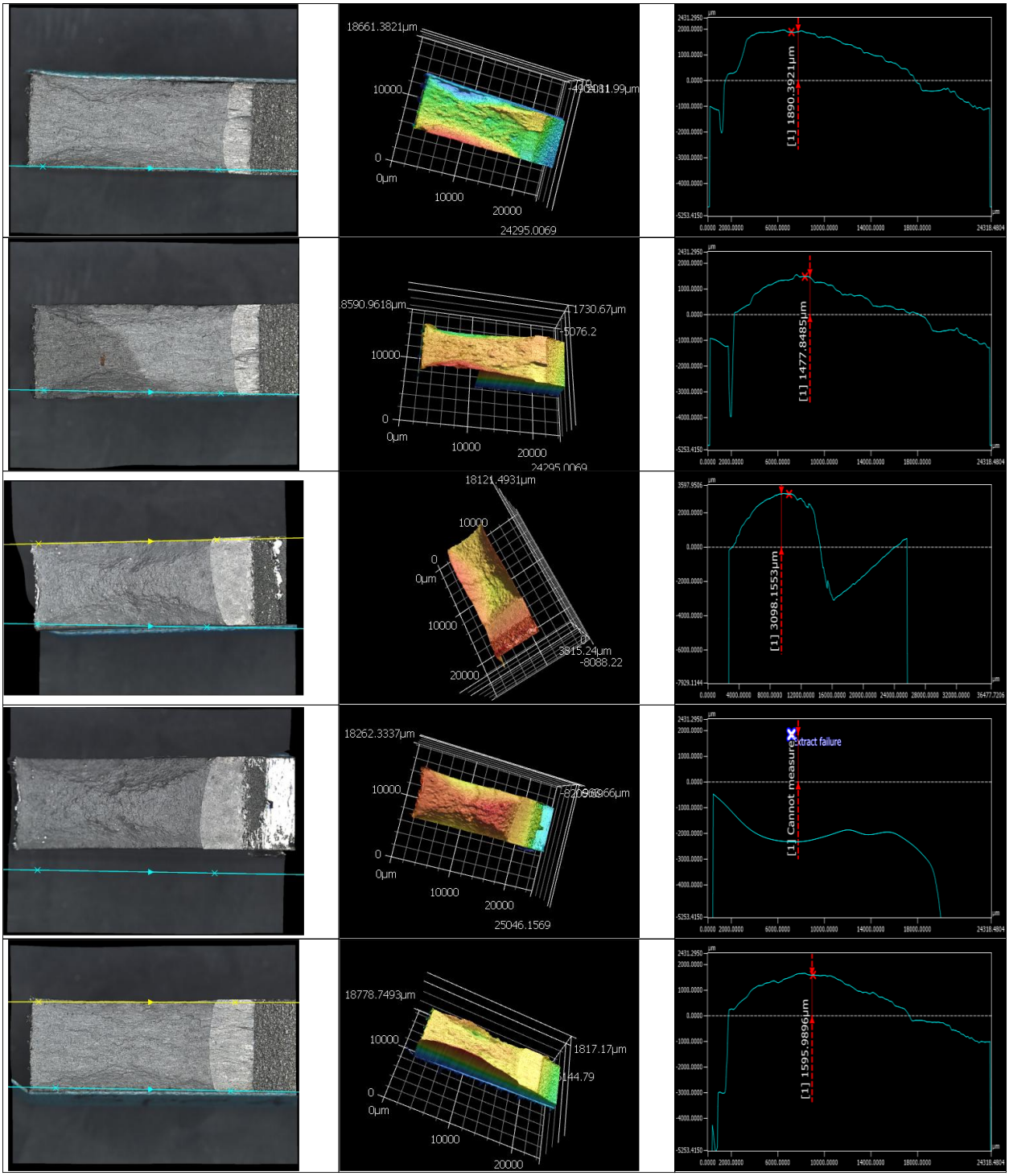

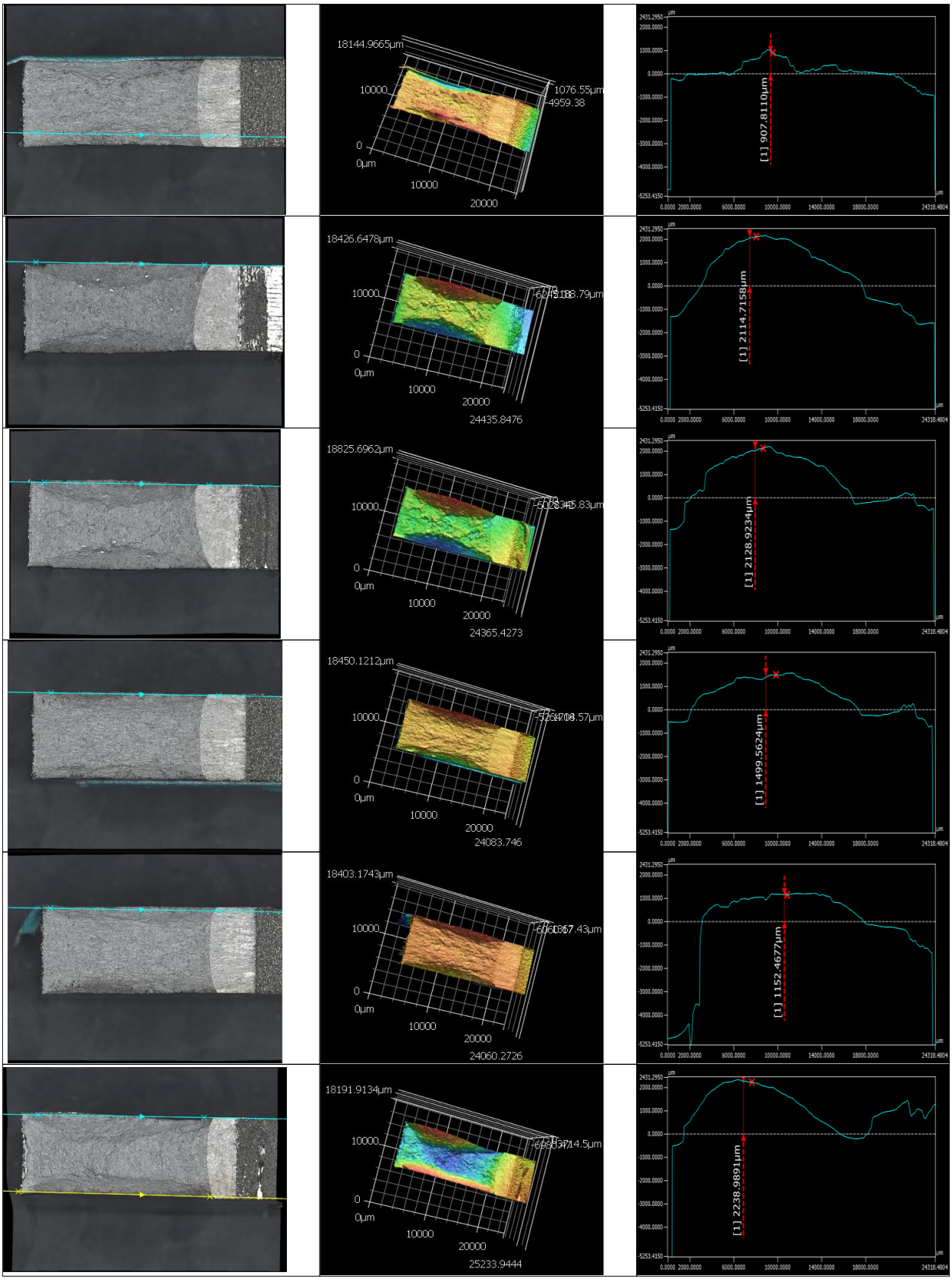
18144.9665µm
10000
0
0µm
10000
20000
1076.55µm
-4959.38
[1] 907.8110µm
18426.6478µm
10000
0
0µm
10000
20000
24435.8476
[1] 2114.7158µm
18825.6962µm
10000
0
0µm
10000
20000
24365.4273
[1] 2128.9234µm
18450.1212µm
10000
0
0µm
10000
20000
24083.746
[1] 1499.5624µm
18403.1743µm
10000
0
0µm
10000
20000
24060.2726
[1] 1152.4677µm
18191.9134µm
10000
0
0µm
10000
20000
25233.9444
[1] 2238.9891µm

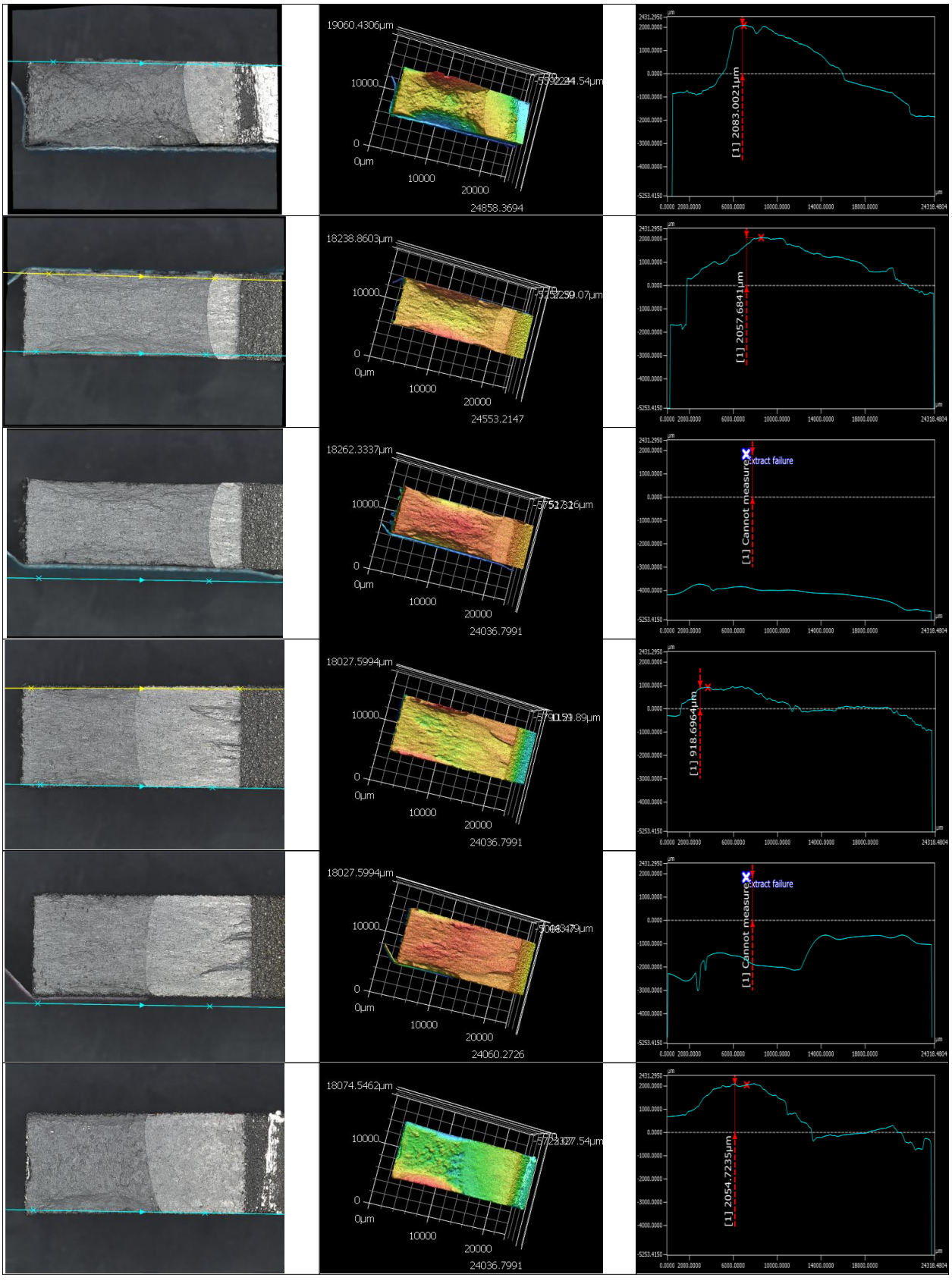
19060.4306µm
10000
0
0µm
10000
20000
24858.3694
[1] 2083.0021µm
18238.8603µm
10000
0
0µm
10000
20000
24553.2147
[1] 2057.6841µm
18262.3337µm
10000
0
0µm
10000
20000
24036.7991
Extract failure
[1] Cannot measure
18027.5994µm
10000
0
0µm
10000
20000
24036.7991
[1] 918.6964µm
18027.5994µm
10000
0
0µm
10000
20000
24060.2726
Extract failure
[1] Cannot measure
18074.5462µm
10000
0
0µm
10000
20000
24036.7991
[1] 2054.7235µm

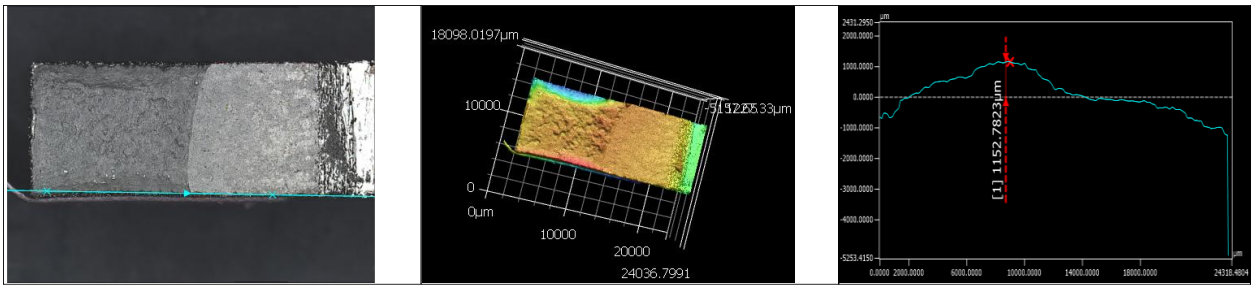
18098.0197µm
10000
0
0µm
10000
20000
24036.7991
[1] 1152.7823µm
2431.2950
2000.0000
1000.0000
0.0000
-1000.0000
-2000.0000
-3000.0000
-4000.0000
-5253.4150
0.0000
2000.0000
6000.0000
10000.0000
14000.0000
18000.0000
24318.4804

A-5 Fracture Toughness – Shear angle

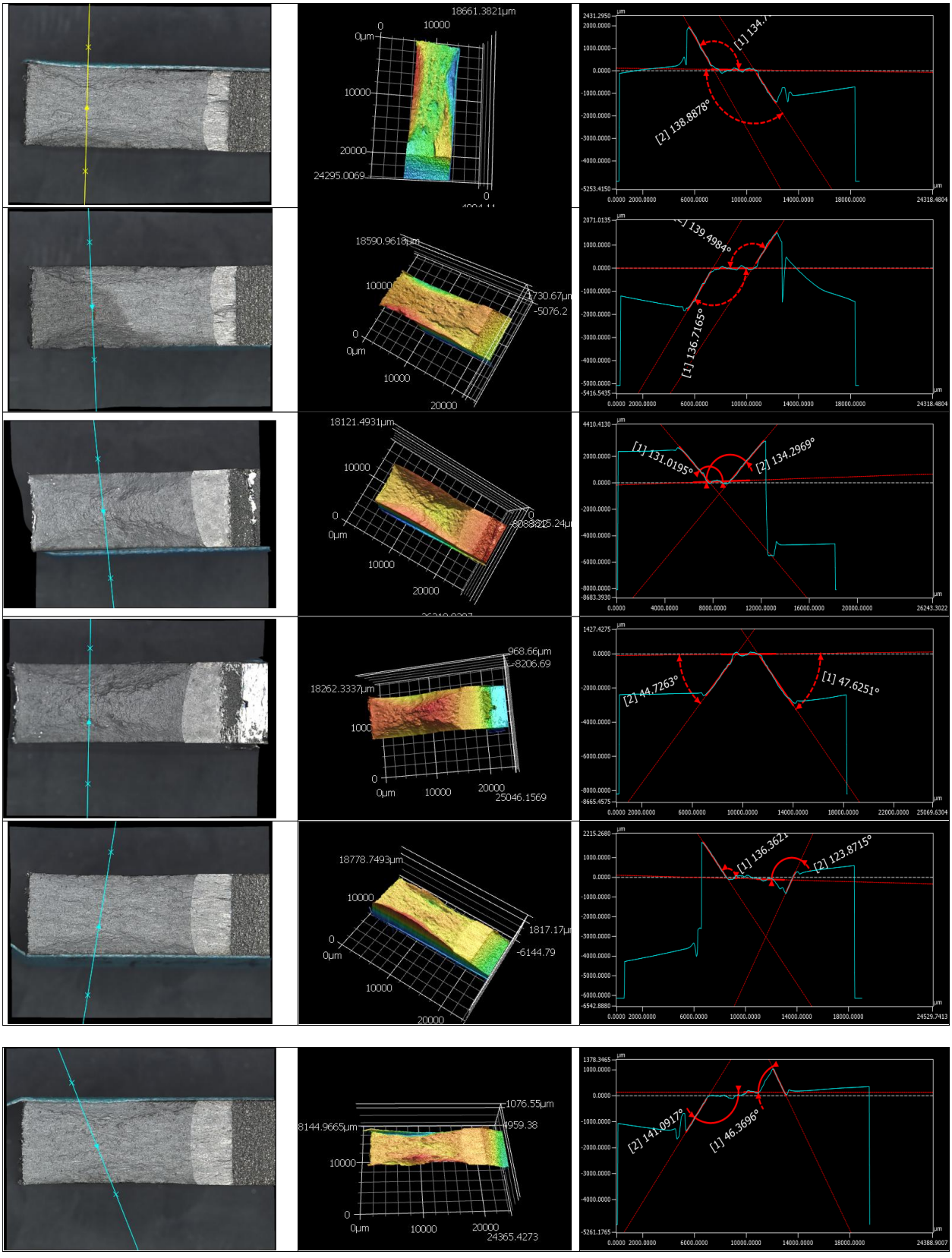

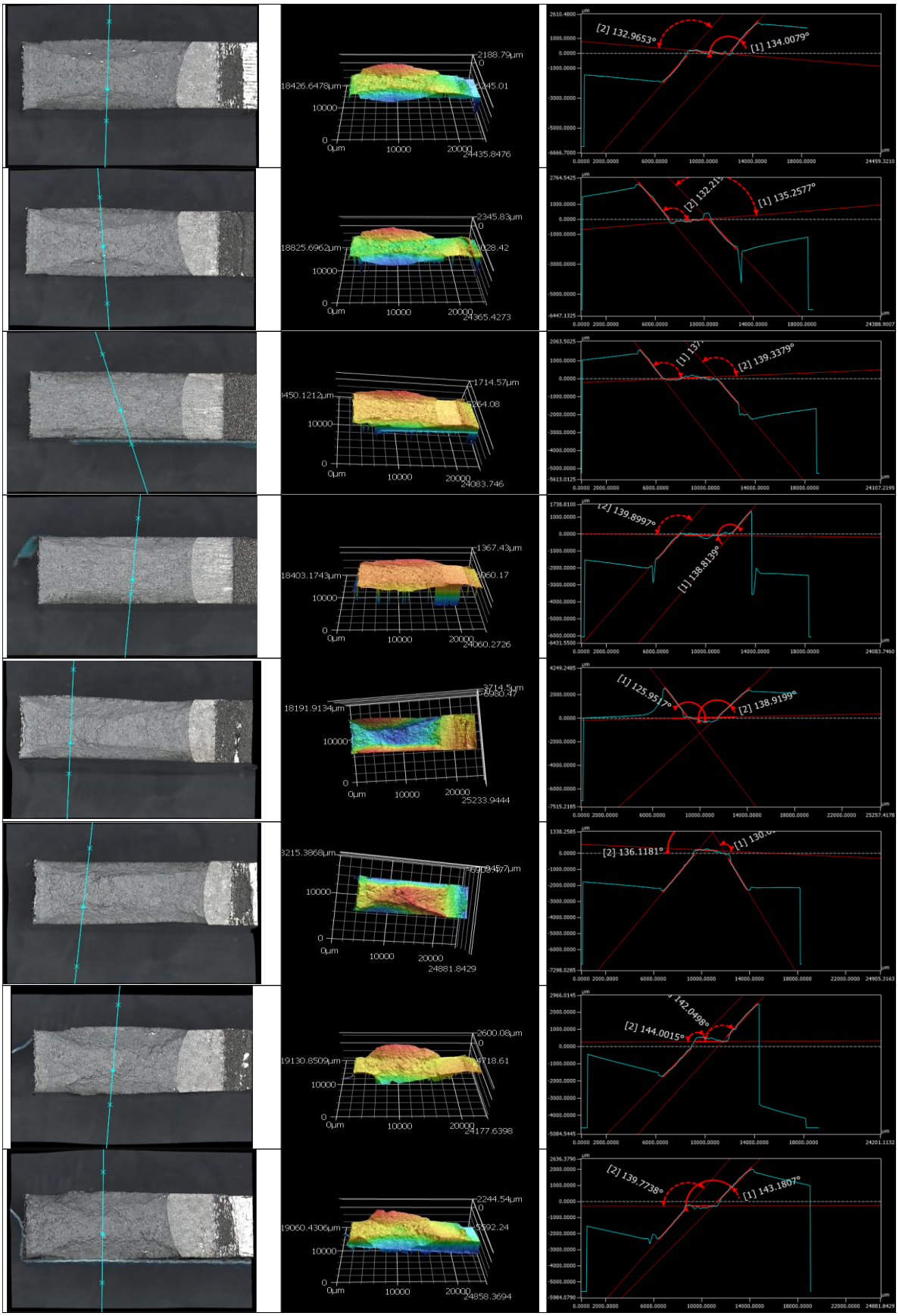
[2] 132.9653°
[1] 134.0079°
[2] 132.21°
[1] 135.2577°
[1] 137
[2] 139.3379°
[2] 139.8997°
[1] 138.8139°
[1] 125.9517°
[2] 138.9199°
[2] 136.1181°
[1] 130.
[2] 142.0498°
[2] 144.0015°
[2] 139.7738°
[1] 143.1807°

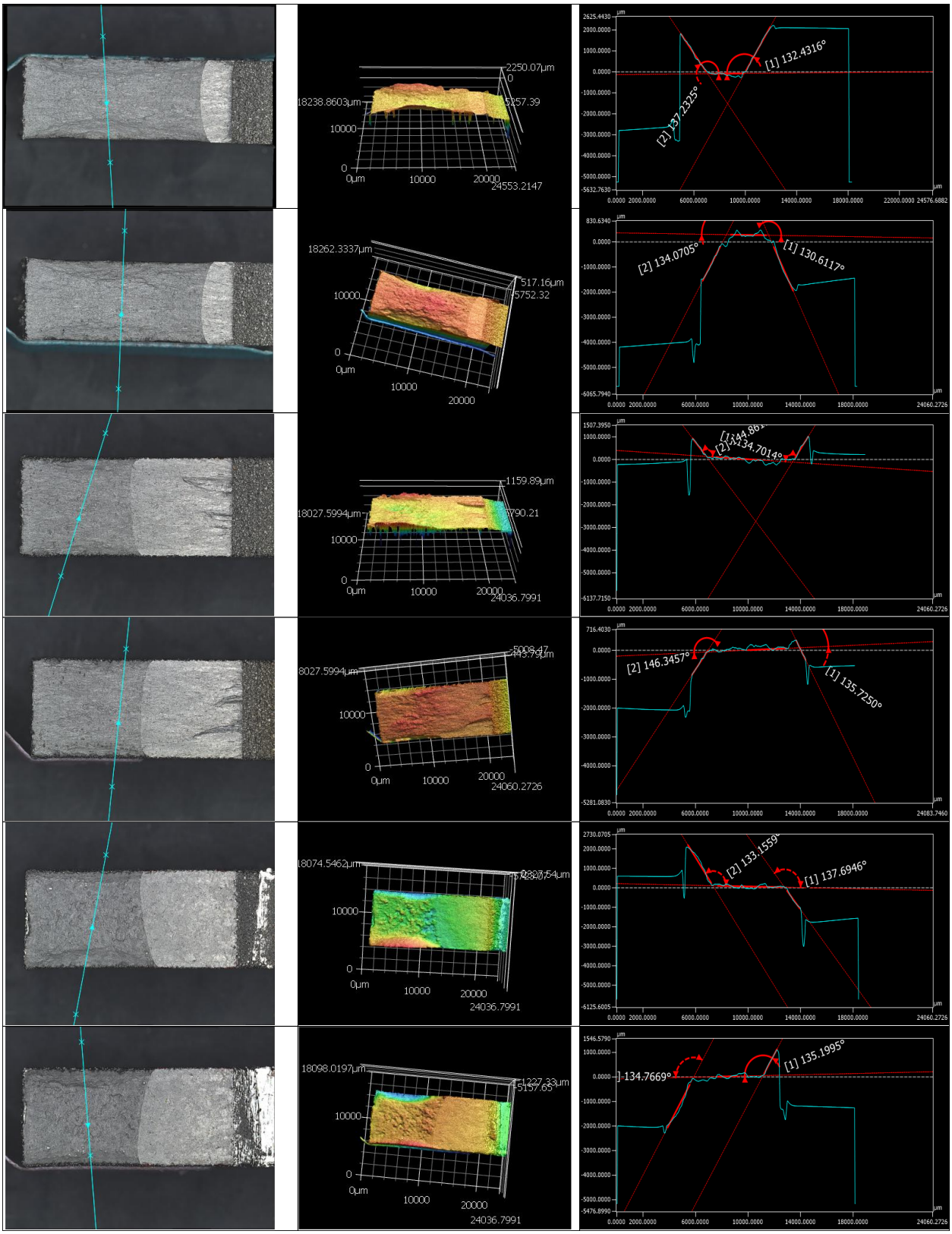
2250.07µm
0
18238.8603µm
5257.39
10000
0
0µm
10000
20000
24553.2147
[1] 132.4316°
[2] 137.2325°
18262.3337µm
517.16µm
5752.32
[2] 134.0705°
[1] 130.6117°
1159.89µm
18027.5994µm
10000
0µm
24036.7991
[2] 134.7014°
8027.5994µm
10000
0µm
10000
20000
24060.2726
[2] 146.3457°
[1] 135.7250°
18074.5462µm
10000
0µm
10000
20000
24036.7991
[2] 133.1559°
[1] 137.6946°
18098.0197µm
10000
0µm
10000
20000
24036.7991
-134.7669°
[1] 135.1995°

Appendix B

B-1 Impact Energy data

Sample#	Energy (J)
HS1	15.67
	(failed)
HS3	16
HS4	15.5
HS5	16.25
HS6	15
HS7	15.25
HS8	16
HS9	16
HS10	17.75
Average	15.9355556
StDev	0.79128236

Sample#	Energy (J)
HT1	16.5
HT2	15
HT3	17
HT4	16
HT5	16.25
HT6	15
HT7	14
HT8	14.5
HT9	14
HT10	16.5
Average	15.475
StDev	1.10836466

Sample#	Energy (J)
V1	16
V2	18.25
V3	20.33
V4	54.5
V5	16
V6	50.25
V7	10.5
V8	9.75
V9	16
V10	17
Average	22.858
StDev	15.9133583

B-2 Notch Toughness - Surface Roughness data

	Sa (µm)	Sz (µm)	Sq (µm)	Sp (µm)	Sv (µm)	Ssk (µm)	Sku (µm)
HS1-1	16.9715	237.0165	22.1532	115.5533	121.4632	-0.1125	4.1466
HS1-2	17.0026	234.7481	22.3055	140.1997	94.5485	0.3527	4.3836
HS2-1	18.6424	319.4124	24.7718	147.9278	171.4846	0.2246	4.8603
HS2-2	18.6093	320.6808	24.7236	148.5247	172.1561	0.2086	4.847
HS3-1	18.1113	250.6239	24.0057	135.7978	114.826	0.3721	4.2727
HS3-2	18.273	258.0279	24.1625	132.2189	125.809	-0.0745	4.2286
HS4-1	17.7105	245.6142	23.5327	146.9135	98.7007	0.197	4.2215
HS4-2	17.5278	220.3142	23.3754	118.8656	101.4485	0.1549	4.243
HS5-1	17.7915	268.8564	24.1607	152.6434	116.213	0.1361	4.8947
HS5-2	17.8034	287.7358	24.2203	138.8399	148.8959	0.3026	5.0431
HS6-1	19.2479	250.3177	25.6322	111.8062	138.5115	0.0552	4.4716
HS6-2	19.1853	262.0427	25.523	150.347	111.6957	0.157	4.59
HS7-1	19.2031	279.0854	25.6861	151.2605	127.8248	0.3569	4.7137
HS7-2	18.9378	287.1423	25.3229	170.0311	117.1113	0.1168	4.6897
HS8-1	17.6272	248.4011	23.486	128.2741	120.127	0.1247	4.444
HS8-2	17.8982	258.9942	23.9383	142.3032	116.691	0.1603	4.6574
HS9-1	17.293	218.0662	22.7786	120.6221	97.4442	0.0495	4.1673
HS9-2	17.4628	228.579	22.9463	109.7555	118.8235	0.2009	4.1423
HS10-1	19.4903	308.192	26.5562	182.4704	125.7216	0.2962	5.2566
HS10-2	18.8522	292.4868	25.6618	148.8492	143.6376	0.0346	5.121
Average	**18.18206**	**263.8169**	**24.24714**	**139.6602**	**124.1567**	**0.165685**	**4.569735**
StDev	0.788857	31.0059	1.227566	18.79313	21.73613	0.133887	0.349908

Sample and face#	Sa (µm)	Sz (µm)	Sq (µm)	Sp (µm)	Sv (µm)	Ssk (µm)	Sku (µm)
HT1-1	21.4423	450.9931	31.688	218.8626	232.1304	0.384	9.1591
HT1-2	21.3739	726.7782	32.8339	404.0481	322.7301	-0.2648	14.5463
HT2-1	18.0444	266.7647	24.1154	140.2693	126.4954	0.1508	4.2319
HT2-2	17.9282	317.6543	24.1868	195.5066	122.1477	0.2848	5.1139
HT3-1	20.6942	717.975	30.1282	431.8822	286.0928	0.0994	12.882
HT3-2	20.8923	546.5944	29.6654	250.8967	295.6977	0.0269	9.9713
HT4-1	17.631	276.8812	22.9825	124.7438	152.1374	0.2315	4.1499
HT4-2	17.2683	215.7187	22.3874	110.1299	105.5888	-0.0149	3.8054
HT5-1	18.0179	427.1822	24.9415	169.1292	258.053	0.0051	6.7814
HT6-1	19.3881	359.5553	25.8898	155.6283	203.927	0.1371	4.6252
HT6-2	20.0697	344.2077	26.8981	197.4517	146.756	0.3178	4.8437
HT7-1	18.153	290.5328	24.1042	140.5988	149.9341	0.275	4.8127
HT7-2	17.6197	271.0837	23.3453	148.9829	122.1008	0.2118	4.7452
HT8-1	18.4671	438.4544	24.8782	277.4478	161.0066	0.2038	7.5941
HT8-2	19.0446	352.9941	25.3333	197.0482	155.9459	0.4083	5.0692
HT9-1	18.0836	250.72	23.5395	148.6338	102.0862	0.2276	3.9256
HT9-2	18.0455	243.6775	23.576	150.395	93.2825	0.1718	4.0836
HT10-1	20.6615	284.7846	27.8181	156.8278	127.9568	0.4069	4.4614
HT10-2	20.5396	358.4888	27.371	188.1721	170.3167	-0.0763	4.2337
Average	**19.12447**	**375.8442**	**26.08856**	**200.3503**	**175.494**	**0.167716**	**6.265032**
StDev	1.428707	147.9571	3.071173	87.51075	70.40621	0.175223	3.168074

Sample and face#	Sa (μm)	Sz (μm)	Sq (μm)	Sp (μm)	Sv (μm)	Ssk (μm)	Sku (μm)
V1-1	23.1892	323.8319	30.776	194.5452	129.2867	0.4422	4.7354
V1-2	22.9844	335.6884	30.5331	148.2499	187.4386	-0.0743	4.4827
V2-1	20.5267	359.1953	27.8723	151.9114	207.2839	0.2731	5.3897
V2-2	20.6612	458.6132	28.4381	275.4027	183.2105	0.1901	6.7075
V3-1	20.7617	362.4329	27.6259	158.6798	203.7531	-0.1311	4.8767
V3-2	20.6161	298.092	27.4925	167.3412	130.7508	0.4132	4.814
V4-1	21.336	321.7072	29.0193	186.8145	134.8927	0.6291	5.6793
V4-2	20.9832	288.4377	27.5879	119.4406	168.9971	-0.0627	4.2393
V5-1	22.5027	360.7139	30.1396	208.3175	152.3964	0.1787	4.8054
V5-2	21.9661	332.1572	29.1714	155.8675	176.2897	0.1396	4.3575
V6-1	22.6287	301.5871	29.8248	156.5761	145.011	-0.077	4.2798
V6-2	22.7045	333.4968	30.2975	181.9551	151.5418	0.4507	4.851
V7-1	17.8687	307.058	24.2718	162.0375	145.0204	-0.0063	5.3243
V7-2	18.0689	297.8658	24.6317	162.9228	134.943	0.4611	5.6098
V8-1	18.7994	305.2262	25.7168	155.0288	150.1974	0.0474	5.2021
V8-2	18.6658	286.4032	25.7417	168.7759	117.6273	0.4923	5.5681
V9-1	21.162	291.924	27.9971	150.38	141.544	0.0191	4.1698
V9-2	21.2106	270.8676	28.0107	154.4936	116.374	0.2496	4.1528
V10-1	26.3097	510.3844	35.7198	243.3859	266.9985	0.084	5.97
V10-2	25.3204	589.6236	35.179	349.0257	240.5979	0.2289	7.095
Average	**21.4133**	**346.7653**	**28.80235**	**182.5576**	**164.2077**	**0.197385**	**5.11551**
StDev	2.180494	81.57627	2.940746	52.67781	40.49006	0.224786	0.820692

B-3 Notch Toughness - Maximum Continuous Shear Lip length

Horizontal Side			
	Lip height (μm)	Dip height (μm)	**AVG (μm)**
HS1	5430.21	5307.94	5369.08
HS2	2871.78		2871.78
HS3	3785.01	3891.97	3838.49
HS4	6594.36	6216.05	6405.21
HS5	5660.04	5539.06	5599.55
HS6	6791.49	6618.99	6705.24
HS7	4620.22	4679.02	4649.62
HS8	6573.53	6408.59	6491.06
HS9	5413.53	5005.76	5209.65
HS10	6380.89	6007.77	6194.33
AVG	**5412.11**	**5519.46**	**5465.78**
Std dev	**1240.06**	**842.44**	**1181.58**

Horizontal Top			
	Lip height (µm)	Dip height (µm)	**AVG (µm)**
HT1	6978.65	6387.88	6683.27
HT2	6556.07	7197.75	6876.91
HT3	6963.88	6532.10	6747.99
HT4		6920.42	6920.42
HT5		6653.12	6653.12
HT6	6775.61	6539.97	6657.79
HT7	5210.04	7002.04	6106.04
HT8	3368.31	3845.32	3606.82
HT9	7477.27	6629.95	7053.61
HT10	7251.21	7359.59	7305.40
AVG	**6322.63**	**6506.81**	**6414.72**
Std dev	**1287.56**	**935.79**	**996.39**

Vertical			
	Lip height (µm)	Dip height (µm)	**AVG (µm)**
V1	7790.47	7367.04	7578.76
V2	7347.76	7192.60	7270.18
V3	7863.54	7485.66	7674.60
V4	7339.23	7303.16	7321.20
V5	5296.41	6387.71	5842.06
V6	7771.15	7285.93	7528.54
V7	6727.36	6484.15	6605.76
V8	5760.43	5715.56	5738.00
V9	7712.16	7463.83	7588.00
V10	7064.73	7147.60	7106.17
AVG	**7067.32**	**6983.32**	**7025.32**
Std dev	**847.37**	**557.34**	**684.48**

B-4 Notch Toughness - Shear angle

Horizontal Top					
	angle 1	angle 2	AVG		Average for each
HT1	131.17	131.73	131.45	HT1	131.45
HT2	130.39	135.35	132.87	HT2	132.87
HT3-1	143.78		143.78	HT3	138.61
HT3-2	133.44		133.44	HT4	135.35
HT4	133.94	136.76	135.35	HT5	
HT6-1	137.50	143.25	140.38	HT6	142.95
HT6-2	145.53		145.53	HT7	135.70
HT7-1	132.82		132.82	HT8	140.54
HT7-2	138.58		138.58	HT9	140.54
HT8-1	143.63		143.63	HT10	143.80
HT8-2	137.44		137.44	**Total aveg**	**137.98**
HT9-1	143.06		143.06	**std dev**	**4.12**
HT9-2	138.02		138.02		
HT10-1	140.99	134.59	137.79		
HT10-2	149.81		149.81		

Vertical					
	angle 1	angle 2	AVG		Average for each
V1	140.88	133.46	137.17	V1	137.17
V2	149.67	138.96	144.32	V2	144.32
V3	137.20	137.65	137.43	V3	137.43
V4	137.57		137.57	V4	137.57
V5-1	134.80		134.80	V5	127.22
V5-2	119.64		119.64	V6	136.53
V6-1	139.23		139.23	V7	133.34
V6-2	133.83		133.83	V8	127.85
V7-1	131.90		131.90	V9	135.69
V7-2	134.78		134.78	V10	136.62
V8	127.85		127.85	**Total aveg**	**135.37**
V9-1	131.63		131.63	**std dev**	**4.72**
V9-2	139.75		139.75		
V10	137.63	135.60	136.62		

Horizontal Side					
	angle 1	angle 2	AVG		Average for each
HS1	152.38	151.99	152.19	HS1	152.19
HS2-1	138.07	131.11	134.59	HS2	136.31
HS2-2	139.35	136.69	138.02	HS3	137.53
HS3-1	137.22	143.62	140.42	HS4	130.86
HS3-2	132.24	137.03	134.64	HS5	116.09
HS4-1	131.65		131.65	HS6	134.10
HS4-2	130.07		130.07	HS7	138.52
HS5	116.09		116.09	HS8	146.31
HS6	124.30	143.89	134.10	HS9	140.04
HS7-1	149.89	129.42	139.66	HS10	132.91
HS7-2	139.21	135.56	137.39	**Total aveg**	**136.48**
HS8-1	143.29		143.29	**std dev**	**9.09**
HS8-2	149.32		149.32		
HS9	137.92	142.16	140.04		
HS10-1	129.06		129.06		
HS10-2	136.75		136.75		

B-5 Notch Toughness - Shear Area

Horizontal Side			
Specimen No.	Up face area (mm2)	(mm2)	**Average (mm2)**
HS1	7.59	6.00	6.79
HS2	8.13	8.13	8.13
HS3	6.72	7.76	7.24
HS4	8.78	7.55	8.16
HS5	7.47	6.55	7.01
HS6	8.36	5.89	7.12
HS7	6.29	6.42	6.36
HS8	8.20	7.13	7.66
HS9	9.64	6.61	8.12
HS10	9.94	8.78	9.36
Average	**8.11**	**7.08**	**7.60**
Std dev	**1.102**	**0.905**	**0.829**

Horizontal Top			
Specimen No.	Up face area (mm2)	(mm2)	**Average (mm2)**
HT1	11.93	6.97	9.45
HT2	13.84	10.92	12.38
HT3	9.12	8.46	8.79
HT4	11.48	10.93	11.21
HT5	8.42	8.42	8.42
HT6	9.51	8.66	9.09
HT7	10.32	8.73	9.53
HT8	10.13	10.46	10.29
HT9	10.82	11.87	11.35
HT10	13.10	10.64	11.87
Average	**10.87**	**9.61**	**10.24**
Std dev	**1.643**	**1.475**	**1.313**

Vertical			
Specimen No.	Up face area (mm2)	(mm2)	**Average (mm2)**
V1	14.54	10.78	12.66
V2	14.50	10.77	12.63
V3	17.39	10.89	14.14
V4	18.01	13.71	15.86
V5	14.25	13.37	13.81
V6	13.25	13.90	13.58
V7	13.99	13.58	13.78
V8	12.66	9.13	10.90
V9	14.30	14.54	14.42
V10	15.35	10.15	12.75
Average	**14.82**	**12.08**	**13.45**
Std dev	**1.601**	**1.821**	**1.256**

B-6 Notch Toughness - Shear Lip Height

Horizontal Side			
	Lip height 1	Lip height 2	average (µm)
HS1	513.99	530.11	522.05
HS2	976.68	959.66	968.17
HS3	552.26	982.29	767.28
HS4	516.03	902.16	709.10
HS5	536.87		536.87
HS6	569.36	847.79	708.58
HS7	443.18	402.57	422.88
HS8	712.97	620.92	666.94
HS9	657.80	759.76	708.78
HS10	580.97	810.07	695.52
		average	**670.62**
		std dev	**142.91**

Horizontal Top				
	Lip height 1	Lip height 2	Lip height 3	average (µm)
HT1	493.12	439.30		466.21
HT2	839.70	700.29		770.00
HT3	960.50	900.20		930.35
HT4	738.80	781.42		760.11
HT5				
HT6	688.83	735.81	358.48	594.37
HT7	1035.67	779.68		907.68
HT8	907.82	870.30		889.06
HT9	780.88	932.30		856.59
HT10	672.57	550.78	706.77	643.37
			average	**757.53**
			std dev	**150.63**

Vertical			
	Lip height 1	Lip height 2	average (µm)
V1	859.38	909.14	884.26
V2	893.81	1139.97	1016.89
V3	1173.12	904.76	1038.94
V4	895.47	1047.84	971.66
V5	1276.47	641.10	958.79
V6	978.98	832.98	905.98
V7	934.92	1109.34	1022.13
V8	876.83		876.83
V9	1087.17	961.12	1024.15
V10	829.06	970.16	899.61
		average	**959.92**
		std dev	**60.66**

B-7 Notch Toughness - Shear lip width

	Horizontal Side		
	Projected area	length of specimen	shear width (mm)
HS1	6.79	10	0.679
HS2	8.13	10	0.813
HS3	7.24	10	0.724
HS4	8.16	10	0.816
HS5	7.01	10	0.701
HS6	7.12	10	0.712
HS7	6.36	10	0.636
HS8	7.66	10	0.766
HS9	8.12	10	0.812
HS10	9.36	10	0.936
		avg	**0.760**
		std dev	**0.083**

	Horizontal Top		
	Projected area	length of specimen	shear width (mm)
HT1	9.45	10	0.945
HT2	12.38	10	1.238
HT3	8.79	10	0.879
HT4	11.21	10	1.121
HT5	8.42	10	0.842
HT6	9.09	10	0.909
HT7	9.53	10	0.953
HT8	10.29	10	1.029
HT9	11.35	10	1.135
HT10	11.87	10	1.187
		avg	**1.024**
		std dev	**0.131**

	Vertical		
	Projected area	length of specimen	shear width (mm)
V1	12.663	10	1.266
V2	12.632	10	1.263
V3	14.140	10	1.414
V4	15.859	10	1.586
V5	13.814	10	1.381
V6	13.575	10	1.358
V7	13.784	10	1.378
V8	10.898	10	1.090
V9	14.419	10	1.442
V10	12.753	10	1.275
		avg	**1.345**
		std dev	**0.126**

B-8 Notch Toughness - Porosity Analysis

Horizontal Top		
Specimen no	HT3 2 5	HT3 2 6
Magnification	400x	60x
Area (µm^2)	10305.828	3182.812
		4701.736
		2730.556
		6750.000
		1781.597
		2388.715
		5382.292
		5230.382
		5434.375
		4815.625
		5700.521
		7371.007
		1859.201
		3701.042
defect area	**10305.830**	**61029.861**
total area	**76800.000**	**3368664.000**
Ratio (def/ tot)	**0.134**	**0.018**
Percentage	**13.42**	**1.81**

Vertical		
Specimen no	V4 1 5	V4 1 6
Magnification	200x	200x
Area (µm^2)	5521.635	959.936
	1309.499	1438.455
	5269.431	3779.896
	1809.259	197.879
	1106.236	483.194
	228.682	1882.654
	296.358	336.656
	1700.507	480.015
		186.610
		448.126
defect area	**17241.607**	**10193.421**
total area	**302736.000**	**302736.000**
Ratio (def/ tot)	**0.057**	**0.034**
Percentage	**5.70**	**3.37**
Average	**4.53**	

B-9 Notch Toughness - Notch Radius

Horizontal Side	
Specimen	radius (µm)
HS1	519.741
HS2	669.549
HS3	636.375
HS4	560.860
HS5	633.959
HS6	518.233
HS7	588.214
HS8	506.043
HS9	558.041
HS10	605.153
avg	**579.617**
std dev	**53.453**

Horizontal Top	
Specimen	radius (µm)
HT1	541.051
HT2	476.051
HT3	485.297
HT4	472.476
HT5	541.999
HT6	343.993
HT7	384.750
HT8	477.986
HT9	501.801
HT10	437.853
avg	**466.326**
std dev	**59.689**

Vertical	
Specimen	radius (µm)
V1	454.005
V2	526.540
V3	498.480
V4	421.737
V5	466.171
V6	614.460
V7	361.296
V8	340.813
V9	513.017
V10	443.741
avg	**464.026**
std dev	**76.266**

B-10 SEM IMAGES

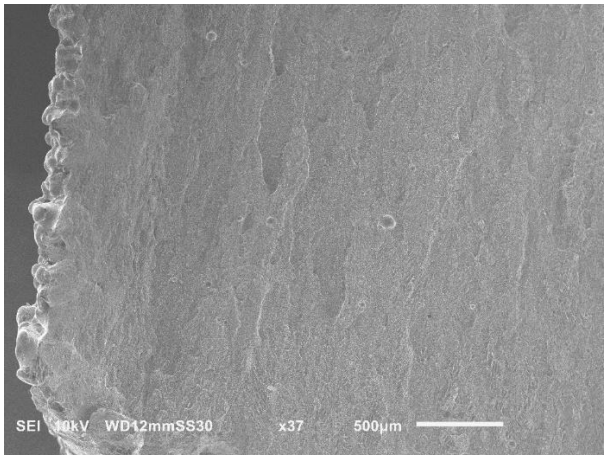

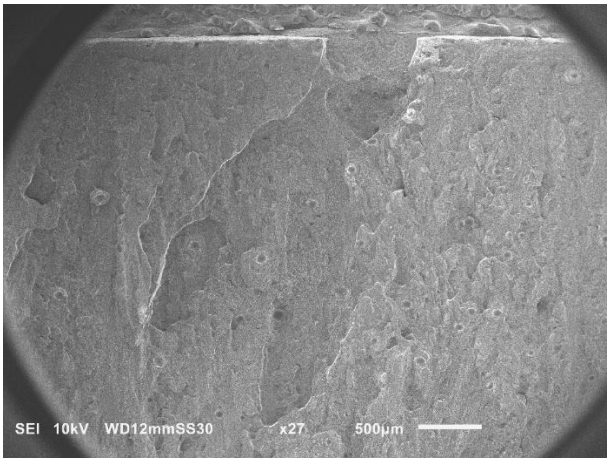

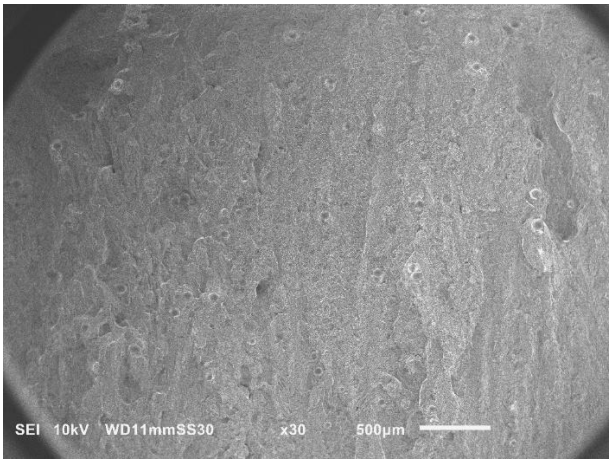

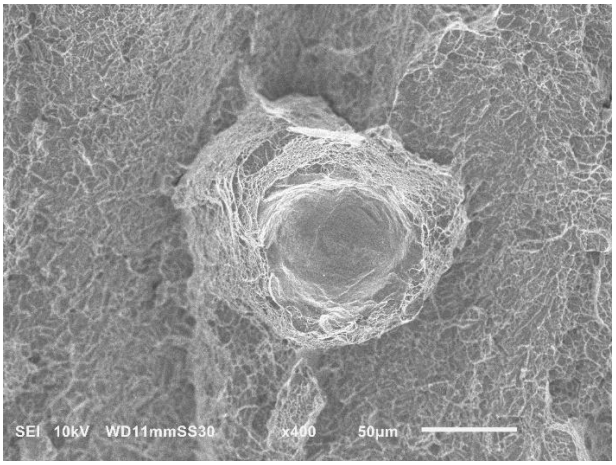

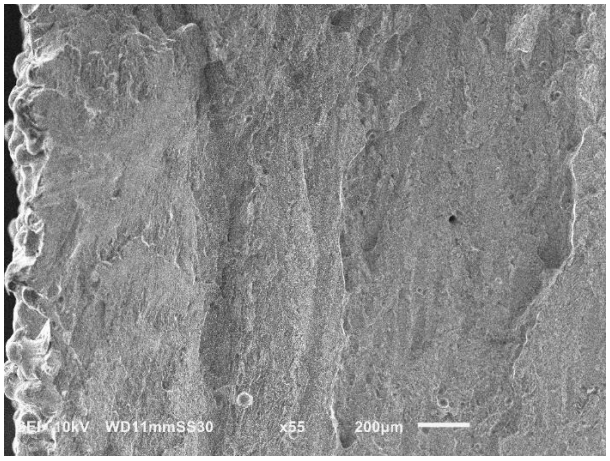

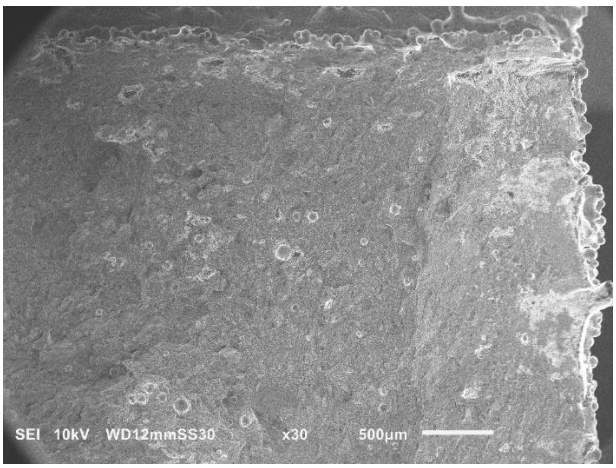

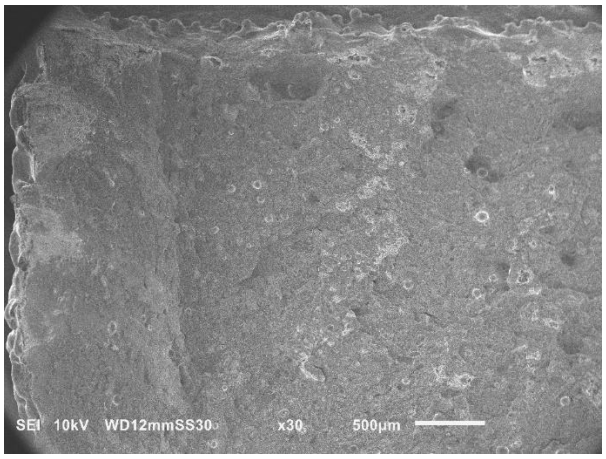
SEI 10kV WD12mmSS30 x30 500µm

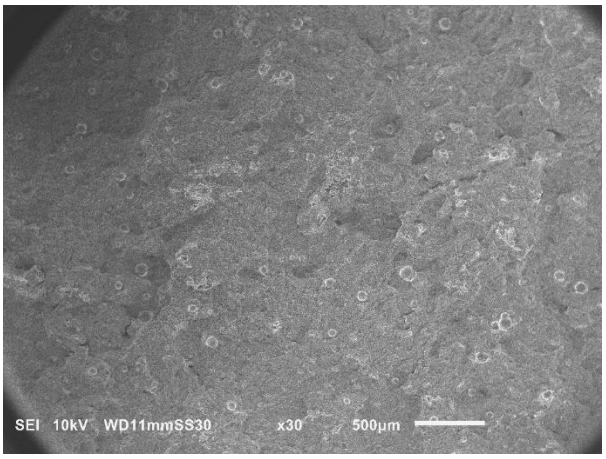
SEI 10kV WD11mmSS30 x30 500µm

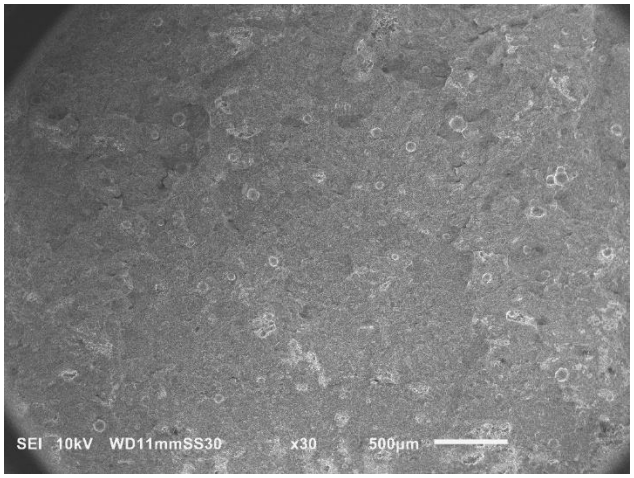
SEI 10kV WD11mmSS30 x30 500µm

B-11 Porosity Analysis Images

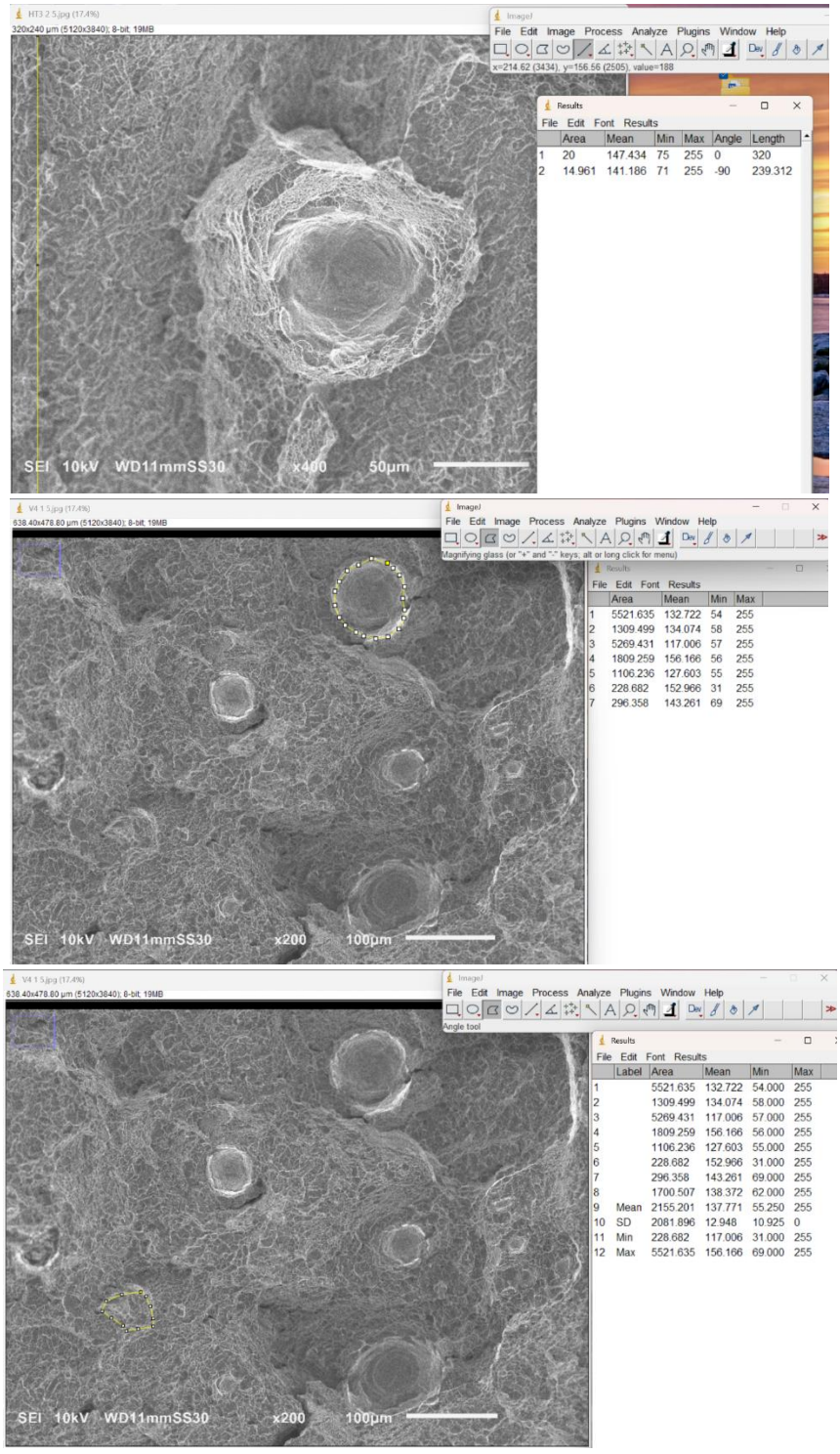

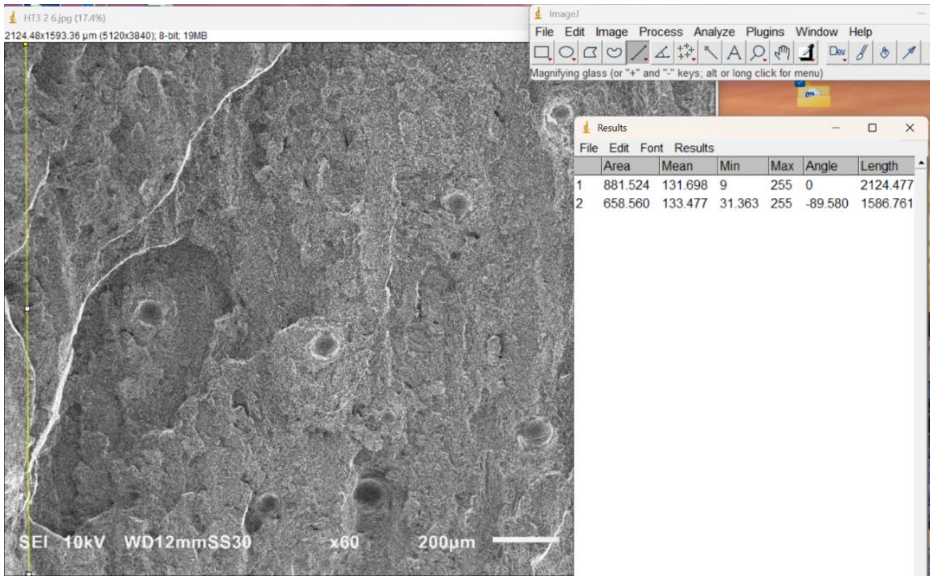
HT3 2 6.jpg (17.4%)
2124.48x1593.36 µm (5120x3840); 8-bit; 19MB
SEI 10kV WD12mmSS30 x60 200µm
ImageJ
File Edit Image Process Analyze Plugins Window Help
Magnifying glass (or "+" and "-" keys; alt or long click for menu)
Results
File Edit Font Results
Area Mean Min Max Angle Length
1 881.524 131.698 9 255 0 2124.477
2 658.560 133.477 31.363 255 -89.580 1586.761

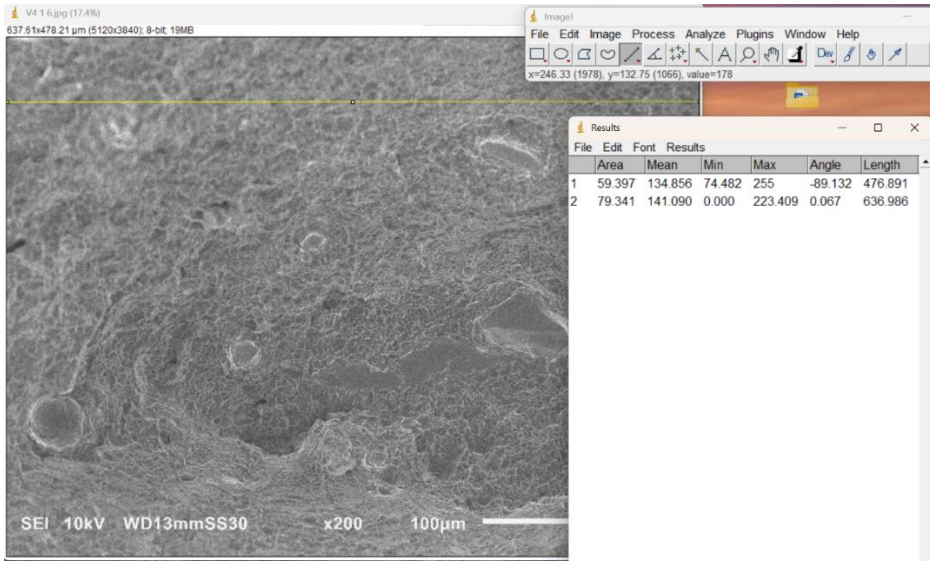
V4 1 6.jpg (17.4%)
637.61x478.21 µm (5120x3840); 8-bit; 19MB
SEI 10kV WD13mmSS30 x200 100µm
ImageJ
File Edit Image Process Analyze Plugins Window Help
x=246.33 (1978), y=132.75 (1066), value=178
Results
File Edit Font Results
Area Mean Min Max Angle Length
1 59.397 134.856 74.482 255 -89.132 476.891
2 79.341 141.090 0.000 223.409 0.067 636.986

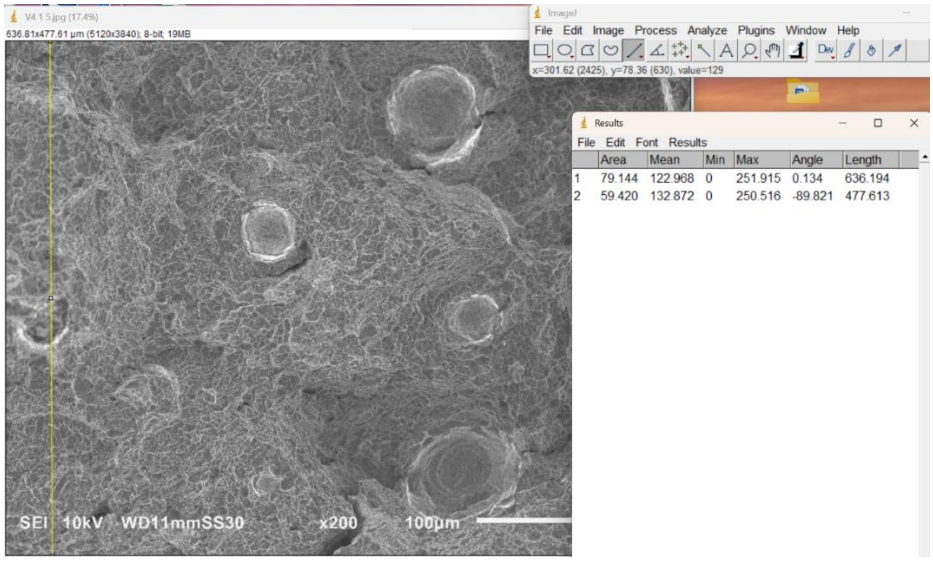
V4 1 5.jpg (17.4%)
636.81x477.61 µm (5120x3840); 8-bit; 19MB
SEI 10kV WD11mmSS30 x200 100µm
ImageJ
File Edit Image Process Analyze Plugins Window Help
x=301.62 (2425), y=78.36 (630), value=129
Results
File Edit Font Results
Area Mean Min Max Angle Length
1 79.144 122.968 0 251.915 0.134 636.194
2 59.420 132.872 0 250.516 -89.821 477.613

B-12 Impact Specimens in ARCAM build space

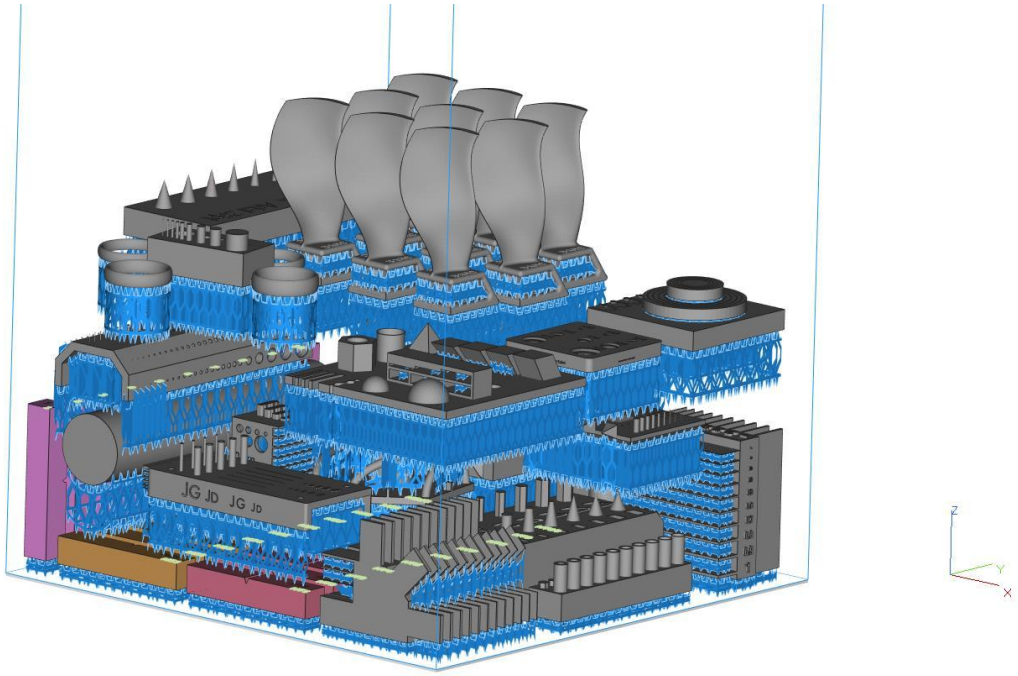

B-13 Impact specimens Fracture surfaces (projected shear area, impact energy)

Horizontal (HT)	Horizontal (HS)	Vertical (V)
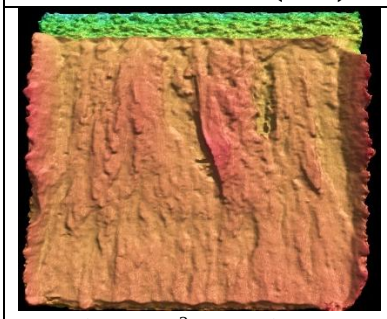 HT1 (9.5 mm^2, 16.5 J)	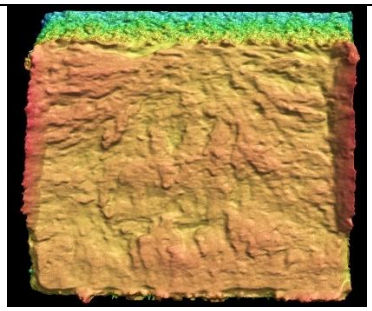 HS1 (6.8 mm^2, 15.6 J)	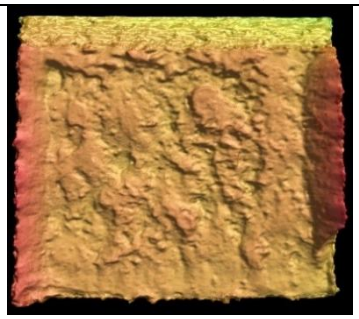 V1 (12.7 mm^2, 16 J)
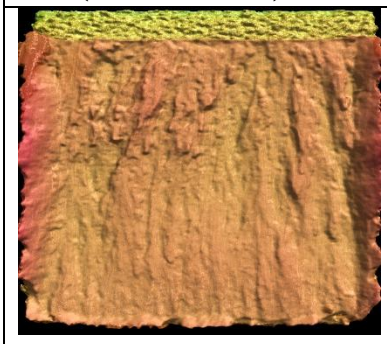 HT2 (12.4 mm^2, 15 J)	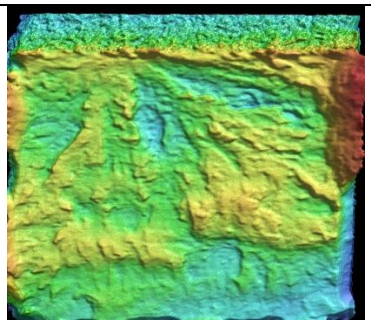 HS2 (8.1 mm^2, - J)	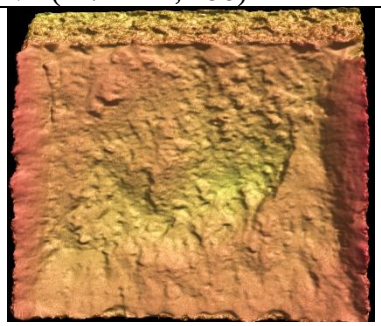 V2 (12.6 mm^2, 18.25 J)
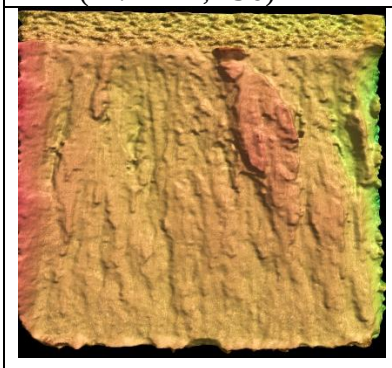 HT3 (8.8 mm^2, 17 J)	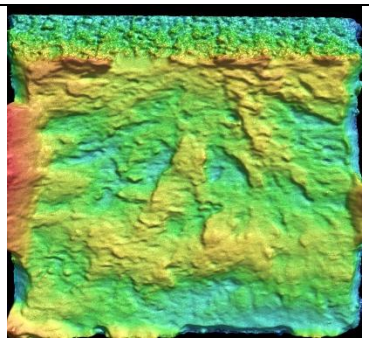 HS3 (7.2 mm^2, 16 J)	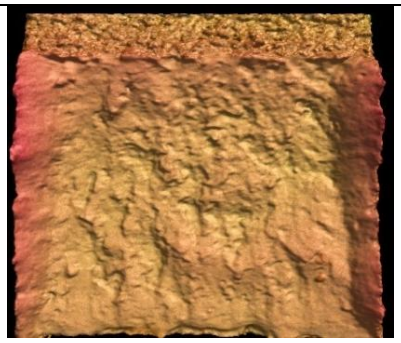 V3 (14.1 mm^2, 20.3 J)
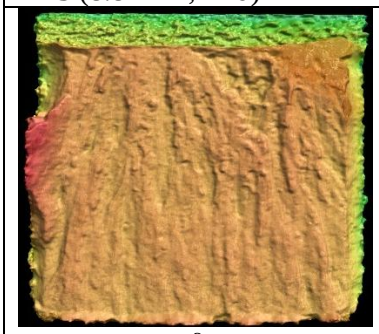 HT4 (11.2 mm^2, 16 J)	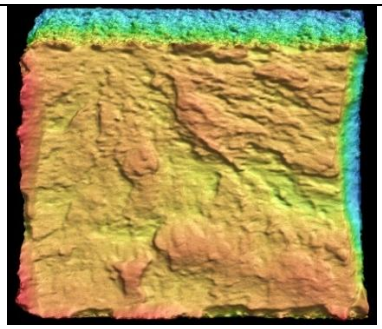 HS4 (8.2 mm^2, 15.5 J)	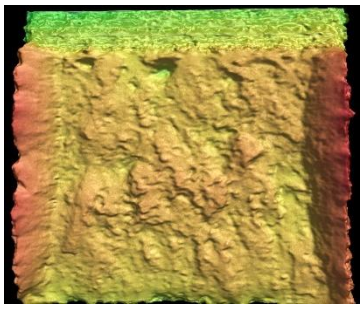 V4 (15.9 mm^2, 54.5 J)

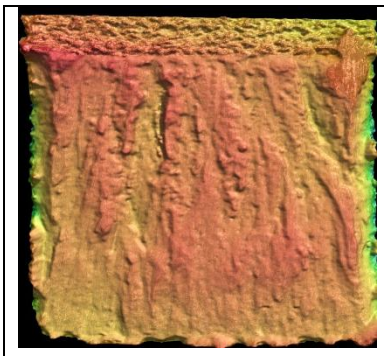 HT5 (8.4 mm^2, 16.25 J)	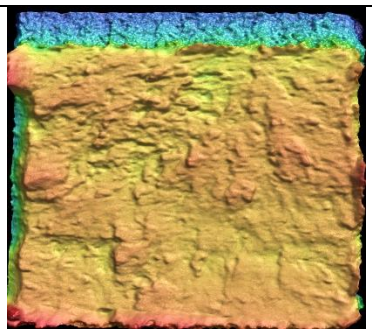 HS5 (7.0 mm^2, 16.25 J)	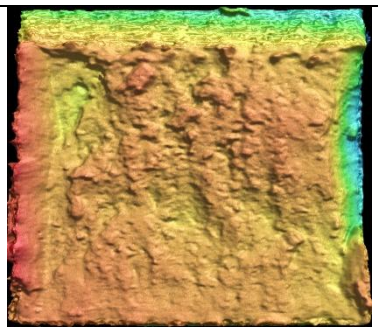 V5 (13.8 mm^2,16 J)
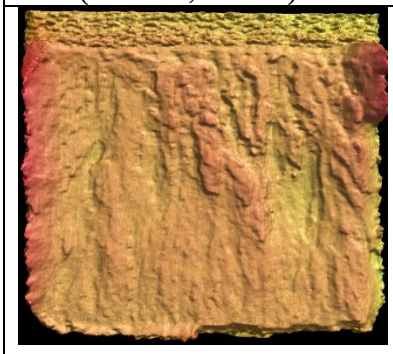 HT6 (9.0 mm^2, 15 J)	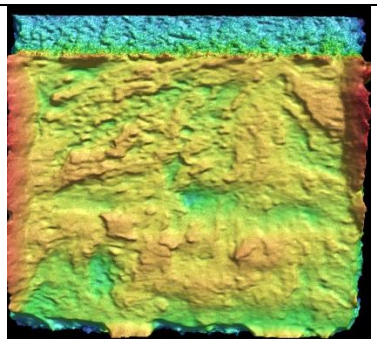 HS6 (7.1 mm^2, 15 J)	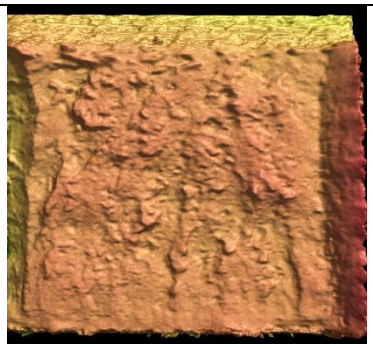 V6 (13.6 mm^2, 50.25 J)
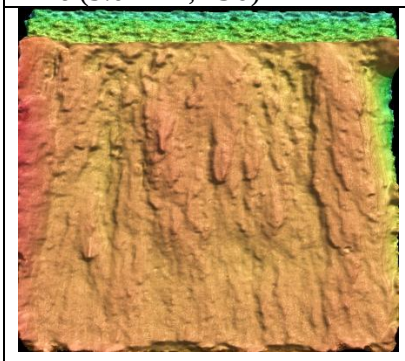 HT7 (9.5 mm^2, 14 J)	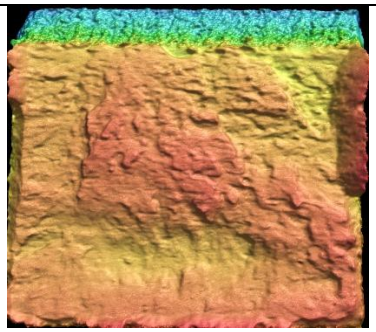 HS7 (6.4 mm^2, 15.25 J)	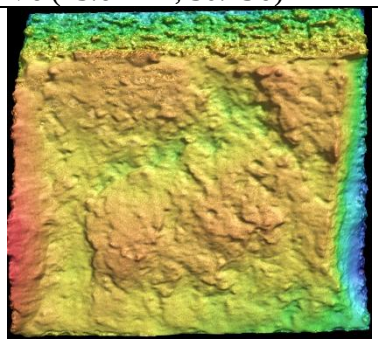 V7 (13.8 mm^2, 10.5 J)
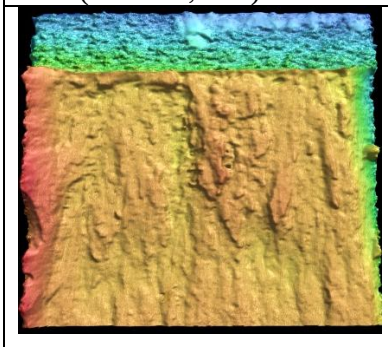 HT8 (10.3 mm^2, 14.5 J)	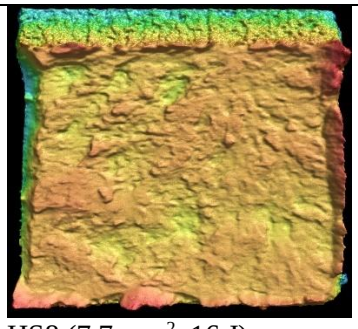 HS8 (7.7 mm^2, 16 J)	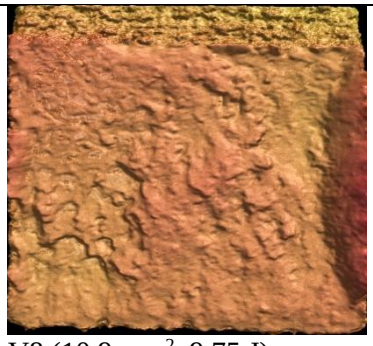 V8 (10.9 mm^2, 9.75 J)

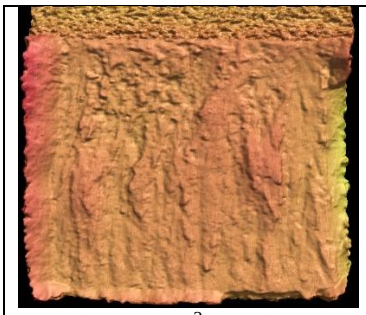 HT9 (11.4 mm^2, 14 J)	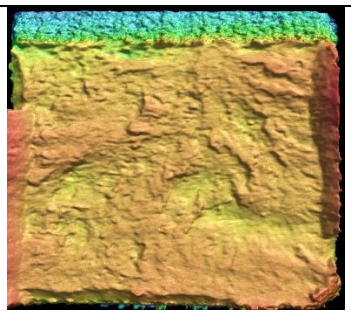 HS9 (8.1 mm^2, 16 J)	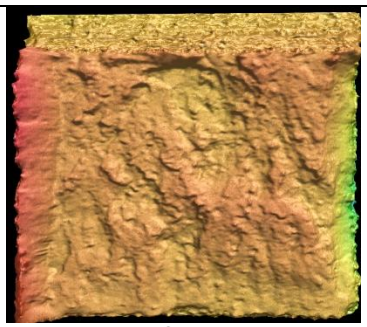 V9 (14.4 mm^2, 16 J)
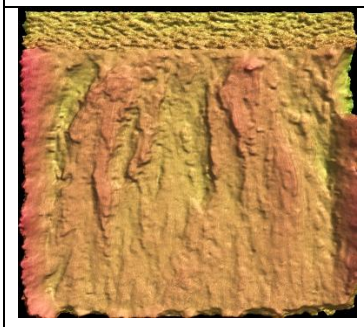 HT10 (11.9 mm^2, 16.5 J)	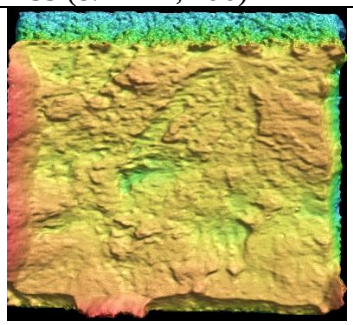 HS10 (9.4 mm^2, 17.75 J)	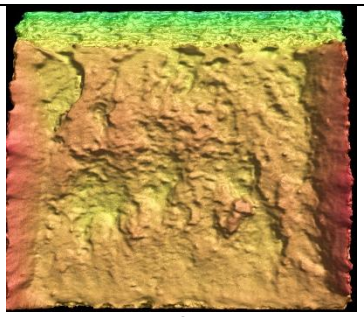 V10 (12.7 mm^2, 17 J)